

Surface Resistivity, Mechanical and Thermal Properties of Rotationally Moulded Polyethylene/Graphite Composites

By

Washington Mhike

Dissertation submitted in partial fulfilment of the requirements for the degree
of

Master of Science Applied Science (Chemical Technology)

In the Faculty of Engineering, Built Environment and Information
Technology
University of Pretoria

Pretoria

March 2012

DECLARATION

I, **Washington Mhike**, **Student No. 29712573**, do hereby declare that this research is my own original work and that to the best of my knowledge and belief, it has not been previously submitted in its entirety or in part and is not currently being submitted either in whole or in part at any university for a degree or diploma, and that all references are acknowledged.

SIGNED on this _____ day of _____ 2012.

Washington Mhike

Surface Resistivity, Mechanical and Thermal Properties of Rotationally Moulded Polyethylene/Graphite Composites

Student: Washington Mhike

Supervisor: Prof. Walter W. Focke

Department: Chemical Engineering

University: University of Pretoria

Degree: Master of Science Applied Science (Chemical Technology)

SYNOPSIS

Antistatic polymers are required to safely dissipate static charges from component surfaces. The overall objective of this study was to develop cost-effective antistatic and flame retardant polyethylene compounds with enhanced thermal conductivities suitable for rotational moulding (rotomoulding). Polymers with enhanced thermal conductivities exhibit better thermal responses during rotational moulding, thereby reducing cycle times. They also allow effective heat dissipation. This study considered the surface resistivity, mechanical and thermal properties of rotationally moulded, linear low-density polyethylene (LLDPE)/graphite composites. These composites contained natural Zimbabwean graphite, expandable graphite or expanded graphite as the antistatic and thermally conductive additive. Dry blending, melt compounding and double dumping were employed as the mixing methods to obtain antistatic composites at the lowest graphite contents. The properties of the composites prepared via these rotomoulded routes were compared to injection-moulded samples.

Dry blending was found to be an effective mixing method for rotomoulding antistatic LLDPE/graphite composites, thereby eliminating an expensive compounding step. Dry-blended Zimbabwean graphite composites showed the lowest surface resistivity at all graphite contents, with a surface resistivity of $10^5 \Omega/\square$ at 10 wt.%. Antistatic ranking for these composites was attained at 5 wt.% graphite content. Although rotomoulded powders

obtained following melt compounding of Zimbabwean graphite exhibited higher resistivity values, the variability was much lower. Injection moulding resulted in surface resistivity values above $10^{14} \Omega/\square$ for all compositions used. The rotomoulded composites exhibited poor mechanical properties in contrast to the injection-moulded composites. The Halpin-Tsai model showed good fits to the tensile modulus data of injection-moulded Zimbabwean and expandable graphite. These fits affirmed the anisotropic nature of the graphite fillers in the composites. All the determined residual aspect ratios were greater than 1.

Differential scanning calorimetry results showed that graphite fillers nucleate LLDPE crystallisation, thereby inducing higher crystallisation temperatures. The higher crystallisation temperatures observed for the LLDPE/graphite composites resulted in faster cooling rates. This is desirable for rotational moulding as cycle times will be reduced. Thermogravimetric analysis of the composites suggests that the presence of the graphite in the polyethylene matrix does not affect degradation of polyethylene. Mass losses for all the composites commence at about 400 °C.

Dry blending was also found to be an effective method of rotomoulding polyethylene/graphite composites with enhanced thermal conductivity. Dry-blended expanded graphite composites exhibited the best overall thermal conductivity with an 88% improvement at a graphite content of 20 wt.%. Melt compounded composites exhibited poor thermal conductivity values due to higher porosities in the mouldings. The thermal conductivities of injection-moulded composites were predominantly better than those for rotomoulded composites. However, conductivity values for injection-moulded composites at 10 wt.% were comparable to those of dry-blended rotomoulded composites at the same loading.

The geometric mean model fits the thermal conductivity data well at low volume fractions of graphite fillers for both rotomoulded and injection-moulded composites. The Lewis-Nielsen model was effectively fitted to the thermal conductivity data as the Halpin-Tsai model. Fittings of the model to the thermal conductivity data of the injection-moulded composites show that the thermal conductivity shape factors used for Zimbabwean and expandable graphite are more than twice those of the tensile modulus. Based on these observations, the shape factors used for the tensile modulus are not adequate for the thermal

conductivity data. The Lewis-Nielsen model was also fitted to the thermal conductivity data of the injection moulded composites using the maximum volumetric packing fractions, unlike in the Halpin-Tsai model. In this case the Lewis-Nielsen model yielded smaller shape factors, compared to when it was used without the maximum packing fractions, as the Halpin-Tsai model. The shape factors obtained from the fits of the thermal conductivity data of rotomoulded composites were smaller compared to the shape factors for injection moulded-composites.

Keywords: Rotomoulding, LLDPE, graphite, surface resistivity, antistatic, mechanical properties, thermal conductivity, Halpin-Tsai model, Lewis-Nielsen model

ACKNOWLEDGEMENTS

I would like to express my sincere gratitude to:

- Prof. Walter W. Focke, for his invaluable support and guidance, as well as his contributions and the encouragement that he gave me throughout this study.
- Ollie del Fabbro, for his advice and technical support.
- Joseph Sebekedi and staff of Xyris Technology, for their technical assistance, especially with the rotomoulding machine, and also the compounding and injection-moulding machines.
- The Institutional Research Development Programme (IRDP) of the National Research Foundation of South Africa and Xyris Technology CC, for the financial support for this research.
- All my colleagues at the Institute of Applied Materials: Shepherd Tichapondwa, Mthokozisi Sibanda, Nontete Nhlapo, Lumbidzani Moyo, Hermínio Muiambo, Shatish Ramjee, Hendrik Oosthuizen and Pedro Massinga Jr. for their thought-provoking suggestions and support.
- My parents, Boniface and Majorie, and brother Lawrence, for encouraging me. Thank you for the faith you have shown in me.
- The love of my life, Theresa T. Nyamadzawo, thank you for your patience and understanding.
- The Lord Our God, through whom all things are possible.

TABLE OF CONTENTS

SYNOPSIS	I
ACKNOWLEDGEMENTS	IV
LIST OF FIGURES	VIII
LIST OF TABLES	X
ABBREVIATIONS	XI
NOMENCLATURE	XIII
CHAPTER 1 : INTRODUCTION	1
1.1 Introduction.....	1
1.2 Background to the problem.....	2
1.3 Aims and objectives	3
1.4 Outline of this study.....	4
CHAPTER 2 : LITERATURE	6
2.1 Rotational moulding.....	6
2.1.1 Process characteristics	7
2.1.2 Melting and densification	8
2.1.3 Physical characteristics of rotomouldable materials.....	10
2.1.4 Technological advancements	10
2.2 Static electricity	11
2.2.1 Definition of static electricity	11
2.2.2 Triboelectrification	12
2.2.3 Hazards associated with static electricity	13
2.2.4 Antistatic materials	16
2.3 Static dissipative thermoplastics	18
2.3.1 Non-particulate conductive fillers.....	19
2.3.2 Particulate conductive additives	22
2.4 Graphite.....	24
2.4.1 Graphite structure.....	24
2.4.2 Graphite properties.....	24

2.4.3 Graphite types	25
2.4.4 Occurrence and production of natural graphite	25
2.4.5 Graphite intercalation compounds	26
2.4.6 Expanded graphite	26
2.4.7 Graphite applications	27
2.5 Electrical conductivity of graphite/thermoplastic composites.....	28
2.5.1 Effect of filler aspect ratio	28
2.5.2 Effect of constituent conductivity of the filler.....	29
2.5.3 Effect of polymer matrix properties on conductivity.....	30
2.5.4 Effect of particle size	31
2.5.6 Effect of processing	32
2.6. Rotomoulded polymer thermoplastic composites.....	34
2.6.1 Incorporation of the filler into the matrix	34
2.7 Mechanical properties of polymer composites	35
2.7.1 Composite moduli.....	35
2.7.2 Composite strength	38
2.7.3 Impact strength.....	41
2.7.4 Influence of composite structure on mechanical properties	42
2.7.5 Mechanical properties of rotationally moulded composites	44
2.7.6 Prediction of mechanical properties.....	47
2.8. Thermal conductivity of polymer composites	52
2.8.1 Thermal conductivity.....	52
2.8.2 Factors that influence thermal conductivity of polymer composites	52
2.8.3 Prediction of composite thermal conductivity	55
CHAPTER 3 : EXPERIMENTAL.....	61
3.1 Materials	61
3.1.1 Material characterisation.....	61
3.2 Methods.....	62
3.2.1 Rotational moulding.....	63
3.2.2 Injection moulding	64
3.2.3 Composite characterisation.....	64
CHAPTER 4 : RESULTS AND DISCUSSION.....	69

4.1 Material characteristics	69
4.2 Composite aesthetics.....	71
4.3 Graphite dispersion and composite morphology	74
4.4 Rheology	78
4.5 Porosity	78
4.6 Differential scanning calorimetry	79
4.7 Surface resistivity.....	81
4.8 Mechanical properties	84
4.8.1 Young’s modulus	84
4.8.2 Tensile yield strength.....	85
4.8.3 Elongation-at-break.....	88
4.8.4 Impact strength.....	88
4.9 Thermal properties	90
4.9.1 TGA	90
4.9.2 Thermal conductivity	91
4.10 Discussion	94
4.10.1 DSC.....	94
4.10.2 Surface resistivity.....	94
4.10.3 Mechanical properties	95
4.10.4 Thermal properties	99
CHAPTER 5 : CONCLUSIONS AND RECOMMENDATIONS	106
REFERENCES.....	109
APPENDICES	121
Appendix A: Rotomoulding charge weights.....	121
Appendix B: Berstorff compounding data	123
Appendix C: Injection moulding data.....	124
Appendix D: Falling weight (Gardner Impact) impact resistance test calculations	126
Appendix E: Photomicrographs of double-dumped composites	129
Appendix F: SEM fractographs of double-dumped rotomoulded composites	130
Appendix G: DSC scans for pre-compounded rotomoulded graphite/LLDPE composites	131
Appendix H: Publications arising from this work	132

LIST OF FIGURES

Figure 1-1	The rotational moulding process.....	1
Figure 2-1	Major axis and minor axis on a rotomoulding machine	7
Figure 2-2	Powder flow and sintering in a heated, rotating mould	9
Figure 2-3	Percolation of a conductive filler in an insulating matrix	23
Figure 3-1	Concentric ring probe and high-resistance meter	67
Figure 4-1	Graphite particle size distributions	69
Figure 4-2	SEM micrographs of polyethylene and graphites	70
Figure 4-3	Digital photos of the interior surfaces of rotomoulded LLDPE/polyethylene composites.....	72
Figure 4-4	Digital photos of the interior surfaces of rotomoulded LLDPE/polyethylene composites.....	73
Figure 4-5	Digital photos of the interior surfaces of rotomoulded LLDPE/polyethylene composites.....	73
Figure 4-6	Photomicrographs of polished rotomoulded composite sections.....	75
Figure 4-7	Photomicrographs of polished injection-moulded composite sections.....	76
Figure 4-8	SEM fractographs of rotomoulded composites with 10 wt.% graphite:	77
Figure 4-9	Variation of zero-shear viscosity of LLDPE/graphite composites with temperature	78
Figure 4-10	Variation of the porosity of LLDPE/graphite composites with graphite content	79
Figure 4-11	DSC scans for dry-blended rotomoulded graphite/LLDPE composites	80
Figure 4-12	DSC scans for injection-moulded graphite/LLDPE composites	80
Figure 4-13	Exterior surface resistivity, rotomoulded LLDPE/Zimbabwean graphite composites.....	82
Figure 4-14	Exterior surface resistivity, rotomoulded LLDPE/expandable graphite composites.....	83
Figure 4-15	Exterior surface resistivity, rotomoulded expanded graphite composites	83
Figure 4-16	Lowest exterior surface resistivities of each rotomoulded graphite type	84
Figure 4-17	TGA of compounded rotomoulded composites with graphite at 10 wt.% content.....	91
Figure 4-18	Fits of the Arrhenius equation to the viscosity data of polyethylene/graphite composites.....	96

Figure 4-19	Fitting the Halpin-Tsai model to Young's moduli data of injection-moulded composites.....	99
Figure 4-20	Fits of the geometric mean model and least square fits of the Halpin-Tsai (HT) model to the thermal conductivity data of the rotomoulded composites.	102
Figure 4-21	Fits of the geometric mean model and least square fits of the Halpin-Tsai model to the thermal conductivity data of the injection-moulded composites	103
Figure E-1	Photomicrographs of polished double-dumped rotomoulded composite sections.....	129
Figure F-1	SEM fractographs of double-dumped rotomoulded composites with 10 wt.% graphite	130
Figure G-1	DSC scans for pre-compounded rotomoulded graphite/LLDPE composites	131

LIST OF TABLES

Table 2-1	Classification of ESD materials	18
Table 2-2	Antistatic agents.....	19
Table 2-3	Graphite properties.....	25
Table 2-4	Graphite occurrence and production in 2011	26
Table 2-5	Variation of the percolation threshold with graphite particle size.....	31
Table 3-1	Description of rotomoulding and injection moulding experiments	62
Table 3-2	Rotomoulding conditions.....	64
Table 4-1	Physical properties of graphite.....	69
Table 4-2	XRF analysis of graphites.....	71
Table 4-3	Effect of graphite type and content as well as processing method on the Young's modulus (MPa) of LLDPE/graphite composites.....	86
Table 4-4	Effect of graphite type and content as well as processing method on the yield strength (MPa) of LLDPE/graphite composites	87
Table 4-5	Effect of graphite type and content as well as processing method on the elongation-at-break (%) of LLDPE/graphite composites	89
Table 4-6	Falling-weight impact (Gardner Impact) resistance of LLDPE/graphite composites.....	90
Table 4-7	Effect of graphite type and content as well as processing method on the thermal conductivity (W/mK) of LLDPE/graphite composites.....	93
Table 4-8	Halpin-Tsai model shape factors for estimating the thermal conductivity of LLDPE/graphite composites.....	104
Table 4-9	Nielsen-Lewis model shape factors for estimating the thermal conductivity of LLDPE/graphite composites.....	105
Table A-1	Rotomoulding charge weights: Zimbabwean graphite composites	122
Table A-2	Rotomoulding charge weights: Expandable graphite (ES 170 300A) composites.....	122
Table A-3	Rotomoulding charge weights: Expanded graphite (ES 250 B5) composites	122
Table B-1	Bestorff compounding data.....	123
Table C-1	ASTM drop impact test mould injection moulding conditions	124
Table C-2	ASTM Tensile test mould injection moulding conditions.....	125
Table D-7	Calculation of the impact resistance of 5 wt.% Zimbabwe graphite, compounded, rotomoulded	126

ABBREVIATIONS

ABS	Acrylonitrile butadiene styrene
ASTM	ASTM International
BET	Brunauer-Emmett-Teller
BN	Boron nitride
D ₅₀	Median particle size in the particle size distribution
d.c.	Direct current
DGEBA	Diglycidyl ether of bisphenol A
DSC	Differential scanning calorimetry
EG	Expanded graphite
ES 170 300A	Expandable graphite ES 170 300A
ES 250 B5	Expandable graphite ES 250 B5
ESD	Electrostatic discharge
EVA	Ethylene vinyl acetate
FESEM	Field Emission Scanning Electron Microscopy
FTIR	Fourier transform infrared
GIC	Graphite intercalation compound
GN/GNP	Graphite nanoplatelet
g-PE	Grafted polyethylene
g-PP	Grafted polypropylene
HDPE	High-density polyethylene
HT	Halpin-Tsai
ICP	Intrinsically conductive polymer
IDP	Intrinsically dissipative polymer
IEC	International Electrotechnical Commission
LDPE	Low-density polyethylene
LLDPE	Linear low-density polyethylene
LMDPE	Linear medium-density polyethylene
LN	Lewis-Nielsen
LOI	Loss on ignition
MFI	Melt flow index
MRF	Modulus reduction factor

NBR	Acrylonitrile butadiene rubber
OroxPk	Polymerised 2,2,4-trimethyl-1,2-dihydroquinoline
PA-6	Polyamide 6
PAni	Polyaniline
PC	Polycarbonate
PE	Polyethylene
PEO	Polyethylene oxide
phr	Parts per hundred of rubber or resin
PIAT	Peak internal air temperature
PMMA	Poly(methyl methacrylate)
PS	Polystyrene
rpm	Revolutions per minute
SBR	Styrene-butadiene rubber
SEM	Scanning electron microscopy
TEM	Transmission electron microscopy
TGA	Thermogravimetric analysis
Vol.%	Volume percent
wt.%	Weight percent
XRF	X-ray fluorescence

NOMENCLATURE

V	DC voltage (V)
I	Steady-state current (A)
R_v	Volume resistance (Ω)
ρ_v	Volume resistivity (V/m)
R_s	Surface resistance (Ω)
ρ_s	Surface resistivity (Ω/\square) or (Ω)
σ_c	Conductivity of the conductive additive (S/m)
σ	Conductivity of the composite (S/m)
v	Volume fraction of the conductive additive
t	A critical exponent of a universal character in the percolation model, equation 2-4
v_c	Percolation threshold
A	Surface area of a single filler particle (m^2)
V	Volume of a single filler particle (m^3)
η_c	Suspension viscosity (Pa.s)
η_p	Matrix viscosity (Pa.s)
k_E	Einstein coefficient
v_f	Volume fraction of filler particles
v_p	Volume fraction polymer matrix
E_c	Tensile or elastic modulus of composite (MPa)
E_p	Tensile or elastic modulus of matrix (MPa)
α	Filler aspect ratio
v_m	The maximum packing efficiency of the filler
ζ	Shape factor that depends on the geometry of filler particles and their relative orientation with respect to the load direction in the Halpin-Tsai and Lewis-Nielsen models, equations 2-12 and 2-15
η	A parameter which relates the matrix and filler moduli or thermal conductivities in the Halpin-Tsai and Lewis-Nielsen models

E_{CT}	Transverse composite modulus (MPa)
E_{CL}	Longitudinal composite modulus (MPa)
ξ_L, ξ_T	Van Es corrected shape factors for platelet reinforcements in the longitudinal and transverse direction in the Halpin-Tsai model
ψ	A parameter which relates the maximum volumetric packing fraction of filler to the volume fraction of the filler, in the Lewis-Nielsen model
MRF	Modulus reduction factor
φ	Parameter in the Verbeek & Focke model, equation 2-17
χ	Modified voidage (voidage relative to the polymer phase)
ϕ	Composite porosity/void content
G_p	Polymer matrix shear modulus (MPa)
q	Heat flux (W/m^2)
T	Temperature ($^{\circ}C$)
x	Thickness (m)
λ	Thermal conductivity (W/m.K)
λ_c	Composite thermal conductivity (W/m.K)
λ_f	Filler thermal conductivity (W/m.K)
λ_p	Matrix thermal conductivity (W/m.K)
A	Shape factor that depends on the geometry of the filler particles and their relative orientation with respect to the heat flow in the Lewis-Nielsen model for thermal conductivity, equation 2-27
B, C	Parameters in the Cheng and Vachon model for thermal conductivity, equation 2-31
C_1, C_2	Constants in the Agari model for thermal conductivity
S_z, S_{xy}	Parameters in the Hatta model, equation (2-46)
β	Filler aspect ratio in the Hatta model, equation (2-46)
ρ_s	Surface resistivity (Ω/\square)
R_x	Surface resistance (Ω)
d_1	Diameter of the inner electrode of the concentric ring probe (m)
g	Distance (gap) between the electrodes of the concentric ring probe (m)

η	Zero-shear viscosity (Pa.s)
η_0	Pre-exponential constant with dimensions of viscosity
E_a	Activation energy (kJ/mol)
R	Gas constant (kJ/K.mol)
T	Absolute temperature (K)
A_L, A_T	Shape factors for the longitudinal and transverse thermal conductivity in the Halpin-Tsai model for thermal conductivity
$\lambda_{CL}, \lambda_{CT}$	Longitudinal and transverse thermal conductivity of composites in the Halpin-Tsai model for thermal conductivity
w	Platelet width (platelet fillers) (m)
t	Platelet thickness (m)

CHAPTER 1 : INTRODUCTION

1.1 Introduction

Rotational moulding, also referred to as rotomoulding or rotocasting, has become one of the most important polymer processing technologies. Rotomoulding has a reported annual growth rate of 10–20% (Yan *et al.*, 2006). It competes strongly with other polymer processing techniques such as injection moulding, compression moulding and thermoforming.

Rotomoulding is used to make hollow plastic structures. Essentially, a predetermined amount of resin in powder or liquid form (Beall, 1998) is charged into a mould which is then closed tightly and rotated biaxially. Heat is applied to the mould, and the solid polymeric material inside melts, forming a layer which takes the shape of the mould, thus forming the product. The mould is then cooled to a temperature suitable for the product to solidify and be ejected. Figure 1-1 shows a schematic of the rotomoulding process.

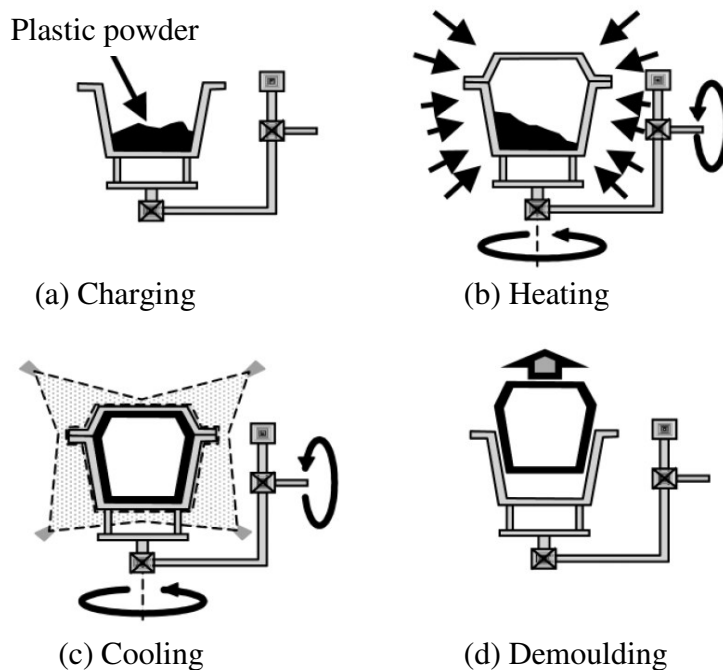


Figure 1-1 The rotational moulding process (Crawford & Throne, 2002)

1.2 Background to the problem

Polyethylene is the principal rotomoulding material (Liu & Peng, 2010). The paucity (and limited mobility) of charge carriers (Jian *et al.*, 2010) results in a high-volume resistivity that makes polyethylene an effective insulator. The high surface resistivity allows the build-up and retention of static charges on product surfaces. Static electricity is a nuisance as well as a hazard, as it is a potential ignition source for fires and explosions.

Polymers can be rendered electrostatically dissipative in several ways (Rosner, 2001), but studies specific to rotomoulding applications are rare (Patch, 2001; Kelly III & Jones, 2002; Angelico 2011). Antistatic agents, intrinsically conductive polymers (ICPs), inherently dissipative polymers (IDPs) and conductive particulates are commonly used (Rosner, 2001). Conventional antistatic agents offer limited static protection due to their migratory nature and the need for a minimum relative humidity (Rosner, 2001). Their high volatility further limits their use in the rotomoulding process (Dahman, 2003). Inherently dissipative polymers (IDPs) and intrinsically conductive polymers (ICPs) are also not suitable owing to insufficient thermal stability (Campbell & Tan, 1995). However, conductive particulate fillers such as graphite are an attractive option for rotomoulding.

Polymers typically exhibit low thermal conductivity values (Debelak & Lafdi, 2007; Wang *et al.*, 2001). LLDPE has a thermal conductivity of about 0.22 W/m.K (An *et al.*, 2009). Higher levels of thermal conductivity in polymeric materials are necessitated by the increased use of polymer materials in numerous applications such as circuit boards, heat exchangers, appliances and machinery where appreciable levels of conductivity are required (Bigg, 1995). Also, thermally conductive polymers are being sought for bipolar plates for use in fuel cells (Gaxiola *et al.*, 2010).

The thermal conductivity of a material determines how effectively heat will be dissipated when it is exposed to a heat source. In a low-conductivity material, heat will remain concentrated on the exposed surface area and the material will ignite earlier (Patel *et al.*, 2011). However, in a material with high conductivity, the heat is dissipated effectively, and the material will take a longer time to ignite. The time to ignition is recognised as an important material parameter in the assessment of fire hazards (Whiteley, 1993; Irvine *et al.*,

2000). The time to ignition gives a measure of the ignitability of the material. A longer time to ignition delays the combustion process, which is desirable in a fire situation.

High thermal conductivity is important in rotomoulding because enhanced heat transfer results in shorter cycle times (Robert & Crawford, 1999; Robert *et al.*, 2000; Planes *et al.*, 2008). A variety of fillers, including metal powders, have been used to enhance the thermal conductivity of polymers (Tavman, 1998). The use of graphite as a thermal conductive additive has been investigated previously. The study by Planes *et al.* (2008) was focused on reducing the rotomoulding cycle time by enhancing the thermal conductivity using lamellar graphite as a constituent of a nanocomposite with ethylene-polypropylene copolymer.

Natural flake graphite is a layered mineral comprising stacked graphene sheets of covalently bonded carbon atoms. It has a high thermal and electrical conductivity suitable even for electrochemical applications (Wissler, 2006). The conductivity of the flakes is anisotropic. It is high in the in-plane direction but much lower in the direction perpendicular to the graphene layers (Chung, 2002).

Expandable graphite is made by partial oxidation of the graphene sheets with simultaneous intercalation (i.e. insertion) of charge-neutralising guest species (e.g. sulphuric acid anions) in between the stacked graphene layers (Chen *et al.*, 2003a). Upon exposure to high temperatures, the intercalated guest ions decompose, forming a gas that causes the flakes to expand rapidly in a worm-like manner and to occupy a much larger volume (Chung, 2002; Wissler, 2006). Expandable graphite is a good intumescent flame retardant for polyethylene at a loading of 10 wt.% and above (Xie & Qu, 2001). Expandable graphite has similar in-plane electrical conductivity as natural flake graphite (Zheng *et al.*, 2004). This means that it could impart both antistatic and flame-retardant properties to polyethylene.

1.3 Aims and objectives

The aim of this study was to develop cost-effective antistatic and flame-retardant polyethylene compounds with enhanced thermal conductivity, suitable for rotomoulding. The main objective was to compare the utility of different graphite forms and mixing methods. In

pursuit of these goals, the surface resistivity, mechanical and thermal properties of rotomoulded graphite/polyethylene composites were determined. Composites were prepared using dry blending of the filler and neat polymer powders, a double-dumping procedure of the graphite and neat polymer powders, and also by powders obtained by the milling of pre-compounded material. Natural Zimbabwean flake graphite, expandable graphite and pre-expanded graphite were explored as fillers. The properties of the composites prepared via these rotomoulded routes were compared to injection-moulded samples.

1.4 Outline of this study

Chapter 1 gives a brief introduction to the rotomoulding process and outlines the underlying problems encountered when polyethylene is used as the rotomoulding material. The aims and objectives of the study are presented.

Chapter 2 presents a detailed literature review. The chapter is divided into eight main sections. The first section gives a brief history of the rotomoulding process, its attributes, and state-of-the-art. The second section focuses on static electricity – its generation, hazards that emanate from it and antistatic materials. The third section reviews the formulation of static dissipative thermoplastics and their suitability for the rotomoulding process. The fourth section reviews the nature of graphite – its properties, occurrence and uses. The fifth section focuses on the electrical conductivity of graphite/thermoplastic composites. Factors which influence the electrical conductivity of graphite/thermoplastic composites are explored in this section. The sixth section presents a review of rotomoulding thermoplastic composites. The last two sections focus on the mechanical properties and thermal conductivity of polymer/graphite composites, and also the mechanical properties of rotomoulded composites. Factors that affect these properties are explored and the models proposed to predict these properties are examined.

Chapter 3 gives a description of the experimental work carried out in this study. The details of the materials, equipment and experimental methods used are presented. The characterisation techniques used are also given.

Chapter 4 presents the results and discussion. The first sections give the material characteristics and structure of the composites. The surface resistivity, mechanical and thermal properties of the composites using the three graphite forms and the three different mixing methods used are then presented. A discussion of the results follows, with the modelling of the modulus and thermal conductivity.

Chapter 5 gives the conclusions and recommendations.

CHAPTER 2 : LITERATURE

2.1 Rotational moulding

Rotational moulding has its roots in ancient Egyptian ceramic pottery and the making of chocolate eggs by the Swiss in the 1600s (Crawford & Throne, 2002). However, British Patent No. 1301 issued to R. Peters in 1855 is acknowledged as the first citation of rotomoulding. The patent addressed better ways of manufacturing metal ordinance shells and other hollow vessels (Beall, 1998). Beall (1998) has described the evolution of the process in detail. In summary, after the 1855 Peters patent, rotational moulding evolved through the late 19th and early 20th centuries, with patents being issued for various aspects of the process. For instance, in US patent 1 341 670 issued to R. J. Powell in 1920 for the moulding of plaster of Paris objects, the advantages of slow rotation and absence of a centrifugal force were shown. The patent also described the commonly used rotation ratio of 4 to 1. The rotation ratio is the relative number of revolutions of the major axis to those of the minor axis determined as:

$$\text{Rotation ratio} = \frac{\text{Major axis rpm}}{\text{Minor axis rpm} - \text{Major axis rpm}}, \quad (2-1)$$

where rpm are revolutions per minute. Figure 2-1 shows the major and minor axis on a rotomoulding machine.

However, rotomoulding was only introduced in polymers in the 1930s (Beall, 1998). The introduction of plasticised liquid polyvinyl chloride (plastisols) in 1946 led to the expansion of the rotomoulding industry. Up to the 1960s, plastisols dominated the rotomoulding industry. The advent of polyethylene powders in the late 1950s was a milestone in the rotational moulding industry, as these powders established themselves as the industry workhorse. The growth of the industry has also been sustained by equipment development and technological advancements (Beall, 1998).

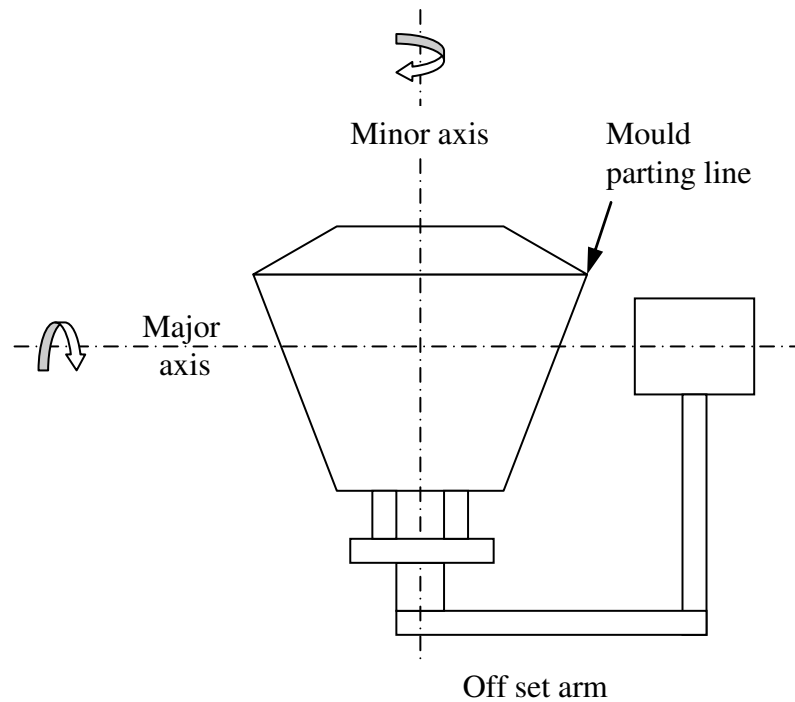


Figure 2-1 Major axis and minor axis on a rotomoulding machine (adapted from Osswald, 1998)

2.1.1 Process characteristics

Rotational moulding is a high-temperature, low-pressure and zero-shear process. Oven temperatures are usually set to 300 °C or more (Crawford, 1996). It is noted that no centrifugal forces are involved in rotomoulding as the rotational speeds used are typically low (10–30 rpm) (Crawford & Throne, 2002).

Crawford & Throne (2002) mention a wide range of rotomoulded product categories, for the following markets:

- Tanks
- Automotive
- Toys and leisure
- Marine industry products

Advantages of the rotomoulding process over other polymer-forming processes include relatively low residual stress in products as it is a low-pressure process. Wall thickness of parts is relatively uniform (Crawford & Gibson, 2006). The wall thickness

distribution can be manipulated without mould modifications (Crawford & Throne, 2002). The moulds used are relatively inexpensive and the process is suitable for short runs. Large and complex parts with intricate details can be moulded. Rotomoulding has the ability to make one-piece parts with no weld lines, ejector pin marks or sprue scars. Also multilayered and foamed parts can be moulded (Crawford & Gibson, 2006). Material wastage is limited as all the material charge is essentially formed into the product. There are relatively short lead times in the manufacture of moulds (Crawford & Gibson, 2006). The mould design constraints are limited (Yan *et al.*, 2006). Different parts can be run on one machine simultaneously (Beall, 1998). Inserts can also be moulded in (Crawford & Gibson, 2006). The process has the ability to mould in graphics (Crawford & Gibson, 2006).

The major constraint of the rotomoulding process compared to other processes is the long cycle time. As a result of the long cycle times and exposure to high temperatures, there are material limitations due to the possibility of thermal degradation (Beall, 1998). The materials are also relatively expensive due to the need for pulverising and additive packages (Crawford & Gibson, 2006). Energy costs are relatively higher due to heating and cooling of the mould and the material (Beall, 1998). The application of mould release is an additional step (Beall, 1998).

2.1.2 Melting and densification

During the early stages of the rotomoulding process, a powder pool is formed at the bottom of the mould (Figure 2-2). The powder tumbles in the mould as it is rotated, coming into contact with all areas of the mould interior (Crawford, 1996). As heat is transferred to the mould and the temperature of the mould wall rises, the powder particles begin to melt and adhere to the mould (Bellehumer, 2005). The particles also start to fuse together or coalesce (also called sintering) (Chaudhary *et al.*, 2001), forming a homogenous polymer melt. During this stage air is trapped between the particles as they coalesce, resulting in the formation of bubbles or pin holes (Bellehumer, 2005), which are characteristic of rotomoulded parts (Crawford, 1996). As the heating continues, the melt densifies, with the bubbles dissolving into the melt (Bellehumer, 2005). After this stage, the mould is cooled, allowing the moulded part to solidify. The measurement of the internal air temperature of the mould allows the visualisation of the stages in the rotomoulding process (Crawford & Throne, 2002).

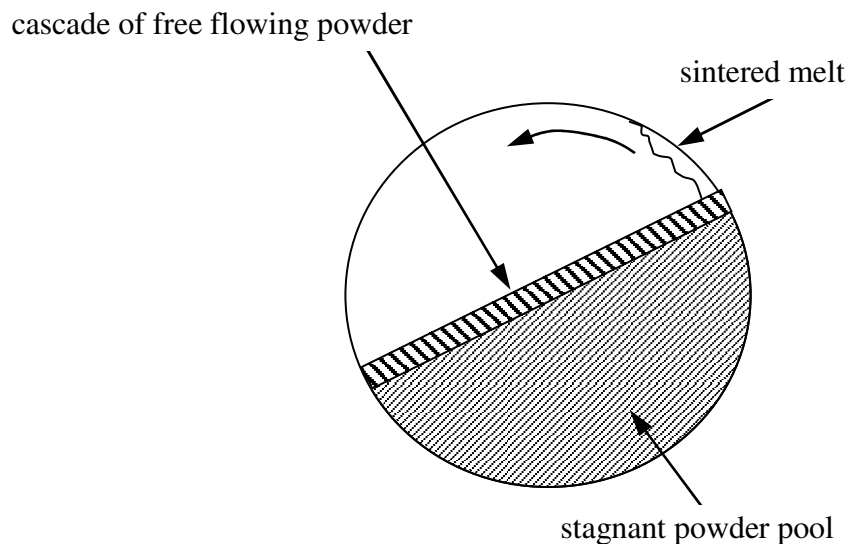


Figure 2-2 Powder flow and sintering in a heated, rotating mould (adapted from Pethrick & Hudson, 2008)

Polymer sintering is fundamental to the rotomoulding process (Bellehumer, 2005; Chaudhary *et al.*, 2001; Sharma *et al.*, 2009). Much of the heating time is expended on polymer sintering and it also affects the final product properties, including the presence of bubbles (Sharma *et al.*, 2009). Chaudhary *et al.* (2001) define sintering as the coalescence of powder particles resulting in the formation of a consistent melt. Theoretical and experimental analysis shows that the most important aspects which affect polymer sintering phenomena in rotomoulding are melt viscosity, melt elasticity and surface tension (Chaudhary *et al.*, 2001; Bellehumer, 2005; Sharma *et al.*, 2009).

The melt flow index is usually specified for rotomoulding polymers (Crawford & Gibson, 2006; Beall, 1998). However, in terms of the melt viscosity, the zero-shear viscosity is more relevant in rotomoulding because it is a pressure and shear-free process (Bellehumer, 2005; Kontopoulou & Vlachopoulos, 1999; Crawford & Throne 2002). Resins with low zero-shear viscosities sinter easily and their flowability enables the filling of intricate mould details and good surface finishes (Kontopoulou & Vlachopoulos, 1999). A higher density of bubbles and poor surface finishes result from high viscosities (Kontopoulou & Vlachopoulos, 1999). Low melt elasticities are preferred because they facilitate faster sintering rates and fewer bubbles (Bellehumer, 2005).

2.1.3 Physical characteristics of rotomouldable materials

Rotomoulding materials are susceptible to oxidative thermal degradation as a result of exposure to high temperatures in the presence of oxygen for long periods. Thermal degradation impacts the mechanical properties of the products. Rotomoulding grades must contain much higher amounts of stabilising agents to reduce degradation (Beall, 1998).

Screening procedures for rotomoulding powder are usually the dry flow index, particle size distribution and bulk density (Crawford & Throne, 2002; Bellehumer, 2005).

The dry flow index, specified by the ASTM D-1895 standard, measures the time in which 100 g of powder flows through a standard funnel (Crawford & Throne, 2002). The dry flow index is an evaluation of the flowability of the powder in the mould, in other words, whether it will be able to reach all cavity areas. It is a function of particle size and shape (Crawford & Throne, 2002).

The bulk density is a measure of the packing ability of the powder (Crawford & Throne, 2002). The bulk density gives an indication of the initial size of the air cavities trapped within the powder which will form the bubbles and so it has an effect on the final bubble density. Good rotomoulding powder should have a high bulk density to limit the number of bubbles in the final product (Chaudhary *et al.*, 2001). A typical value for LLDPE is 320 kg/m³ (Crawford & Throne, 2002).

It is generally agreed that a narrow particle size distribution of rotomoulding powder of less than 500 µm (35 mesh) is adequate for the melting quality required for rotomoulding, and at the same time limits the pulverising costs (Crawford & Throne, 2002).

2.1.4 Technological advancements

Reduction of cycle times

One of the major drawbacks of the rotational moulding process is the long cycle times. Studies to address this drawback have been largely successful. Abdullah *et al.* (2009) reported significant cycle time reductions using various techniques such as surface-enhanced

moulds, internal mould pressure, internal mould cooling, water spray cooling, and higher oven air flow rates. Planes *et al.* (2008) formulated nanocomposites with lamellar graphite with enhanced thermal conductivity to enable reduction of cycle times. Chaudhary *et al.* (2001) showed that rotational moulding cycle times can be reduced for polyethylene by blending it with low molecular weight additives. These additives also resulted in the reduction of bubbles in the rotomoulded parts.

Process control

Initially, process control in rotomoulding was established by trial and error (Cramez *et al.*, 2002). Advances have now been made in process control. The Rotolog™ system was developed to facilitate process control and thus obtain products of consistent quality (Yan *et al.*, 2006). The Rotolog™ system measures the temperature inside the mould in real time (Crawford, 1996). It has been shown that there is a characteristic temperature profile for each polymer with a peak internal air temperature (PIAT) which results in products of consistent quality (Crawford, 1996). Other control systems have since been reported, including TempLogger™ (Roto Solutions, Hout Bay, South Africa) (Maplestone, 2008).

2.2 Static electricity

2.2.1 Definition of static electricity

Britton (1999) defines static electricity as the observable phenomena which emanates from electric charges, which can be stationary or in motion. The Electrostatic Discharge (ESD) Association defines the electrical charge caused by an excess or deficiency of electrons on a material surface as static electricity (ESD Association, 2010). From the two definitions, it is clear that ‘electrical charge’ is the key phrase.

Electrostatic charges are generated through triboelectrification (also referred to as contact charging), induction charging (Greason, 1992; Pavey, 2004; Pilkington, 1994), corona charging (Pavey, 2004), and conduction charging (Greason, 1992). Triboelectrification is considered to be the fundamental mechanism by which electrostatic charging occurs (Pavey, 2004). Triboelectrification is the most significant mechanism in most static electricity generation problems (Greason, 1992; Chubb, 1999).

2.2.2 Triboelectrification

Triboelectrification originates from ‘tribo’, a Greek word which means rubbing (Harper, 1970), and ‘electricity’ which comes from the Greek word for amber (Pionteck, 2007). The Greek scientist Thales of Miletus observed that amber becomes charged after rubbing with animal fur (Pionteck, 2007), and so triboelectrification originally meant electrification by rubbing.

There is disagreement among scientists as to whether tribocharging (rubbing) or contact charging, which occurs when two surfaces are brought into close proximity and then separated, can be considered similar mechanisms for electrification (Castle & Incelet, 1997). Harper (1970) asserted that materials can be charged through contact electrification and rubbing, which he called frictional electrification. He suggested that triboelectrification be used to encompass both mechanisms when it is not known which one is dominant. Where energy was expended through friction, frictional electrification dominates; contact electrification occurs where there is contact and separation. In recent times triboelectrification has been used interchangeably to describe both mechanisms (Pavey, 2004; McCarty & Whitesides, 2008; Jian *et al.*, 2010). This was adopted in this study.

Charge transfer in triboelectrification

The mechanism by which charge transfer occurs during triboelectrification between conductors such as metals is widely known. Electron transfer occurs between metals in contact as a result of differences in metal work functions (Hogue *et al.*, 2004; Pavey, 2004). The work function is the energy required to move an electron from a surface to infinity. Electrons will move from higher energy levels (lower work function) to lower energy levels (higher work function).

However, the mechanisms by which charge transfer occur between conductors and insulators and between insulators and insulators are still a matter of scientific debate. Some propositions have been made which partially correlate with the observed results. Some researchers argue that charge transfer between a conductor and an insulator occurs through the transfer of electrons, whereas others argue that it is through ion transfer and bulk material transfer (Harper, 1970; Hogue *et al.*, 2004; McCarty & Whitesides, 2008).

Liquids become electrostatically charged through the double layer mechanism (Pavey, 2004; Mulligan, 2003). Actions such as filtration and pumping can increase the charge density significantly (Leonard, 1981).

2.2.3 Hazards associated with static electricity

Static electricity has been fundamental in many inventions in the past century, and looks set to form the basis of more inventions in the future (Castle, 2001). These include air pollution control using electrostatic precipitators, xerography and electrostatic coating (Castle, 2001). However, static electricity is also a source of serious hazards. Charged objects develop huge electrical potentials relative to uncharged objects.

Electrostatic discharge

The transfer of electrons between objects at different electrical potentials constitutes an electrostatic discharge (ESD) event (ESD Association, 2010). An ESD event occurs so as to achieve electrical neutrality or dynamic electrical equilibrium. Two forms of electrostatic discharges can be distinguished: charge dissipation through a conductive pathway, either through the bulk of the material or its surface, and gas discharges (Lüttgens & Wilson, 1997).

Where electrically conductive materials are involved and they are grounded, that is electrically connected to the earth, the charge developed on the surface is dissipated to the earth, either through the bulk or the surface of the material, as the earth is at zero potential. In fact, grounding electrically conductive objects is the primary way of controlling static electricity by dissipating the charge and ensuring that dangerous potentials do not build up (Britton, 1999).

In instances where electrically insulative materials such as most polymers are involved, electrostatic charging develops very high potentials up to 30 000 to 40 000 volts, depending on other factors such as the nature of the materials and humidity (Grob & Minder, 1999). The voltage builds up because there are no conductive pathways through which the charge can be dissipated, even when the object is grounded.

A potential difference can result between the charged material and another material in close proximity. If the potential difference is high enough, the dielectric strength of the medium between the materials can break down, resulting in its ionisation (Lüttgens & Wilson, 1997). This allows charge flow between the materials, which constitutes a current, and this is termed gas discharge. The nature of the discharge is, however, dependent on the types of material, their shape and conditions such as humidity (Pavey, 2004). The dielectric strength of air is 3 MV/m.

Static electricity becomes hazardous as a result of uncontrolled electrostatic discharges. Electrostatic discharges can damage electronic equipment, produce shocks which can severely harm personnel and be of an incendiary nature. The increased use of polymers in various industries exacerbates the risks associated with static electricity as these materials find their way into many uses such as packaging.

Electrostatic discharges can affect electronic equipment directly and indirectly (Takai *et al.*, 1998). The direct effect emanates from the discharge current flow which disrupts the proper functioning of a component. Electromagnetic impulses resulting from ESD cause the indirect effect through electromagnetic interference.

Gas discharges and their incendivity

‘Incendivity’ is the igniting ability. Incendive discharges are of great concern in situations which involve flammable and explosive materials such as fuels. These can arise from the use of fuel containers, pipes or pneumatic conveyance systems.

The conventional way of assessing the incendivity risks of discharges is to compare their total energy with the minimum ignition energy of the particular flammable atmosphere using a capacitative circuit (Gibson, 1997).

Corona discharges

These occur on a sharp conductor at a high potential or from a charged object to an earthed sharp object (Pavey, 2004; Gibson, 1997). The gap in between does not fully ionise because

of the non-uniformity of the electric field; as a result, the energy of the discharge is low, as is its incendivity (Pavey, 2004; Gibson, 1997).

Spark discharges

These occur between two conductors at different potentials (Pavey, 2004; Gibson, 1997). All charge is transferred in a single discharge event (Pavey, 2004), releasing all the energy on the conductor (Gibson, 1997).

Brush discharges

These occur from a charged insulator to a rounded electrode (Gibson, 1997). The discharge is not a single event, because the charge cannot flow through or on the insulator. Discrete discharges occur from the surface simultaneously, often forming a single channel above the surface (Pavey, 2004). Experimental evidence shows that brush discharges are capable of igniting flammable gases and vapours in air even if the minimum ignition energy is less than about 3-4 mJ (Pavey, 2004; Glor, 1981).

Propagating brush discharges

These occur as a result of the development of high charge densities of opposite polarities on either sides of a thin insulating material when the material is brought into close proximity to an earthed conductor. These discharges are of high energy (they can exceed 1 J) (Pavey, 2004), and they can ignite flammable atmospheres (Gibson, 1997).

Cone discharges

These discharges occur across highly charged insulating powder materials in a heap (Pavey, 2004). The energy of cone discharges is higher than that of brush discharges and is capable of igniting flammable atmospheres (Pavey, 2004).

The nature of these gas discharges show that insulating plastic materials such as polyethylene poses a risk when they are used in flammable environments as brush or

propagating brush discharges can occur. Also, incendive spark discharges from highly charged low-resistivity liquids (such as petroleum products) are possible when insulating materials such as plastics are used to contain them and they cannot dissipate charge to the earth (Gibson, 1997).

2.2.4 Antistatic materials

Fowler (1988) defined an antistatic material as a material whose susceptibility to triboelectrification is low. Triboelectrification is the charging of materials due to rubbing or contact and separation. Because there are many different circumstances in which a material can be charged (for instance humidity, nature of second material, contact area), there is no test method suitable for characterising the charging propensity, i.e. ‘antistatic’ nature, of a material (Carter, 2010). However, electrically conductive materials can dissipate charge to lower potentials. Thus the electrical conductivity of a material is important as it enables the voltage build-up to be minimised by dissipating the charge, but it does not give an indication of the charging propensity (Grasso *et al.*, 1985). Two methods widely used to measure the conductivity of materials for static protection are surface resistivity and charge decay (Grasso *et al.*, 1985).

Electrical resistivity and conductivity

The following definitions are specified by the IEC 61340-2-3 standard:

Volume resistance (R_v)

This is the ratio of a DC voltage (V) applied between two electrodes placed on two opposite surfaces of a specimen and the steady-state current (A) between the electrodes. It is measured in ohms (Ω)

$$R_v = \frac{V}{I} \tag{2-2}$$

Volume resistivity (ρ_v)

This is the ratio of the DC field strength (V/m) to the steady-state current density (A/m^2) within the material. It is equal to the volume resistance of a cube with unit length, having the electrodes at two opposite surfaces. Volume resistivity is proportional to the cross-sectional area of the specimen and indirectly proportional to the length of the specimen, i.e.:

$$\rho_v = \frac{A}{L} R \quad (2-3)$$

The volume conductivity is the reciprocal of volume resistivity, given in Siemens/metre (S/m).

Surface resistance (R_s)

This is the ratio of a DC voltage (V) applied between two electrodes on a surface of a specimen and the current (A) between the electrodes.

Surface resistivity (ρ_s)

The surface resistivity is equal to the surface resistance of a square area having the electrodes at two opposite sides. The unit of surface resistivity is the ohm (Ω), according to the IEC 61340-2-3 standard, but it is sometimes referred to as ohms per square (Ω/\square). The surface conductivity is the reciprocal of the surface resistivity, measured in Siemens per square or just Siemens.

A specimen with high surface resistivity or high volume resistivity has low surface conductivity or low volume conductivity respectively. The opposite is true. Fowler (1988) and Groop *et al.* (2003) have shown that there is no correlation between surface resistivity and triboelectrification (the main mode by which static electricity is known to build up). Surface resistivity is, however, an important parameter, because it can be known if the material is able to safely dissipate the charge.

In the technical literature, ‘antistatic’ is used to describe materials with surface resistivities low enough to dissipate charge (Grasso *et al.*, 1998). However, standards which pertain to protection from static electricity hazards, for instance IEC 61340-5-1, categorise materials as being conductive, static dissipative and insulative, with respect to their surface resistivities. Static dissipative materials can only dissipate the charge if they are in contact with other materials at a lower potential, or the earth, which is regarded to be at zero potential. Table 2-1 shows the classification of packaging materials to be used in ESD applications, according to their surface resistance using the IEC 61340-5-1 standard.

Table 2-1 Classification of ESD materials (IEC 61340-5-1)

Material	Required range: Surface resistance (R_s) [Ω]
Insulator	$R_s \geq 1 \times 10^{11}$
Static dissipative	$1 \times 10^5 \leq R_s < 1 \times 10^{11}$
Conductive	$1 \times 10^2 \leq R_s < 1 \times 10^5$

Static charge decay

Another way used to quantify the effectiveness in charge dissipation is static charge decay (Grasso *et al.*, 1998). This method evaluates how fast a charge put on a surface of a specimen is dissipated. For a material to pass this test it must dissipate the charge in a specified time. Federal Test Method Standard No. 101C, Method 4046.1, “Electrostatic Properties of Materials”, specifies such a method (Grasso *et al.*, 1998).

2.3 Static dissipative thermoplastics

Most polymers are inherently electrically insulative because of the paucity (and limited mobility) of charge carriers (Jian *et al.*, 2010). The versatility of polymers has widened the scope of their applications in recent years. Their high inherent electrical resistances are useful in many applications such as electrical insulation. However, they also have drawbacks in applications such as fuel-handling systems such as fuel containers, due to the risk of static electricity. Conductive and electrically dissipating polymers are highly sought after for applications such as electromagnetic shielding and antistatic applications.

As mentioned in section 1.2, polymers can be rendered electrostatically dissipative in several ways (Rosner, 2001), but studies specific to rotomoulding applications are rare (Kelly III & Jones, 2002; Angelico 2011; Patch 2001). Antistatic agents, intrinsically conductive polymers (ICPs), inherently dissipative polymers (IDPs) and conductive particulates are commonly used (Rosner, 2001).

2.3.1 Non-particulate conductive fillers

Antistatic agents

These are hygroscopic surfactants (Murphy, 2001) . ‘Surfactant’ is an acronym for ‘surface active agent’. They have a hydrophobic tail and a hydrophilic head, which migrates to and aligns itself with the surface. The hydrophilic head interacts with contaminants, ions and water, forming a conductive pathway through which electrons can flow, thereby increasing the surface conductivity. Examples of antistatic agents given by Murphy (2001) are shown in Table 2-2 below.

Table 2-2 Antistatic agents (Murphy, 2001)

Sub-category	Antistatic agents
Cationic	Alkyl ammonium salts, glycerol stearate, acid esters, ethoxylated amines
Anionic	Alkyl salts of alkyl sulphonic, phosphonic or carboxylic acids
Non-ionic	Ethoxylated alkyl amines and amides, fatty acid esters, esters and ethers of polyols

A distinction is made between external and internal antistatic agents. External antistatic agents are applied on the surface of the polymer by spraying, painting or dipping to impart low surface resistivity. Internal antistatic agents are incorporated into the polymer during compounding and migrate or ‘bloom’ out during the service life or during manufacture of the polymer, to impart low surface resistivity. Their amphiphilic nature enables partial compatibility of the polymer matrix with the hydrophobic tail, while the hydrophilic head is aligned with the surface.

Antistatic agents have been used with success in thermoplastics and they are relatively cheap (Rosner, 2001). However, they do have drawbacks, such as the dependence of their functionality on a minimum relative humidity. Antistatic agents can also be rubbed off,

washed off or wiped off with time. Internal antistatic agents are replenished by blooming (Rosner, 2001) to the surface, but with time they will be exhausted. Thus they do not provide permanent protection. Antistatic agents can contaminate products because of their migratory nature. High volatility further limits their use in the rotomoulding process (Dahman, 2003).

Inherently dissipative polymers

Inherently dissipative polymers (IDPs) are typically copolymers (Rosner, 2001; Campbell & Tan, 1995; Dahman, 2003). These contain ether oxygens in their molecular backbones that are able to form complexes with cationic species, thereby invoking ionic charge transfer (Campbell & Tan, 1995). Charges can move from one oxygen to the other as a result of the mobility of ether chains.

When combined with thermoplastic matrices, IDPs form an interpenetrating network within the polymer matrix, thereby providing static dissipative pathways (Jennifer, 2008). Processing has to be done carefully in order to obtain the interpenetrating network necessary for static dissipation (Rosner, 2001; Dahman, 2003).

Examples include polyethylene dioxide (PEO) (Rosner, 2001), polyurethanes like the one described in the patent by Kolycheck *et al.* (1992) and also a copolymer consisting of 60–95% polyethylene oxide and 5–40% epichlorohydrine components in the patent by Yu (1990). Du point's Entira™ is an IDP based on an ethylene ionomer, which makes it compatible with polyolefin-based polymers (Hausmann, 2007). It is said to be suitable for applications which include blow moulding bottles and multilayer films.

Advantages of IDPs include their ability to impart surface resistivities in the range 10^8 - 10^{12} Ω/\square , independence from humidity in their operation, colourability and their non-migratory nature as they are large molecules (Campbell & Tan, 1995; Jennifer, 2008; Rosner, 2001). Thus they are non-blooming and provide permanent static dissipation. Also, the incorporation of IDPs does not significantly change the mechanical properties of many thermoplastics (Rosner, 2001). In the work by Dahman (2003), injection-moulded samples of polycarbonate/acrylonitrile butadiene styrene (PC/ABS) with IDPs were compared to those of

neat PC/ABS. The IDPs/PC/ABS blends had increased impact strength and moderately reduced tensile strength and stiffness

The thermal stability of IDPs is limited to 250 °C (Campbell & Tan, 1995), which again is a cause for concern in the high-temperature rotomoulding moulding process.

Intrinsically conductive polymers

Electrical conductivity in intrinsically conducting polymers (ICPs) evolves from π electron conjugation in their bonding structure (Bhadra *et al.*, 2009). Conjugation occurs in a molecule when there are alternating single and double bonds. This results in the delocalisation of the π electrons, which brings about limited electrical conductivity, as electrons cannot move through the whole chain length (Rosner, 2001). To obtain metal-like conductivity from the ICP it must be doped (Rosner, 2001). Doping is the formation of a conductive complex between the ICP and a guest species (Dahman, 2003).

Among ICPs, polyaniline (PAni) is the most extensively studied (Ameen *et al.*, 2010). Numerous researchers have synthesised blends of thermoplastics and PAni and obtained conductivities well within the static dissipative range, for instance Martins & De Paoli (2005), Chipara *et al.* (2003), and Cote *et al.* (2009). Deterioration in the mechanical properties was always observed in these blends. However, in a study by Dahman (2003) with an undisclosed ICP and a thermoplastic, the injection-moulded samples had consistent resistivity values in the static dissipative range, with no sudden drop with an increase in ICP content. The mechanical properties of the thermoplastic/ICP blends deteriorated with an increase in ICP content, but were almost similar to those of the matrix polymer.

It was reported that a rotomouldable blend of PAni/thermoplastic is technically feasible (Rosato, 2007). However, rotomoulding is a high-temperature process, and recent studies have shown that PAni is thermally unstable, which serves to demonstrate that ICPs cannot be rotomoulded. In the work by Dahman (2003) the surface resistivity of ICP/thermoplastic was shown to be thermally unstable, increasing by two orders of magnitude after being kept at 80 °C for a year. Thus ESD protection lasts only for a limited period. Studies by Ansari & Keivani (2006), and Bhadra *et al.* (2008) also showed that there

was a significant decrease and even total loss in conductivity for PANi which was heat treated at $> 150\text{ }^{\circ}\text{C}$ for prolonged periods.

The use of ICPs as antistatic additives has decreased, with Panipol Oy, the leading producer of PANi (Rosato, 2007), stopping the production of the PANi additive (Jennifer, 2008).

2.3.2 Particulate conductive additives

Due to the limitations of non-particulate conductive additives highlighted in the previous sections, conductive particulate fillers such as graphite are an attractive option for rotomoulding.

Conduction mechanism and percolation

For a polymer composite based on an insulating matrix filled with conductive particles, the variation of the electrical resistivity with filler loading follows a universal trend (Struèmpler & Glatz-Reichenbach, 1999; Omastova *et al.*, 1999; Clingerman *et al.*, 2000; Rosner, 2001). At low filler loadings the conductive particles are well separated by the polymer matrix and do not make contact with each other. In this composition range the resistivity barely decreases with filler loading. Above critical filler loading there is enough of the filler present so that a three-dimensional conductive network of touching conducting particles forms. This is the so-called percolation threshold and the resistivity decreases abruptly by several orders of magnitude. Beyond the percolation threshold the resistivity decrease levels off and adding more of the conductive filler makes little difference. Figure 2-3 illustrates the percolation phenomenon.

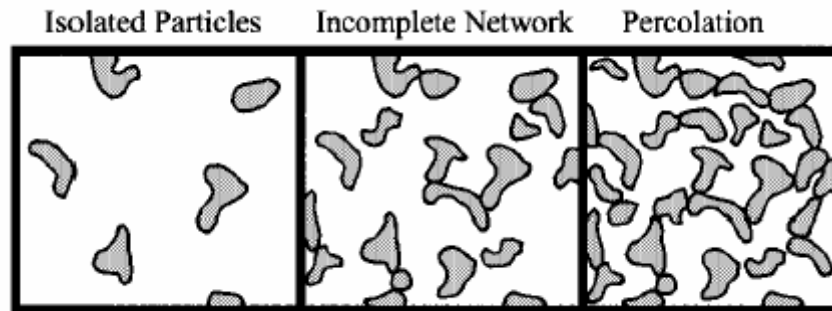


Figure 2-3 Percolation of a conductive filler in an insulating matrix (Rosner, 2001)

Several geometric, statistical and thermodynamic percolation models have been proposed to describe the conductivity of composites (Lux, 1993). The classical statistical percolation model originally proposed by Kirkpatrick & Zallen is often used to predict the conductivity of composites consisting of dispersed conductive particulates in insulating matrices (Lux, 1993). This model gives the dependence of conductivity near the percolation threshold as a power law (Wycisk *et al.*, 2002):

$$\sigma = \sigma_c (v - v_c)^t \quad (2-4)$$

where σ_c is the conductivity of the conductive additive, v is the volume fraction of the conductive additive, t is a critical exponent of a universal character, v_c is the percolation threshold.

The classical percolation model does not correlate with all experimentally observed results (Omastova *et al.*, 1999; Clingerman *et al.*, 2000), but it forms the basis of most other models (Clingerman *et al.*, 2000). The models do not take into consideration all the factors that are known to affect the percolation threshold and conductivity of the composites, hence their limitations in predicting conductivity. Physical filler properties that include the type, size, shape and surface properties and also physical polymer matrix properties affect composite conductivity (Struèmpler & Glatz-Reichenbach, 1999; Clingerman *et al.*, 2000). The contact resistance at the interface of the polymer matrices and fillers also plays an important role in the conductivity of the composite, particularly nanocomposites (Zeng *et al.*, 2010).

2.4 Graphite

Graphite is an allotrope of carbon, others being diamond and fullerenes (Chung, 2002). The word *graphite* is derived from the Greek word *graphein*, which means ‘to write’, and relates to the use of graphite for writing and drawing, particularly in pencils (Pierson, 1993).

2.4.1 Graphite structure

Graphite consists of planar hexagonal units of covalently bonded sp^2 hybridised carbon atoms stacked together through weak van der Waals forces. The one-atom-thick planar hexagonal units of covalently bonded sp^2 hybridised carbon atoms are referred to as graphene layers (Chung, 2002).

The electronic configuration of carbon is $1s\ 2s^2\ 2p^2$. Carbon atoms have four valence electrons. In graphite, sp^2 hybridisation results in three sp orbitals and one p orbital. The three sp orbitals form sigma bonds by overlapping between the carbon atoms. The remaining p orbitals from each carbon atom form a delocalised π electron orbital, which stabilises the in-plane carbon bonding (Chung, 2002). The π electrons are delocalised throughout the immediate graphene layers (Asbury Carbons, 2011). The graphene layers are bound together by weak van der Waals forces (Chung, 2002) which emanate from the interacting force fields of the π electron networks of adjacent graphene layers (Asbury Carbons, 2011).

The interlayer spacing between graphene layers is 0.335 nm. The stacking of graphene layers in graphite can occur in an -ABABAB- sequence (hexagonal graphite) or -ABCABC- sequence (rhombohedral graphite). The hexagonal graphite structure is the most common crystal structure; the rhombohedral structure is not thermodynamically stable (Pierson, 1993).

2.4.2 Graphite properties

As a result of the nature of its bonding, graphite exhibits anisotropic properties. Thus graphite is highly electrically conductive in the in-plane direction due to the delocalised electrons, and poorly conductive perpendicular to the layers (c -axis), as a result of the weak interlayer van der Waals forces (Chung, 2002). It is also highly thermally conductive in the in-plane direction, due to the easier propagation of phonons in the covalently bonded in-plane

direction. However, it exhibits low thermal conductivity perpendicular to the layers as a result of the difficulty of phonons to travel in this direction (Burchel, 2001). Typical graphite properties are given in Table 2-3, although these are highly dependent on the type of graphite.

Table 2-3 Graphite properties

Property	Value		Unit	Reference
	<i>In-plane</i>	<i>C-axis</i>		
Resistivity	2.5-5.0	3000	$\mu\Omega\text{m}$	(Pierson, 1993)
Young's modulus	1 000	36.5	GPa	(Pierson, 1993)
Thermal conductivity	3 000	6	W/mK	(Sengupta <i>et al.</i> , 2011)
Strength	130		GPa	(Sengupta <i>et al.</i> , 2011)
Density	2.26		g/cm^3	(Sengupta <i>et al.</i> , 2011)

2.4.3 Graphite types

Graphite is classified into natural and synthetic graphite (Wissler, 2006). Natural graphite is further divided into microcrystalline and macrocrystalline graphite. Microcrystalline graphite is also known as amorphous graphite; it has a low crystallinity and purity, and thus low conductivity (Wissler, 2006).

Macrocrystalline graphite is divided into flake graphite and vein graphite. Macrocrystalline graphite consists of large crystals, with the crystals being oriented in a lamella shape in flake graphite and chip-like shape in the vein graphite. Flake graphite and vein graphite have conductivities suitable for electrochemical applications (Wissler, 2006).

Synthetic graphite is divided into primary and secondary synthetic graphite. Primary synthetic graphites have consistent qualities compared to secondary graphite (Wissler, 2006).

2.4.4 Occurrence and production of natural graphite

Although the occurrence of natural graphite is worldwide, countries listed in Table 2-4 had deposits of significant commercial interest in 2001. Estimates of graphite production output in 2001 are also included in Table 2-4 (Kalyoncu & Taylor, 2005). The natural graphite used in this investigation comes from Zimbabwe. Zimbabwean graphite is crystalline flake graphite and comes from a single mine, the Lynx graphite mine.

Mined graphite is purified from the ore by a wide range of techniques, which usually begin with crushing and grinding, and then go on to processes such as flotation or leaching (Kalyoncu & Taylor, 2005).

Table 2-4 Graphite occurrence and production in 2011 (Kalyoncu & Taylor, 2005)

Country	Graphite production (Kt)
Austria	12
Brazil	72
Canada	25
China	450
Germany	0.3
Madagascar	40.3
Mexico	30
North Korea	25
Norway	2.5
Russia	6
Sri Lanka	6
Ukraine	7.5
Zimbabwe	10

2.4.5 Graphite intercalation compounds

Graphite intercalation compounds (GICs), also known as expandable graphite, are formed by introducing a chemical species, atomic or molecular, between the stacked graphene layers of graphite (Dresselhaus & Dresselhaus, 2002). Intercalation of the species into the graphene layers occurs through reduction or oxidation of the π electron network, depending on whether the species is electronegative or electropositive. Electronegative species will accept electrons from the π electron network, forming acceptor type GICs, whereas compounds formed by electron donors, e.g. metals, are donor GICs (Noel & Santhanam, 1998). Intercalation of some species into graphite can be used to modify some properties of graphite, for instance increase the conductivity (Dresselhaus & Dresselhaus, 2002).

2.4.6 Expanded graphite

Upon exposure to heat, the interlayer spacing of some GICs increases forming expanded graphite (Chung, 2002). The interlayer spacing between some of the graphene layers is increased as a result of the vaporisation of the intercalate, resulting in the formation of gas

pockets (Chung, 2002). Irreversible expansion results in the bursting of the gas pockets, producing an elongated, worm-like structure (Chung, 2002). Expandable graphite is a good intumescent flame retardant for polyethylene (Xie & Qu, 2001) at a loading of 10 wt.% and above.

The worm-like structure of expanded graphite is made up of an interconnected network of delaminated stacks of graphene nanoplatelets with pores which range from 10 nm to 10 μm (Chen *et al.*, 2002). Nanocomposites can be formed by the intercalation of some species in the pores, such as polymer molecules (Chen *et al.*, 2002). Expanded graphite has an increased packing volume compared to that of the GIC, but the in-plane electrical conductivity is the same as that of the natural flake graphite (Zheng *et al.*, 2004).

Graphite nanosheets or graphene nanoplatelets (GNs) are made of multiple stacked layers of graphene (Chen *et al.*, 2010). Graphite nanosheets have been produced from expanded graphite using an ultrasonic method (Chen *et al.*, 2004). GNs exhibit high aspect ratios of up to 500 (Chen *et al.*, 2003a).

2.4.7 Graphite applications

Natural graphite has numerous industrial applications as a result of its unique properties, viz. electrical and thermal conductivity, chemical inertness, thermal resistance and lubricity (Kalyoncu & Taylor, 2005). These include the fabrication of refractories, lubrication, brake linings, electrical applications including batteries and pencil making. The graphene layers can slide over each other as a result of the weak interlayer of van der Waals forces, hence its use as a lubricant and in pencils (Chung, 2002). Natural graphite is also used to make graphite intercalation compounds or expandable graphite.

The review by Dresselhaus & Dresselhaus (2002) underscores some of the technological applications envisaged and already applied for GICs. These include conductivity applications, as some GICs have high room-temperature conductivities.

Expanded graphite has a wide range of industrial applications (Chung, 1987). These include fire extinguisher agents, gaskets, seals and packings, electrodes and as a conductive additive for thermoplastic resins.

The various forms of graphite have been exploited as fillers for imparting thermal and electrical conductivity in plastics. Interest in expandable graphite as an intumescent flame retardant additive in plastics has been heightened by the advent of new regulations the world over limiting the use of halogen-based flame retardants (Duquesn *et al.*, 2003).

2.5 Electrical conductivity of graphite/thermoplastic composites

Numerous studies on the electrical conductivity of thermoplastic/graphite composites have been done (Krupa & Chodak, 2001; Thongruang *et al.*, 2002a; Panwar & Mehra, 2008; Bhattacharya *et al.*, 2009). Varying conductivity percolation thresholds and conductivity levels were reported. The factors which influence the electrical conductivity are reviewed in the following sections.

2.5.1 Effect of filler aspect ratio

The filler shape defines the aspect ratio (the length:diameter ratio for fibres and the diameter:thickness ratio for platelets). High aspect ratio fillers such as fibres and flakes form conductive pathways in polymer matrices at low concentrations, thus their percolation thresholds are relatively low compared to particulates with low aspect ratios.

Bigg (1979) investigated the effect of aspect ratio on the electrical conductivity of metal-filled composites. An increase in the aspect ratio of metal fibres resulted in a decrease in the filler content required to attain electrical conductivity. Resistivities of 20 Ω .cm were obtained with aluminium fibres having an aspect ratio of 24. The results of Nagata *et al.* (1999) on the conductivity of solution-compounded, hot-rolled LDPE/graphite composites using spherical and platelet graphite further demonstrates the effect of aspect ratio on electrical conductivity. Spherical graphite only attained the percolation threshold at 29 vol.%, compared to platelet graphite which attained percolation thresholds at graphite contents as low as 13 vol.%.

Various researchers, for instance Chen *et al.* (2002), Chen *et al.* (2003a; 2007) and Shen *et al.* (2005) have shown that thermoplastic/graphite nanocomposites have relatively low percolation thresholds. The high conductivity was attributed to high aspect ratios of graphite nanoplatelets.

Chen *et al.* (2002) attained the conductivity percolation threshold at a low expanded graphite content of 0.67 vol.% in maleic anhydride grafted polypropylene (gPP)/expanded graphite (EG) nanocomposites prepared by solution intercalation. The electrical conductivity reached 10^{-3} S/cm when the EG concentration was 3.90 vol.%. SEM and TEM revealed the high aspect ratio in these composites.

In a comparative study by Chen *et al.* (2003a), graphite nanosheets with aspect ratios of between 100–500 and graphite powder (7 500 mesh) with aspect ratios of between 5-10 were used to prepare composites with PMMA. A percolation threshold of about 0.31 vol.% was attained with the high aspect ratio graphite nanosheets, compared to that of about 3 vol.% attained with graphite powder.

However, Kalaitzidou *et al.* (2010) observed no apparent effect on the percolation threshold even when there was a significant difference in the aspect ratios of graphite nanoplatelets (aspect ratios of 100 and 1 500). This was attributed to poor mixing, resulting in poor dispersion of the high aspect ratio platelets. Also, a significant number of the platelets assumed a bent or rolled up morphology, which reduced their apparent aspect ratios in the nanocomposites.

2.5.2 Effect of constituent conductivity of the filler

The filler type determines the constituent conductivity of the filler and ultimately the conductivity of the composite (Clingerman *et al.*, 2000). The anisotropic electrical conduction of graphite has been reviewed in the preceding sections.

2.5.3 Effect of polymer matrix properties on conductivity

The polymer matrix properties that influence the conductivity of the composites include its crystallinity, inherent conductivity and its surface energy (Clingerman *et al.*, 2000).

The results of Krupa & Chodak (2001) show the influence of polymer matrix crystallinity on conductivity. It is known that in semi-crystalline polymers the filler is only distributed in the amorphous regions, whereas in amorphous polymers it is distributed in the whole polymer. Lower percolation thresholds (6 and 11 vol.%) were obtained in high-density polyethylene (HDPE)/graphite composites, compared to the thresholds for polystyrene (PS)/graphite composites (12 and 13 vol.%) with two different graphite types respectively. Conductive networks were easily formed in the semi-crystalline HDPE. The results of Kalaitzidou *et al.* (2010) show the same trend.

However, in another study by Krupa *et al.* (2004), the difference in crystallinity between HDPE and LDPE did not result in significant differences in the percolation threshold and conductivity of the graphite composites with the same graphite particles as used in the previous study. The percolation threshold was 11 vol.% for both matrices. The graphite particles were apparently large enough not to cause any effect due to the difference in crystallinity.

The interaction between the polymer and the conductive filler is influenced by the surface energies of the constituents and also has an effect on the conductivity of the composites. Smaller differences in surface energies between the filler and the polymer will result in the effective wetting of the filler, hence large amounts of polymer coat the filler. When this happens, the filler is effectively dispersed and more particles will be required to establish a conductive pathway, thus the percolation threshold will be higher. A difference in surface energies between the filler and the polymer is thus desirable (Clingerman *et al.*, 2000).

2.5.4 Effect of particle size

Nagata *et al.* (1999) investigated the effect of graphite particle size and shape on the conductivity of solution-compounded, hot-rolled LDPE/graphite composites. They showed that the percolation threshold increased with the mean sizes of the platelet type graphite (Table 2-5). However, spherical particles exhibited the highest percolation thresholds, and these thresholds were independent of particle size.

Table 2-5 Variation of the percolation threshold with graphite particle size

Mean particle size (μm)	Percolation threshold (vol.%)
2.1	13.5
5.8	14.0
14.5	16.8
25.7	17.8
50.8	23.5
82.6	25.5
5.1*	29.2

*Spherical graphite particles

Krupa & Chodak (2001) also showed that smaller graphite particles give lower conductivity thresholds (6 vol.% compared to 11 vol.%) in high-density polyethylene (HDPE). However, there was no significant difference in the percolation thresholds due to differences in particle size in polystyrene (PS)/graphite composites, but the smaller particles resulted in higher conductivity.

A high percolation (34 wt.%) was also obtained by Chen *et al.* (2007) in HDPE/natural graphite composites. The graphite particles were much larger (7 500 mesh).

There has been much research interest in materials based on nanosized graphite nanosheets (GN) for use in polymer composites because of their perceived lower conductivity thresholds and better mechanical properties (Chen *et al.*, 2003b; Kalaitzidou *et al.*, 2007; 2010; Kim *et al.*, 2010; Pötschke *et al.*, 2010). For instance, Chen *et al.* (2003b) fabricated polystyrene (PS)/graphite nanosheet composite films with a percolation threshold close to 1 wt.%, compared to composites of PS with 7 500 mesh natural graphite which had a percolation threshold of 6 wt.%. Chen *et al.* (2003b) obtained the PS/GNs composites by in situ polymerisation of styrene in the presence of sonicated expanded graphite. This study also

shows the effect of the filler aspect ratio. The findings of other researchers who have done work on graphite/polymer nanocomposites are reviewed in subsequent sections, as the particle size is interrelated with other filler properties which influence the electrical conductivity.

2.5.6 Effect of processing

Graphite/thermoplastic composites prepared by the same methods with similar particle sizes show consistently low percolation thresholds. Bhattacharya *et al.* (2009) reported on HDPE/graphite composites prepared by tumble mixing 10–20 μm graphite particles with HDPE and subsequent compression moulding which had a percolation threshold of 1.13 vol.% (2 wt.%). Panwar & Mehra (2008) obtained a percolation threshold of 2.70 vol.% with graphite particles of 10–20 μm in HDPE/graphite particles tumble mixed and compression moulded.

However, different processing techniques distribute and orient the fillers differently, affecting the conductivity. The results of Bhattacharya *et al.* (2009) and Panwar & Mehra (2008) are in contrast with the results obtained by Thongruang *et al.* (2002a), in which a high percolation threshold of more than 50 wt.% was obtained in HDPE/graphite composites. The composites were prepared by mechanical mixing and subsequent compression moulding. This somewhat high percolation was attributed to an even dispersion of the graphite particles in the polymer matrix.

In another study by Thongruang *et al.* (2002b), the percolation threshold of HDPE/graphite composites was lowered by incorporating UHMWPE in the composites. This phenomenon was attributed to the preferential distribution of graphite in one of the polymer phases or at the interface of the polymer phases. This results in the *double percolation effect*, which is the percolation of the graphite in one of the phases and the continuity of that phase in the other polymer phase (Thongruang *et al.*, 2002b). This effect has also been observed in carbon black composites with polymer blends (Narkis *et al.*, 1999; Farshidfar *et al.*, 2006; Thongruang *et al.*, 2002b).

The methods by which graphite/thermoplastic nanocomposites are fabricated and processed appear to have a more pronounced effect on conductivity percolation thresholds. Solution intercalation is the common graphite/thermoplastic nanocomposites fabrication method (Kalaitzidou *et al.*, 2010). Numerous polymer/graphite nanocomposites have been prepared through solution intercalation of a monomer within the graphene layers and subsequent in situ polymerisation or the dissolution of a polymer into a solvent containing the graphene layers (Shen *et al.*, 2005; Xiao *et al.*, 2002; Fim *et al.*, 2010; Chen *et al.*, 2002; Wang *et al.*, 2006). The other methods are the coating method and the melt mixing method (Kalaitzidou *et al.*, 2010).

Shen *et al.* (2005) compared the effect of various methods used to prepare thermoplastic/graphite nanocomposites. They used solution intercalation, the masterbatch route and direct melt mixing to prepare polyethylene (PE)/maleic anhydride grafted PE (g-PE)/expanded graphite (EG) composites. The percolation thresholds were: solution intercalation (2.19 vol.%), masterbatch route (3.18 vol.%) and direct mixing (4.68 vol.%). The percolation threshold was even higher (5.35 vol.%) for the specimens without the maleic anhydride grafted PE (g-PE). The lower percolation thresholds were attributed to the preservation of the high aspect ratios of the graphite nanosheets by the processing methods.

The results of the study by Kalaitzidou *et al.* (2010) are consistent with the results of Shen *et al.* (2005). Kalaitzidou *et al.* (2010) also evaluated the effect of different methods of thermoplastic/graphite nanocomposite preparation by preparing polypropylene (PP)/graphite nanocomposites. The coating method produced conductivity values slightly better than the solution intercalation method (10^{-3} S/cm at a graphite loading of 3 vol.%). The two methods were significantly better than the melt compounding method which exhibited a conductivity of less than 10^{11} S/cm at 3 vol.%. The discrepancies in the nanocomposites' conductivity were explained in terms of differences in the effectiveness of the dispersion of the graphite nanosheets by the different fabrication methods and their effects on the structure of the graphite nanosheets. They showed that in the solution intercalation and coating methods the platelet structures of the graphite nanosheets and their aspect ratios are preserved. The dispersion of the graphite nanosheets in the polymer matrix was observed to be effective when the coating method was used compared to the melt mixing and the solution intercalation methods, in which agglomerates of graphite nanosheets were present.

The fabrication methods of the composites also affect the way the graphite platelets are oriented and the aspect ratios of the graphite nanoplatelets (Kalaitzidou *et al.*, 2010). Thus in injection moulding the graphite nanoplatelets were found to be oriented in the direction of the flow, which meant a high loading was required to establish the conductivity percolation threshold. Compared to compression moulding, the orientation is random and so a lower loading was reported to reach the percolation threshold.

2.6. Rotomoulded polymer thermoplastic composites

Studies of rotationally moulded polymeric composites have largely focused on the mechanical properties of the composites, although some have focused on achieving better processibility. This review focused on rotomoulded polymer composites that contain particulate or fibrous fillers. Other types of rotomoulded composites mentioned in the literature which contain structural supports such as inserts (Beall, 1998) are not part of this review.

2.6.1 Incorporation of the filler into the matrix

In the literature, three ways of incorporating the filler into the polymer matrix for rotomoulding applications were identified, namely:

- dry blending,
- melt compounding, and
- the multiple shot procedure (multiple dumping).

When dry blending is used, the filler and the polymer matrix are blended in a high-speed mixer before charging into the mould. Melt compounding involves a step in which the filler is mixed into the melt, usually in an extruder; the extrudate is then ground into a powder suitable for rotomoulding. In the multiple shot method (Yan *et al.*, 2006; Wesley, 1999), a layer of material is first moulded, after which another batch of material is charged and moulded, and this can be subsequently repeated. The drawbacks are the added costs (Yan *et al.*, 2006) and the disruptions in the processing (Wesley, 1999).

2.7 Mechanical properties of polymer composites

The modulus, yield strength and impact strength are the mechanical properties considered in most applications (DeArmitt & Hancock 2003). Polymer reinforcement is regarded as the simultaneous improvement of the modulus and strength (Xanthos, 2005).

2.7.1 Composite moduli

The inclusion of rigid filler particles into a polymer matrix enhances the Young's modulus due to differences in stiffness between the particles and the polymer matrix (Fu *et al.*, 2008). The tensile modulus of graphite in the in-plane is 1 TPa, and the c-axis value is 36.5 GPa (Pierson, 1993). The modulus of LLDPE is only up to hundreds of MPa (Kissin, 2005). It can therefore be expected that the inclusion of graphite in the polyethylene matrix increases its modulus.

Effect of filler loading

The modulus of composites increases with filler content due to the higher rigidity of the fillers compared with the matrix. This is the trend observed in most graphite/polymer composites.

Gaxiola *et al.* (2010) observed a significant increase in tensile and flexural moduli with an increase in synthetic graphite content in graphite-polypropylene composites. Akinci (2009) also obtained an increase in elastic modulus with an increase in graphite content up to 50 wt.% in injection-moulded graphite polypropylene composites. Yasmin & Daniel (2004) observed a 25% improvement in the elastic modulus of an epoxy (anhydride-cured diglycidyl ether of bisphenol A (DGEBA)) reinforced with graphite platelets at 25 wt.% content of the graphite platelets. George & Bhowmick (2008) observed an increase in the modulus of EVA and its strength with increasing concentrations of expanded graphite (EG). An improvement of 150% was observed in the modulus at 100% elongation. A significant improvement in the modulus of thermoplastic polyurethane was observed with an increase in graphite nanoplatelets (GNPs) content due to the stiffness of GNPs (Quan *et al.*, 2009). An improvement of 300% was observed at only 3.9 vol.% graphite nanoplatelets.

Effect of different matrices on the modulus

Reinforcement of a polymer matrix is dependent on its stiffness. The reinforcing effect is more pronounced in weaker matrices. True reinforcement occurs in elastomers (Móczó & Pukánszky, 2008). Graphite/polymer composites exhibit the same behaviour, as evidenced by the higher increase in the Young's modulus in low-density polyethylene (LDPE) compared to high-density polyethylene prepared by injection moulding (Krupa *et al.*, 2004). The modulus of HDPE is higher than that of LDPE.

Effect of filler properties on the modulus

Particle size and distribution

In the review by Fu *et al.* (2008), it was shown that there is a critical average particle size above which particulate filled composite modulus does not depend on filler particle size. Below this particle size, the modulus increases with a decrease in particle size. Although Fu *et al.* (2008) stress that the critical average particle size cannot be determined theoretically, this particle size was apparently in the nano range.

The trends observed by Fu *et al.* (2008) are not apparent in the results obtained in graphite polymer composites. In fact, the moduli appear to vary with all particle sizes, improving with a decrease in particle size for all particle size ranges, even in the micron range size.

Composites of HDPE and synthetic graphite prepared with smaller graphite particle sizes (d_{50} of 14.1 μm) exhibited higher moduli compared to those prepared with larger particle sizes (d_{50} of 31.6.1 μm) (Krupa & Chodák, 2001). The higher moduli in the composites with the smaller graphite particles were attributed to the enhanced interaction between the matrix and the graphite particles as a result of the huge surface area of smaller particles.

However, smaller particles have a tendency to form aggregates, which are detrimental to the mechanical properties of the composite. Matrices containing large particles can fail

prematurely as these easily debond from the matrix under loading (Móczó & Pukánszky, 2008).

Effect of filler shape

The reinforcing effectiveness of a filler is characterised by its surface area A to volume V ratio, which should be maximised for optimum reinforcement (Nugay *et al.*, 1997; Xanthos, 2005). The A/V ratio determines the area available for interaction between the filler and the polymer matrix.

An increase in the filler aspect ratio results in an increase in the A/V ratio (Xanthos, 2005). For the same volume, the A/V ratio of spherical particles is fixed, whereas that of anisotropic fillers such as fibres and platelets can be manipulated by changing the aspect ratio. Higher aspect ratio fillers therefore possess a relatively higher reinforcing effect (Móczó & Pukánszky, 2008). There is no ambiguity in that respect for graphite/polymer composites.

The results of Cho *et al.* (2007) show that the modulus of epoxy/graphite nanocomposites is highly dependent on the graphite filler aspect ratio. Composites processed with graphite with the highest aspect ratio of about 200 exhibited the best modulus values. The expanded graphite exhibited the highest aspect ratio, leading to nanocomposites with high modulus.

Zheng *et al.* (2004) observed an improvement of 17% in the tensile modulus of expanded graphite/HDPE composites at 3 wt.% expanded graphite content. In contrast, untreated graphite/HDPE composites in the same study attained only 10% improvement at 3 wt.% graphite loading. This discrepancy was due to the higher A/V ratio exhibited by expanded graphite. This was a result of the high aspect ratio of expanded graphite.

Effect of interfacial interactions

In the works reviewed by Fu *et al.* (2008), it was shown that the polymer matrix/particle interfacial adhesion had little effect on the Young's modulus. They concluded that because the Young's modulus was measured at relatively low deformations, the deformation was not sufficient to cause interface separation.

However, Zheng *et al.* (2004) observed marginal improvements (10 and 17% respectively) in tensile modulus and strength in both untreated and expanded graphite/HDPE composites. The marginal improvement was attributed to poor matrix-filler interface, which limited the load transfer from matrix to filler.

2.7.2 Composite strength

The strength of polymer composites is dependent on the stress transfer between the filler and the matrix (Fu *et al.*, 2008). The factors that influence the stress transfer are reviewed in the next sections.

Effect of filler properties

Particle size and distribution

The strength of particulate filled composites generally increases with decreasing particle size. This is attributed to the larger total surface area of smaller particles, which enables an efficient stress transfer mechanism (Fu *et al.*, 2008). Most polymer/graphite composites exhibit this trend.

The tensile strength of styrene-butadiene rubber (SBR)/graphite composites was observed to increase with a decrease in graphite particle size at a wide range of graphite contents (0-140 phr) (Ismail & Khalaf, 2011). The highest tensile strength values at the same graphite loading were exhibited by acrylonitrile butadiene rubber (NBR)/graphite composites made with the smallest graphite particle sizes, (sub-micron range) (Yang *et al.*, 2006). SEM revealed better adhesion between the small graphite particles used and the NBR. However,

aggregation was shown to limit the increase of the tensile strength with content of the sub-micron graphite. Graphite platelet agglomeration was also shown to deteriorate the tensile strength at higher graphite platelet loadings in epoxy (anhydride-cured diglycidyl ether of bisphenol A (DGEBA)) reinforced with graphite platelets (Yasmin & Daniel, 2004). An improvement of 21% in the strength at 2.5 wt.% was observed. But due to platelet agglomeration, at 5 wt.% the improvement was only 9%.

Particle shape

In an earlier section on the review of composite moduli it was discussed how the particle shape influences the filler surface area available for interaction with the polymer. Thus the filler aspect ratio also has an effect on the strength of the composite as it determines the surface area available for interaction. Higher aspect ratio fillers therefore possess a relatively higher reinforcing effect with respect to the composite strength (Móczó & Pukánszky, 2008).

Gaxiola *et al.* (2010) observed a decrease in both flexural and tensile strength with an increase in synthetic graphite content in PP due to the low aspect ratio of the graphite. Higher aspect ratio nanotubes used in the experiments exhibited an increase in both flexural and tensile strength with an increase in content at low loadings.

Effect of interfacial interactions

The composite strength and toughness are significantly influenced by the interfacial interactions. The interfacial adhesion between the polymer and the particle determines the load that will be transferred between the components. Good interfacial adhesion enables effective stress transfer, hence high strength is achieved. Poor bonding results in inefficient stress transfer at the particle/polymer interface. As a result of the poor bonding of the particle to the polymer matrix, a discontinuity in the form of debonding arises. The composite strength thus decreases with the addition of filler particles because the particle cannot carry any load. An increase in strength is observed in composites with well-bonded particles, particularly nanoparticles as they have higher surface areas for polymer interaction (Fu *et al.*, 2008).

Interfacial adhesion is frequently described by four theories: the theory of mechanical interlocking, the theory of interdiffusion, the theory of electrostatic interaction, and the theory of adsorption interaction (Pukánszky & Fekete, 1999). The theory of adsorption interaction is used mostly for the description of the interaction in filled polymers (Pukánszky & Fekete, 1999; Móczó & Pukánszky, 2008).

Wang *et al.* (2001) observed an increase in yield strength with an increase of graphite content up to 55 wt.% in graphite/HDPE composites with graphite treated with a silane coupling agent. The improved strength was attributed to the good dispersion of graphite particles and the increased interfacial interaction as a result of the pre-treatment.

Effect of filler loading

The composite strength depends on the filler loading; however, this dependence is interrelated to the filler particle size and polymer/filler interaction. Thus various trends were noticed in the composite strength variation with the filler loading (Fu *et al.*, 2008). This observation is consistent with the observations regarding the strength of graphite/polymer composites.

An improvement in the tensile strength of 36% was observed with a concentration of 4 phr in composites of expanded graphite and EVA. However, at a graphite content of 8 phr, tensile strength decreased by 17% as a result of agglomerations (George & Bhowmick, 2008). The tensile strength of polystyrene/expanded graphite composites gradually increased with graphite content before levelling off at about 27% improvement at 5 wt.% content graphite (Chen *et al.*, 2001). An increase in tensile strength with an increase in expanded graphite content was also observed up to 4 wt.% expanded graphite in HPDE/graphite nanocomposites, after which the strength started to decline (She *et al.*, 2007). After 4 wt.% the mobility of the HDPE molecules was restricted, thus they could not dissipate mechanical energy, and therefore there was reduction in strength (She *et al.*, 2007).

Akinci (2009) also observed a decrease in tensile strength with an increase in graphite content in graphite/polypropylene composites. This was attributed to the immobilisation of polymer chains by the filler. The stress at break of graphite composites with polystyrene and

polyethylene (Krupa & Chodák, 2001; Krupa *et al.*, 2004) showed an initial decrease, then an increase, with graphite content.

Uhl *et al.* (2005) used melt blending to prepare composites of polyamide-6 (PA-6)/graphites with virgin graphite, different expandable graphites (GICs) and expanded graphite. There was deterioration in the tensile strength for all types of graphite at all loadings. However, the deterioration of tensile strength was lower in composites prepared with virgin and expanded graphite compared to the ones prepared with GICs, due to the evolution of sulphuric acid from the GICs and the degradation of PA-6.

2.7.3 Impact strength

Dewetting and crazing phenomena are mainly responsible for the impact strength of particulate-filled polymers (Nielsen & Landel, 1994). Filler particles are responsible for crack initiation and these are easily propagated in rigid polymers, thus reducing the impact strength (Nielsen & Landel, 1994).

Effect of polymer matrices, particle characteristics and interfacial interactions

Rigid fillers can either decrease or improve the impact strength of filled polymers. They decrease the impact strength of elastomeric polymers (DeArmitt & Hancock, 2003). However, they may improve the impact strength of rigid polymers through the promotion of crazing. Soft or rubbery fillers improve the impact strength of rigid polymers (DeArmitt & Hancock 2003; Nielsen & Landel, 1994).

The impact strength of graphite/HDPE composites was observed to decrease with graphite content because the graphite is more rigid compared to the matrix (Wang *et al.*, 2001).

Good adhesion between the phases is a prerequisite for the improvement of the impact strength of rigid polymers filled with elastomeric particles (Nielsen & Landel, 1994). Poor interfacial adhesion and dispersion appeared to be the cause of the decrease in impact strength in polystyrene/expanded graphite composites (Chen *et al.*, 2001).

A sharp decrease in Izod notched impact strength of expanded graphite/HDPE composites with filler loading up to 3 wt.% was observed; thereafter it levelled off (She *et al.*, 2007). Poor affinity between graphite and the matrix might have caused the decrease in impact strength. It is believed that the expanded graphite could have been polar due to some functional groups such as -COOH and C-OH formed on the surface of the EG, whereas the matrix is apolar. FTIR results appeared to confirm this.

It was reported that increased aspect ratio resulted in a decrease in falling weight impact strength (DeArmitt & Hancock, 2003).

Effect of particle size

The impact strength of particulate-filled polymer composites increases with a decrease in filler particle size (Nielsen & Landel, 1994). The improvement of the impact strength in composites with well-dispersed small particles is attributed to a crack-pinning mechanism (DeArmitt & Hancock, 2003). However, the impact strength will deteriorate at a very small particle size due to agglomeration (Nielsen & Landel, 1994). Agglomerates and large particles act as flaws (DeArmitt & Hancock, 2003). High impact strengths were obtained with better dispersion of expanded graphite (Chen *et al.*, 2001) in polystyrene/expanded graphite composites.

2.7.4 Influence of composite structure on mechanical properties

In their review, Móczó & Pukánszky (2008) underlined the fact that filler particle characteristics and composition and the processing technique are principally responsible for the composite structure. They noted that the important aspects that affect composite structure are homogeneity, attrition of the filler, aggregation and orientation of the anisotropic fillers.

Uniform dispersion of the filler is critical to achieving enhanced mechanical properties of the composites. In most reports on the graphite/polymer composites encountered, those that contained well-dispersed graphite particles showed improved mechanical properties, for instance Yasmin *et al.* (2006), Chen *et al.* (2001), Wang *et al.* (2001).

George & Bhowmick (2008) observed deterioration in the mechanical properties of EVA composites with natural graphite as a result of poor dispersion and subsequent agglomeration of the natural graphite particles, thereby forming weak points in the composites.

Epoxy/graphite nanocomposites prepared by different techniques, i.e. direct, sonication, shear and combined sonication and shear mixing all show a higher modulus compared to the epoxy matrix (Yasmin *et al.*, 2006). However, of all the individual processing methods used, shear mixing was able to exfoliate and disperse graphite nanosheets effectively, leading to the best mechanical properties with respect to the modulus. The good dispersion of the nanosized graphite particles and good interfacial adhesion between the expanded graphite particles and epoxy matrix restrict the mobility of polymer chains under loading, thereby improving the modulus.

In the previous sections it was noted that aggregation is detrimental to all the mechanical properties of graphite/polymer composite. The difference in magnitude between the forces attempting to separate the particles and those attempting to hold them together influences the occurrence of aggregation (Móczó & Pukánszky 2008). Aggregation can be reduced by increasing the shear rate and the particle size. It can also be reduced by decreasing the surface tension and reversible work of adhesion of the polymer melt through surface treatments (Móczó & Pukánszky 2008). Wang *et al.* (2001) attained good dispersion of graphite in HDPE matrix by using a silane coupling agent.

Attrition of the filler causes a change in the filler dimensions. This can have an impact on the aspect ratio, whose influence on mechanical properties has already been discussed.

The flow patterns and shear forces developed during processing determine the orientation of anisotropic particles (Móczó & Pukánszky, 2008). The mechanical properties are to a large extent influenced by the average orientation of particles relative to the direction of the external load (Móczó & Pukánszky, 2008). The modulus, strength and impact strength can be improved by increased alignment (Móczó & Pukánszky, 2008). Yasmin *et al.* (2006) ascribed the stiffening effect in expanded graphite/epoxy composites to be likely from the orientation of graphite platelets and polymer chains.

Verbeek & Focke (2002) showed that porosity is a key factor in the mechanical properties of the composite. Voids deteriorate the mechanical properties because they do not carry any load.

Inclusion of filler in a polymer matrix can influence its crystallisation characteristics by increasing the rate of cooling and nucleating crystallisation, and changing the degree of crystallisation (DeArmitt & Hancock, 2003). The degree of crystallinity influences the mechanical properties of the composite as the crystalline phase has a higher modulus than the amorphous phase (DeArmitt & Hancock, 2003). The yield strength was reported to be proportional to the heat of crystallisation (DeArmitt & Hancock 2003).

However, Zheng *et al.* (2004) found the effect of crystallinity on the mechanical properties of graphite/HDPE composites to be insignificant. They found that expanded graphite and untreated graphite nucleated HDPE, thereby inducing crystallisation at high temperatures. However, the degree of crystallinity decreased with filler content and it was inferred that the improvement in mechanical properties was not a result of crystallinity, but rather the reinforcing effect of graphite.

2.7.5 Mechanical properties of rotationally moulded composites

Agglomeration and segregation of particulate fillers is a potential problem in rotomoulding (Yuan *et al.*, 2008; Yan *et al.*, 2006; Martin *et al.*, 2003; Wesley, 1999). In the various works encountered, research efforts were devoted to addressing factors which promote even distribution of the fillers to avert these challenges as they are known to impact on the mechanical properties.

Effect of mixing methods on composite mechanical properties

With regard to the mixing method used, the filler type and size have been shown to influence the mechanical properties of rotomoulded composites. Yan *et al.* (2006) obtained an improvement in the tensile modulus of polyethylene composites with various particles between 90-240 μm up to a loading of 10 vol.% when the dry mixing method was used. This was in contrast to the tensile moduli of composites moulded from smaller sized particles (6.5-

35 μm), which increased up to a loading of at most 2%. However, melt compounding was shown to be suitable for the smaller particles (6.5–35 μm).

In the study by Yan *et al.* (2006), it was established that the reinforcing effect was only possible if a uniform distribution of the filler was achieved. This was achieved by the dry mixing method for particles between 90–240 μm and by the melt compounding method for particles between 6.5–35 μm .

In the work by Wesley (1999) on rotational moulding of glass fibre reinforced polyethylene composites, dry mixing was used. Fibre/matrix segregation resulted in the fibres lining the inside of the moulding, and playing no part in enhancing the mechanical properties. However, Yuan *et al.* (2008) achieved a slight improvement (2 MPa) in tensile strength at 5 vol.% of wollastonite microfibrils in LMDPE using melt compounding. A coupling agent was used in this case.

Sae-Chieng & Kanokboriboon (2007) rotomoulded polyethylene filled with fly ash (160 μm) using the dry mixing and melt mixing methods. Deterioration in the tensile strength was observed in both instances. However, the deterioration was more pronounced for the dry-mixed samples. An improvement of 20% in the flexural modulus was observed for the melt-compounded samples, whereas the dry-blended samples were inconsistent. The deterioration in elongation-at-break was more severe in the dry blended compositions. This study shows that the melt compounding method is also suitable for larger particles (> 100 μm).

Wesley (1999) used the multiple shot method in a rotomoulding study on glass fibre reinforced polyethylene. An improvement in the tensile strength by 10% after 5 shots and the flexural modulus by 15% after 3 shots was observed.

Recently, Liu & Peng (2010) observed an improvement in the impact strength with an increase in polycarbonate reinforcement content in rotomoulded polycarbonate reinforced polyethylene composites. However, the tensile strength of the composites was found to deteriorate with increasing content of polycarbonate.

In agreement with other studies on rotational moulding, Liu & Peng (2010) found that the best mechanical properties of the composites prevailed when a certain peak internal air temperature (PIAT) was reached. The rate of cooling also had an effect on the mechanical properties.

Effect of coupling agents

Coupling agents are used to improve the adhesion between filler and polymer matrix. The use of coupling agents in composites for rotomoulding has been shown to improve the mechanical properties of the composites. Wesley (1999) found that using a maleic anhydride coupling agent optimises the mechanical properties when the melt compounding method is used. Maleic anhydride modified polyethylene was used to enhance the adhesion between talc and polyethylene, and between mica and polyethylene. This was evidenced by better mechanical properties (Robert & Crawford, 1999). Yuan *et al.* (2008) also found that the use of aminosilane as a surface treatment improved the strength of the wollastonite-filled PE.

Effect of the type, size and shape of filler

The study by Yan *et al.* (2006) using a range of different types of microsized fillers showed that for all the types of particulates sized between 90–240 μm , there was no variation in the tensile modulus and strength of the composites when the dry mixing method was used, regardless of type or shape of the filler. A trend in the modulus was apparent: an increase was observed up to about 10 wt.% filler content, after which there was a decrease. The tensile strength deteriorated with filler content.

All the types of smaller particles (6.5–35 μm) also followed the same trends when dry mixing was used. However, the improvement in the modulus was only up to about 2 wt.%. Deterioration in tensile strength was more severe. It was shown that smaller-sized particulates are not suitable for dry mixing.

Robert & Crawford (1999) also observed the same trends in the tensile moduli and strengths of rotomoulded polyethylene composites. They used mica and talc fillers in polyethylene-filled composites. There was an improvement in the modulus to up to 15 wt.%

filler loading, after which it deteriorated. A decrease in the strength was observed. However, the properties of the mica-filled composites were better than those of the talc-filled composites. This was explained in terms of the aspect ratios. The mica had a higher aspect ratio than talc. The results obtained by Robert & Crawford (1999) are in contrast to the results of Yan *et al.* (2006), because Yan *et al.* (2006) did not observe any differences in the mechanical properties of the composites due to different shapes or type of filler. This can be explained by the fact that the fillers used by Yan *et al.* had aspect ratios between 1–1.35.

Torres & Aragon (2006) synthesised natural fibre reinforced polyethylene composites through rotomoulding. The tensile strength results were dependent on the type of natural fibre used, but there was an optimum fibre content at which an improvement in tensile strength was observed. However, the impact strength decreased with an increase in fibre content.

2.7.6 Prediction of mechanical properties

Prediction of the modulus of composites with non-spherical fillers

Several models for predicting the moduli of polymer composites have been proposed in the literature. Ahmed & Jones (1990) carried out an extensive survey of models used to predict the moduli of particulate-filled composites. In this brief review, the emphasis is on mathematical models applicable to composites containing fillers with a platelet or flaky geometry such as graphite.

Guth model

Einstein's equation for the viscosity of a suspension of rigid spherical particles in a compliant matrix served as the basis for one of the earliest theories of composite modulus (Ahmed & Jones 1990). The equation can be written as:

$$\eta_c = \eta_p (1 + k_E v_f) \quad (2-5)$$

where η_c and η_p are the suspension and matrix viscosity respectively. k_E is the Einstein coefficient for spheres, which is equal to 2.5. v_f is the volume fraction of the particles. Analogously, the modulus of a composite can be obtained from (Brown & Ellyin, 2005):

$$E_c = E_p (1 + k_E v_f) \quad (2-6)$$

where E_c and E_p are the tensile or elastic modulus of the composite and matrix respectively.

Guth modified Einstein's equation for non-spherical fillers as follows (Ahmed & Jones, 1990):

$$E_c = E_p [1 + 0.67\alpha v_f + 1.62(\alpha v_f)^2] \quad (2-7)$$

where α is the filler aspect ratio, which is the length l to thickness t ratio.

The Guth equation and the preceding equations are valid at low filler concentrations (Ahmed & Jones, 1990).

Brodnyan model

Einstein's equation was further modified by Mooney for spherical fillers at higher concentrations (Kumar *et al.*, 2011). Rao (2007) generalised Mooney's equation for the modulus of a composite as follows:

$$\ln \frac{E_c}{E_p} = \frac{k_E v_f}{1 - v_f / v_m} \quad (2-8)$$

where v_m is the maximum packing efficiency of the filler. This is the ratio of the true volume of the filler to the apparent volume occupied by the filler.

Brodnyan modified the Mooney equation for non-spherical particles to incorporate the aspect ratio of the filler α ($1 < \alpha < 15$) (Brown & Ellyin, 2005):

$$\frac{E_c}{E_p} = \exp\left(\frac{2.5v_f + 0.407(\alpha - 1)^{1.508} v_f}{1 - v_f / v_m}\right) \quad (2-9)$$

The parallel and series model and its modifications

In the parallel and series model a lamellar composite with alternating layers of a high modulus phase and a compliant matrix phase is idealised. It is assumed that there is excellent

adhesion between the composite layers and thus the volume fraction, not the thickness of the composite layers, is the significant factor (Ward & Sweeney, 2004).

The effective modulus is a maximum when a uniaxial stress is applied parallel with the layers, yielding the Voigt average modulus (Ward & Sweeney, 2004). It is assumed that isostrain conditions are met in the composite layers. Equation 2–10 gives an expression for the modulus using the parallel model, which is the rule of mixtures (Kumar *et al.*, 2011).

$$E_c = E_f v_f + E_p v_p \quad (2-10)$$

When the uniaxial stress is applied transverse to the composite layers, a much lower modulus, which is the Reuss average modulus, is obtained (Ward & Sweeney, 2004). In this case the layers are subjected to the same force, hence the same stress, and thus isostress conditions are met. Equation 2–11 gives an expression for the modulus using the series model, which is the inverse rule of mixtures (Kumar *et al.*, 2011):

$$\frac{1}{E_c} = \frac{v_f}{E_f} + \frac{v_p}{E_p} \quad (2-11)$$

The parallel and series models give the upper and lower bounds respectively for the elastic modulus (Ahmed & Jones, 1990). Other modifications of the parallel and series models exist that give the modulus within the upper and lower bounds of the parallel and series models, for instance the Hashin and Shtrikman model, the Hirsch model and the Takayanagi model (Ahmed & Jones, 1990).

Halpin-Tsai Model

The Halpin-Tsai equations (Halpin & Kardos, 1976) are widely used to predict the modulus of unidirectional composites (Tucker III & Liang, 1999; Fornes & Paul, 2003). The Halpin and Tsai equations are a general form of the Kerner equation and many other equations (Nielsen & Landel, 1994). The equations have the form of:

$$\frac{E_c}{E_p} = \frac{(1 + \xi \eta v_f)}{(1 - \eta v_f)} \quad (2-12)$$

where E_c is the composite tensile modulus in the longitudinal or transverse direction with respect to the alignment of particles, ζ is a shape factor that depends on the geometry of the filler particles and their relative orientation with respect to the load direction. The parameter η is given by:

$$\eta = \frac{(E_f / E_p - 1)}{(E_f / E_p + \zeta)} \quad (2-13)$$

where E_f is the tensile modulus of the filler. Van Es (2001) has corrected the shape factors for platelet reinforcements for the longitudinal (E_{CL}) and transverse (E_{CT}) composite modulus as $\zeta_L = \frac{2}{3} \frac{w}{t}$ and $\zeta_T = 2$ respectively. Van Es (2001) also approximated the composite modulus of a matrix containing randomly oriented platelets using an averaging scheme as follows:

$$E_c = 0.49E_{CL} + 0.51E_{CT} \quad (2-14)$$

where E_c is the composite modulus, and E_{CL} and E_{CT} are evaluated from the Halpin-Tsai equations using the respective shape factors ζ_L and ζ_T .

Lewis-Nielsen model

Lewis and Nielsen (Nielsen & Landel, 1994; Halpin & Kardos, 1976) modified the Halpin-Tsai equations by considering the maximum volumetric fraction of the filler to yield the following equation:

$$\frac{E_c}{E_p} = \frac{(1 + \xi\eta v_f)}{(1 - \psi\eta v_f)} \quad (2-15)$$

where

$$\psi = 1 - v_f \frac{(1 - v_m)}{v_m^2} \quad (2-16)$$

Smaller maximum volumetric packing fractions v_m of the filler result in a rapid increase of the modulus in the Lewis-Nielsen model (Wu *et al.*, 2004). However, with v_m set at 1, the Halpin-Tsai and Lewis-Nielsen models are similar.

Verbeek & Focke Model

The Verbeek & Focke model predicts the modulus of an idealised composite reinforced with rectangular platelets aligned parallel to the direction of stress application (Verbeek, 2001). Stress transfer from the matrix to the filler is explained in terms of a shear mechanism, and perfect adhesion is assumed between components (Kumar *et al.*, 2011). Verbeek & Focke took into consideration the effect of composite porosity on the modulus as they noted that porosity influences the area over which the stress acts. In the model the modulus is zero when the polymer content is zero. This phenomenon is not addressed in other models, which predict that when the polymer content is zero the modulus will be that of the filler. In this model the Young's modulus is given as:

$$E_c = v_f E_f MRF + v_p E_p \quad (2-17)$$

where MRF is the modulus reduction factor, which depends on the filler aspect ratio and is given by:

$$MRF = 1 - \frac{\tanh(\phi)}{\phi}, \quad (2-18)$$

$$\phi = \alpha \sqrt{\frac{(1-\chi)^3 G_p v_f}{E_p (1-v_f)}}, \quad (2-19)$$

χ is the modified voidage (voidage relative to the polymer phase), given by:

$$\chi = \frac{\phi}{v_p (1-\phi) + \phi} \quad (2-20)$$

and ϕ is the composite porosity/void content given by:

$$\phi = \frac{(1-v_p)^2 v_m}{1-v_f v_m} \quad (2-21)$$

G_p is the polymer matrix shear modulus.

2.8. Thermal conductivity of polymer composites

2.8.1 Thermal conductivity

Thermal conductivity is a measure of the ability of a material to conduct heat. Thermal conductivity is a transport property, that is, a coefficient that defines the ratio between a flux and the directional gradient of the driving force causing the transport (Bigg, 1995). In heat transfer, the flux is the heat flux, q ; dT/dx is the directional temperature gradient through distance x which is the driving force. The heat flux, q , is the rate of heat flow through a certain cross-sectional area A . Following Fourier's law of heat conduction, thermal conductivity (λ) is defined according to the equation:

$$\lambda = \frac{q}{A} \bigg/ \frac{dT}{dx} \quad (2-22)$$

Weber *et al.* (2003a) asserted that the key factors affecting polymer composite thermal conductivity are:

- Thermal conductivities of the filler and the polymer matrix.
- The filler characteristics, i.e. shape and size, therefore aspect ratio.
- The filler loading.
- The degree of dispersion of the filler in the polymer matrix.
- Orientation of the filler.
- Interfacial interaction between the filler and the matrix.

2.8.2 Factors that influence thermal conductivity of polymer composites

Effect of filler and matrix conductivities

Highly thermally conductive composites are produced with fillers with high inherent conductivity. However, Bigg (1995) has shown that once the ratio of filler conductivity to matrix conductivity is over 100, there will not be a significant difference in the conductivities of composites.

The polymer matrix crystallinity plays a significant role in composite thermal conductivity. In semi-crystalline polymers, better heat conduction is attained in the crystalline phase compared to the amorphous phase. For the same type of graphite, HDPE composites had a higher conductivity compared to LLDPE composites as a result of HDPE being more crystalline (Krupa *et al.*, 2004).

Effect of filler loading

In the several works reviewed, for instance Wang *et al.* (2001), Weber *et al.* (2003b), Hung *et al.* (2006), Ye *et al.* (2006) and Debalak & Lafdi (2007), the increase in thermal conductivity of polymer composites with filler loading is unambiguous. This is not unexpected since the thermal conductivities of fillers are usually decades higher than those of polymers.

Effect of particle size

The effect of particle size appears to be significant in anisotropic fillers. For instance, the results of Bigg (1995) showed that for composites with spherical metal spheres, the conductivity does not depend on the particle size or metal type. However, Debalak & Lafdi (2007) observed higher thermal conductivities with larger graphite flakes, compared to conductivities exhibited in the composites with smaller graphite flakes in exfoliated graphite/epoxy composite. Improvements were observed of about 300% (0.868 W/m.K) at a graphite loading of 4 wt.% with the larger flakes (150 mesh) compared to the medium and smaller size flakes (100 and 50 mesh). This was attributed to the higher aspect ratios in the larger exfoliated graphite flakes compared to the smaller ones. Ye *et al.* (2006) also observed an increase in thermal conductivity with graphite particle size increase. The micron-sized particles used had a range of 1.5–30 μm . The increase in conductivity with graphite particle size reached a maximum before the whole particle size range was covered. This observation appears to be in agreement with what Bigg (1995) showed. However, Ye *et al.*'s explanation was that finer particles offer more thermal resistance due to increased contact with the matrix.

In contrast, Krupa & Chodák (2001) observed higher conductivities in HDPE/graphite and PS/graphite composites prepared with smaller graphite particles (d_{50} of 14.1 μm) compared to composite of the same matrices prepared with bigger graphite particles (d_{50} of

31.6 μm). This difference was attributed to agglomeration of the smaller particles resulting in the formation of more conductive pathways.

Effect of filler shape

The filler particle shape determines the filler aspect ratio, as has been previously discussed. It has been established that high aspect ratio fillers impart higher conductivity to polymer composites at low filler loading. High aspect ratio fillers can easily form conductive pathways within the polymer matrix compared to isotropic fillers (Agari *et al.*, 1993). The results of Weber *et al.* (2003b) showed that the conductivity was higher for composites with fibres compared to composites containing graphite particles, as a result of the different aspect ratios. Other results attest this trend (Tecke *et al.*, 2007).

Effect of filler orientation

The orientation of anisotropic fillers in the polymer matrix has been shown to have a significant effect on the thermal conductivity of the composite. Weber *et al.* (2003b) demonstrated that the thermal conductivity was high in the direction of filler alignment, compared to the transverse direction, for composites of polycarbonate with graphite and carbon fibres respectively. Analogously, Fu & Mai's (2003) study showed that high conductivity was obtained from minimum mean fibre orientation angle, with respect to the direction of thermal conductivity measurement. For platelet fillers such as graphite, which exhibits anisotropic conductivity, maximum conductivity can be obtained when the basal plane is aligned parallel to the direction of heat flow (Hill & Supancic, 2002).

Effect of filler dispersion

Agari *et al.* (1991) studied the effect of different dispersion states of graphite-filled, low molecular weight polyethylene. Their study showed that the thermal conductivity decreased in the order of powder mixing, solution mixing, roll milling and melt mixing. These results showed that the conductivity was higher in dispersion states in which the graphite could easily form conductive chains.

Effect of interfacial interactions and porosity

Several researchers have shown that improved interfacial interactions between the filler and polymer matrix significantly enhance the thermal conductivity of polymer composites (Zhang & Dai, 2007; Dong, 2005; Hung *et al.*, 2006). The interface conductance between the filler and matrix is significant in composite conductivity when smaller particles are involved due to their large interfacial areas (Dong, 2005; Hung *et al.*, 2006). Poor bonding between the matrix and filler and thermal expansion mismatch in the composite can increase the interfacial thermal contact resistance (Dong, 2005).

In nonmetals, heat transfer is a result of the flow of lattice vibration energy, or phonons, along the temperature gradient within the specimen. Phonons are sensitive to surface defects, thus interfacial contact between filler and polymer is critical (Dong, 2005). Defects contribute to interfacial thermal resistance as a result of phonon scattering (Sumirat *et al.*, 2006).

Pores are also a cause of phonon scattering, contributing to the thermal resistance and hence reducing the thermal conductivity (Sumirat *et al.*, 2006). The results of Osman *et al.* (2007) attest this assertion.

2.8.3 Prediction of composite thermal conductivity

Numerous mathematical models have been proposed for the prediction of thermal conductivity of two-phase composites. Exhaustive reviews have been carried out by Progelhof *et al.* (1976) and Bigg (1995).

The parallel, series and geometric models

The basic thermal conductivity models for two-phase systems are the parallel, series and geometric mean conduction models (Progelhof *et al.*, 1976). The parallel and series models are adaptations of the rule of mixtures and inverse rule of mixtures respectively.

The parallel model predicts the conductivity of a composite consisting of alternating parallel layers of filler and polymer matrix, with heat flux parallel to the layers. For a polymer matrix with a single type of filler, the parallel model gives the composite conductivity as:

$$\lambda_c = v_f \lambda_f + v_p \lambda_p \quad (2-23)$$

where λ_c is the composite thermal conductivity, λ_f and λ_p are the thermal conductivities of the filler and matrix respectively, v_f and v_p are the volume fractions of the filler and polymer matrix.

The parallel model predicts the thermal conductivity of unidirectional composites with continuous fibres well, but it usually over-predicts the thermal conductivity of short fibre and particulate composites (Weber *et al.*, 2003a). It gives the upper bound of the thermal conductivity (Bigg, 1995).

The series model predicts the conductivity of a composite consisting of alternating parallel layers of filler and polymer matrix, with heat flux normal to the layers. For a polymer matrix with a single type of filler, the series model gives the composite conductivity as:

$$\frac{1}{\lambda_c} = \frac{v_f}{\lambda_f} + \frac{v_p}{\lambda_p} \quad (2-24)$$

The series model usually under-predicts the thermal conductivity of composites and gives the lower bound of thermal conductivity.

For a polymer matrix with a single type of filler, the geometric rule of mixtures is given as (Progelhof *et al.*, 1976):

$$\lambda_c = \lambda_f^{v_f} \lambda_p^{v_p} \quad (2-25)$$

Weber *et al.* (2003a) asserted that the geometric mean model fits experimental data better than the series and parallel models. Furthermore, the results of Ye *et al.* (2006) show that of all the conductivity models tested, the geometric model fitted the thermal conductivity data of graphite/polyethylene composites well, compared to other models.

Maxwell model

Maxwell used potential theory to obtain a conductivity model for randomly distributed and non-interacting homogenous spheres in a homogeneous continuous medium (Progelhof *et al.*, 1976). The assumption that the fillers should be non-interacting limits this model to low filler concentrations. Higher filler concentrations mean that filler interaction occurs, resulting in the formation of conductive pathways. As a result it under-predicts the conductivity of composites:

$$\lambda_c = \lambda_p \left[\frac{2\lambda_p + \lambda_f + 2v_f(\lambda_f - \lambda_p)}{2\lambda_p + \lambda_f - 2v_f(\lambda_f - \lambda_p)} \right] \quad (2-26)$$

Lewis-Nielsen model

The Lewis-Nielsen (LN) model for the prediction of the thermal conductivity of composites is derived by analogy from the Halpin-Tsai equations (Nielsen, 1974). The Halpin-Tsai equations (Halpin & Kardos, 1976) are widely used to predict the tensile modulus of composites (Tucker III & Liang, 1999; Fornes & Paul, 2003). Lewis and Nielsen (Nielsen, 1974) considered the maximum volumetric fraction of the filler to yield the following equations for the composite thermal conductivity:

$$\frac{\lambda}{\lambda_p} = \frac{1 + ABv_f}{1 - B\psi v_f} \quad (2-27)$$

$$A = k_E - 1 \quad (2-28)$$

where λ is the composite thermal conductivity, A is a shape factor that depends on the geometry of the filler particles and their relative orientation with respect to the heat flow; it is related to the Einstein coefficient k_E . The parameter B takes into consideration the relative thermal conductivity of the components and is given by:

$$B = \frac{\lambda_f / \lambda_p - 1}{\lambda_f / \lambda_p + A} \quad (2-29)$$

The factor ψ is determined by the maximum packing fraction v_m as follows:

$$\psi = 1 + \left(\frac{1 - v_m}{v_m^2} \right) v_f \quad (2-30)$$

The maximum packing fraction v_m is the true volume of the filler particles divided by the volume they appear to occupy when packed to their maximum extent. When the maximum packing fraction v_m is set at 1, the Lewis-Nielsen model becomes the Halpin-Tsai model. Lower maximum volumetric packing fractions v_m of the filler result in a rapid increase of the composite thermal conductivity in the Lewis-Nielsen model (Bigg, 1995).

Cheng and Vachon model

Cheng & Vachon (1969) assumed that the discontinuous phase (the filler particles) had a parabolic distribution in the continuous phase (polymer matrix), thereby evaluating the constants in Tsao's basic probabilistic model. The constants are expressed as a function of the constituent proportions. An expression for the equivalent thermal resistance of a unit cube of the two-phase mixture, which is in terms of the constants of the parabola and thermal conductivity of the constituents, was then derived. For the case where $\lambda_f > \lambda_p$, the composite conductivity is given by:

$$\frac{1}{\lambda_c} = \frac{1}{\sqrt{C(\lambda_f - \lambda_p)[\lambda_p + B(\lambda_f - \lambda_p)]}} \ln \frac{\sqrt{\lambda_p + B(\lambda_f - \lambda_p)} + \frac{B}{2} \sqrt{C(\lambda_f - \lambda_p)}}{\sqrt{\lambda_p + B(\lambda_f - \lambda_p)} - \frac{B}{2} \sqrt{C(\lambda_f - \lambda_p)}} + \frac{1 - B}{\lambda_p} \quad (2-31)$$

$$\text{where, } B = \sqrt{\frac{3v_f}{2}} \text{ and} \quad (2-32)$$

$$C = -4 \sqrt{\frac{2}{3v_f}} \quad (2-33)$$

If the thermal conductivity of the filler is much higher than that of the polymer, i.e. $\lambda_f \gg \lambda_p$ or $\lambda_f / \lambda_p > 100$, the second term can approximate the thermal conductivity of the composite, as long as $v_f < 0.667$. Thus:

$$\lambda_c \approx \frac{\lambda_p}{1-B} \quad (2-34)$$

Agari model

The model of Agari and Uno is based on the parallel and series models of conduction (Agari & Uno, 1986). Their model considers a randomly dispersed system to be isotropic in thermal conduction. This model is given as:

$$\log \lambda_c = v_f C_2 \log \lambda_f + v_p \log(C_1 \lambda_p) \quad (2-35)$$

where $0 < C_2 < 1$ is a constant which describes the ease of forming conductive chains of filler particles. For those filler particles which easily form conductive chains, C_2 is close to 1. C_1 is a constant which describes the effect of the filler on crystallinity and crystal size of the polymer.

The Agari model was shown to predict the conductivities of graphite-filled polymers well (Agari & Uno, 1986). Its drawback, however, is the difficulty of evaluating the constants C_1 and C_2 .

Hatta model

Hatta *et al.*'s model (1992) is based on the Eshelby equivalent inclusion model for the modulus. In this model equivalent inclusions with a thermal conductivity similar to that of the surrounding polymer matrix and Eigen value-temperature gradient replace the actual fillers in the composite. For composite with flakes aligned in-plane, the Hatta model is:

$$\frac{\lambda_{ci}}{\lambda_p} = 1 + \frac{v_f}{S_i(1-v_f) + \frac{\lambda_p}{(\lambda_f - \lambda_p)}} \quad (2-36)$$

where i shows the direction of thermal conduction, with $i = z$ denoting the out-of-plane direction and $i = xy$ the in-plane direction and:

$$S_z = 1 - \frac{\pi}{2} \beta \quad (2-37)$$

$$S_{.xy} = \frac{\pi}{4} \beta \quad (2-38)$$

where β is the diameter-to-thickness ratio of the flake, assumed to be a disc.

The Hatta model was shown to predict the composite thermal conductivity of keramid with Al_2O_3 short fibres, SiN_4 whiskers and SiO_2 , but under-predicted the thermal conductivity for BN flakes/keramid composites. The authors attributed this to a material change in the BN flake composite. However, as noted by Bigg (1995), the flakes are seldom in perfect alignment, and random orientation of flakes could result in the formation of conductive pathways due to clusters of flakes which have not been accounted for in the model.

CHAPTER 3 : EXPERIMENTAL

3.1 Materials

Linear low-density polyethylene (LLDPE) was supplied by Sasol Polymers. It was a hexene co-monomer-based rotomoulding powder (Grade HR 411; MFI 3.5 (190 °C/2.16 kg); density 0.939 g/cm³; particle size 90% < 600 µm). Natural Zimbabwean flake graphite was obtained from BEP Bestobell, Johannesburg. Chemserve Systems supplied the release agent Sliprelease 20K, and Orchem provided the antioxidant Orox PK (polymerised 2,2,4-trimethyl-1,2-dihydroquinoline). Two grades of expandable graphite ES 250 B5 (onset temperature 220 °C) and ES 170 300A (onset temperature 300 °C) were supplied by Qingdao Kropfmuehl Graphite (China). The latter constituted the expandable form used in this study. The former could not be used for rotomoulding as the expansion onset temperature was too low. Instead it was used to prepare the pre-expanded graphite form. This was done by exposing ES 250 B5 grade powder to high heat for 5 minutes by placing it in a Thermopower electric furnace set at 600 °C.

3.1.1 Material characterisation

The graphite particle size distributions were determined with a Mastersizer Hydrosizer 2000 (Malvern Instruments, Malvern, UK). The specific surface areas of the graphite powders were determined with a Nova 1000e BET in N₂ at 77 K. True densities were determined on a Micrometrics AccuPyc II 1340 helium gas pycnometer. Tap densities were determined according to the method of Focke *et al.* (2009). Minute quantities of graphite powder were added to a 25 cm³ measuring cylinder. The cylinder was tapped exhaustively against a wooden surface at an angle of ca. 25 ° from the vertical to consolidate the column of powder after each addition. The mass of powder corresponding to a tapped volume of 25 cm³ was determined.

LLDPE powder and graphite morphologies were studied using a JEOL JSM-5800LV scanning electron microscope (SEM) (for low-resolution micrographs) and a Zeiss ULTRA FE-SEM (for high-resolution micrographs). The acceleration voltages used in these

instruments were 20 kV and 1 kV respectively. No electro-conductive coating was applied on the graphite particles.

The elemental composition of the graphite powders was determined by XRF analysis performed using the ARL 9400XP+ XRF spectrometer. The samples were prepared as pressed powder briquettes and introduced to the ARL 9400XP+ XRF spectrometer. Analyses were performed using the UniQuant software. The software analyses for all elements in the periodic table between sodium (Na) and uranium (U), but only elements found above the detection limits, were reported. The values were normalised, as no LOI was done to determine crystal water and oxidation state changes. All elements were expressed as oxides.

3.2 Methods

Rotational moulding was the processing method of interest in this work. However, injection-moulded composites of the same formulations as the rotomoulded formulations were also prepared for comparison. The composites were rotomoulded using the three forms of graphite: natural Zimbabwean graphite, expandable and expanded graphite. Three mixing schemes were investigated: dry blending, melt compounding and double dumping. Table 3-1 summarises the experimental processing methods utilised.

Table 3-1 Description of rotomoulding and injection moulding experiments

Rotational moulding		Graphite content (wt.%)							
Graphite type	Mixing method	0	2	5	8	10	15	20	25
Zimbabwean graphite	Dry blending	▪		▪		▪	▪	▪	▪
	Double dumping	▪		▪		▪	▪	▪	
	Melt compounding	▪		▪		▪	▪	▪	▪
Expandable graphite ES 170 300 A	Dry blending	▪		▪		▪	▪	▪	
	Double dumping	▪		▪		▪	▪	▪	
	Melt compounding	▪		▪		▪	▪	▪	
Expanded graphite ES 250 B5	Dry blending	▪		▪		▪	▪	▪	
	Melt compounding	▪	▪	▪	▪	▪			
Injection moulding		Graphite content (wt.%)							
Graphite type		0	2	5	8	10	15	20	25
Zimbabwean graphite		▪		▪		▪	▪	▪	▪
Expandable graphite ES 170 300A		▪		▪		▪	▪	▪	
Expanded graphite ES 250 B5		▪	▪	▪	▪	▪			

3.2.1 Rotational moulding

A stainless steel rectangular cuboid mould with inside dimensions 200 mm x 150 mm x 100 mm was used for rotomoulding. A constant volume of material (ca. 320 cm³) was used for all compositions in order to obtain a constant part thickness. The charge mass was adjusted according to the density of the various components. Detailed calculations and the actual charge weights used for all weight fractions are given in Appendix A.

The rotomoulding machine was a modified Thermopower convection oven that was fitted with a biaxial mould rotating mechanism.

Dry-blended composites

Composites containing 5, 10, 15 and 20 wt.% Zimbabwean graphite, ES 170 300A and expanded ES 250 B5 were prepared. The dry-blended samples were prepared by blending the LLDPE, graphite and heat stabiliser Orox PK for one minute using a coffee blender. The rotomoulding processing conditions are stated in Table 3-2. The mould was cooled in the oven using ambient air.

Compounded composites

LLDPE composites with 5, 10, 15, 20 wt.% graphite were prepared with Zimbabwean graphite and ES 170 300A, with an additional 25 wt.% graphite composition for the Zimbabwean graphite. LLDPE/pre-expanded graphite ES 250 B5 samples contained 2, 5, 8 or 10 wt.% filler. LLDPE composites with the Zimbabwean graphite and ES 170 300A were manually mixed before compounding. The pre-expanded ES 250 B5 was mixed with LLDPE in a Jones vertical high speed mixer for two minutes before compounding.

All the samples were melt-compounded in a 40 mm co-rotating Berstorff twin screw extruder using the processing conditions given in Appendix B. The composite strands were water cooled, air dried and granulated into pellets. These were then milled into rotomoulding powder using a Pallmann 300 pulveriser. The heat stabiliser Orox PK was blended into the

powder using a coffee blender for a period of one minute. The rotomoulding conditions are reported in Table 3-2. The mould was allowed to cool down inside the oven using ambient air.

Double dumped composites

LLDPE/graphite compositions with 5, 10, 15 and 20 wt.% compositions were prepared with the Zimbabwean graphite and ES 170 300A. The LLDPE and heat stabiliser Orox PK were first blended in a coffee blender for one minute. The relevant amount of graphite for each composition was charged into the mould after application of the mould release and rotated at 30 rpm for 1 minute, after which LLDPE was then charged. The conditions in Table 3-2 were then used for rotomoulding. The mould was cooled in the oven using ambient air.

Table 3-2 Rotomoulding conditions

Oven temperature (°C)		Heating time (min)	Cooling time (min)	Rotation speed (rpm)
Set	Initial			
300	~90	60	30	30

3.2.2 Injection moulding

Injection-moulded test specimens were moulded on an Engel EC088 injection moulding machine using the compounded samples. ASTM drop impact and ASTM tensile test moulds were utilised. The injection moulding parameters are given in Appendix C.

3.2.3 Composite characterisation

Composite interior surface texture

The surface texture of the interior surfaces of the rotomoulded composites was characterised using a Nikon D700 digital camera with a Nikkor lens (105 mm macro, exposure f32 at 1/125 s). Studio flashes with umbrellas were used.

Graphite distribution in the composites and composite morphology

Polished cross-sections of the composites were prepared to study the distribution of the graphite fillers. Sectioned sample pieces were first cast in an epoxy resin (Specifix 20). After the resin had set, they were polished on a Buehler Alpha 2-speed grinder-polisher. These specimens were viewed with a Zeiss Imager fitted to an A1m optical microscope under the epi-polarised light mode.

The morphology of the composites was also observed with scanning electron microscopy (SEM). Samples were fractured in liquid nitrogen and coated with gold in an Emitech K550 X sputter coater. The fracture surfaces were viewed using an acceleration voltage of 5 kV in a JEOL JSM 5800LV.

Rheology of the composites

Viscosity determinations for compounded composite samples containing 10 wt.% graphite were done on an Anton Paar Physica MCR301 rheometer. Estimates of the zero-shear viscosity were obtained by operating the machine at a shear rate of 0.01 s^{-1} . A parallel plate measuring system (1 mm gap and 50 mm ϕ) fitted with a Peltier heating system (Anton Paar PTD200 attachment) was used. The tests were done at temperatures ranging from 140–200 °C.

Composite porosity

The envelop density of 15 x 15 mm² pieces of rotomoulded sheets was evaluated on a Micrometrics GeoPyc 1360 envelope density analyser. Five cycles were performed on each sample and each value was an average of three tests. The skeletal density of these test pieces was measured on a Micrometrics AccuPyc II 1340 helium gas pycnometer using five cycle measurements. Each value was an average of three tests. The porosity was calculated as follows:

$$Porosity (\%) = \left(1 - \frac{Envelop\ density}{Skeletal\ density} \right) \times 100 \quad (3-1)$$

Differential scanning calorimetry

Differential scanning calorimetry (DSC) thermograms of the LLDPE and graphite composites at 10 wt.% graphite loading were obtained using a Mettler Toledo DSC 1 STAR^e System Thermal Analyser in air at a flow of 50 mL/min at a heating rate of 10 °C/min. Closed aluminium pans with pin holes were used to hold the samples. The data analysed was for the second heating and cooling. Samples of ca. 6 mg were held isothermally at -50 °C for 5 minutes before heating to 200 °C. The samples were held at 200 °C for 5 min and then cooled back to -50 °C at a cooling rate of 10 °C/min.

Thermogravimetric analysis

Thermogravimetric analysis (TGA) of the LLDPE and graphite composites at 10 wt.% graphite loading was performed using a Mettler Toledo TGA 850e. Closed 150 µm alumina pans with lids (pin hole) were used to hold the samples. Sample masses of ca. 15 mg were heated from 25–1 000 °C at 10 °C min⁻¹ under air flow (50 mL/min).

Surface resistivity

Surface resistivity was determined according to IEC 61340-2-3 using a Vermason TB-7549 concentric ring probe and high-resistance test kit shown in Figure 3-1. The surface resistivity tests were performed on the exterior surfaces of 120 mm x 80 mm sheets cut out of the rotomoulded specimens. The surface resistivity of injection-moulded samples was determined using 60 mm ϕ circular discs moulded for ASTM drop impact tests. All tests were performed on as-moulded samples placed on an insulating wooden surface at ambient conditions. Surface resistivity values were calculated from surface resistance values using the formula:

$$\rho_s = \pi R_x (d_1 + g) / g \quad (3-2)$$

where ρ_s is the surface resistivity (Ω/\square); R_x is the measured surface resistance (Ω); d_1 is the diameter of the inner contact electrode (0.03 m); g is the distance (gap) between the contact electrodes (0.0165 m). Each reported value represents the geometric mean of five separate measurements done on different samples. The error bars reported span the full range of values measured for each sample set.



Figure 3-1 Concentric ring probe and high-resistance meter

Tensile properties

Tensile tests according to ASTM D 638-08 were performed at 23 °C on a Lloyds Instruments LRX Plus machine fitted with a 5 kN load cell using an extension rate of 50 mm/min. Dumbbells with a gauge length of 35.5 mm were punched out of sheets cut from the rotomoulded samples. Injection-moulded tensile strength specimens (gauge length 35 mm) were moulded directly. Five specimens were tested for each sample and the data averaged.

Impact properties

The falling weight (Gardner Impact) impact resistance test was used to determine the impact energy according to ASTM D 5420-04. Square discs (42 mm x 42 mm) were cut from the rotomoulded samples. The average thickness of the square discs was 2.88 ± 0.39 mm. Circular discs (diameter 60 mm, 3 mm thick) were injection moulded directly. The mass of

the drop weight used was 0.9 kg. For each sample, the expected break height was first determined, and then 20 specimens were used for the actual tests. The tests were carried out at room temperature. A sample calculation for the impact energy of 5 wt.% Zimbabwe graphite, compounded and rotomoulded, is shown in Appendix D.

Thermal conductivity

Thermal conductivity measurements were performed on 42 mm x 42 mm square sheets cut from the rotomoulded sheets using a ThermTest Inc. Hot Disk® TPS 500 Thermal Constants Analyser. The Hot Disk® TPS 500 Thermal Constants Analyser uses the transient plane source method. A 6.403 mm Kapton disk type sensor was selected for the analysis. The sensor was sandwiched between two sample sheets. A linear low-density polyethylene disc was inserted between the sample and the sample holder on both sides of the sample so as to reduce any heat loss. Injection-moulded specimens (60 mm diameter, 3 mm thick) were moulded using the drop impact strength mould with conditions in Appendix C, Table C-1. Each result was an average of three tests.

CHAPTER 4 : RESULTS AND DISCUSSION

4.1 Material characteristics

Figure 4-1 shows the particle size distribution of the various graphite types used. The d_{50} particle size, BET surface area and densities of the different graphites are presented in Table 4-1. The d_{50} particle size of the Zimbabwean flake graphite was about four times lower than that of the two expandable graphite grades. The surface area of the expandable graphite increased almost seven-fold when it expanded on heat treatment at 600 °C.

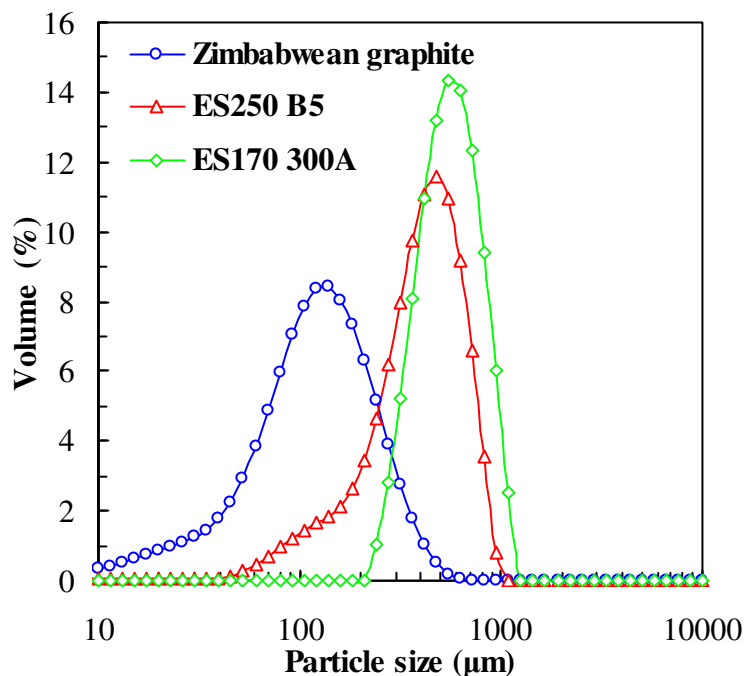


Figure 4-1 Graphite particle size distributions

Table 4-1 Physical properties of graphite

Graphite type	d_{50} (μm)	Surface area (m^2/g)	True density (g/cm^3)	Tap density (g/cm^3)
Zimbabwean graphite	112	4.0	2.34	0.80
Expandable ES 250 B5	381	2.4	2.08	0.85
Expanded ES 250 B5		16.3	0.66	
Expandable ES 170 300A	521	2.09	2.23	0.82

Figure 4-2 shows that the LLDPE had the recommended shape for rotomoulding: the “squared egg” shape (Crawford & Throne, 2002). Figure 4-2 also shows the flake-like nature of the natural and expandable graphites. The expanded graphite in Figure 4-2 has a worm-shaped, accordion-like structure. Slit-shaped gaps between the graphite platelets are clearly visible.

XRF results in Table 4-2 revealed that the carbon content of the Zimbabwean flake graphite was about 92 wt.%. The main impurities were silica and clay minerals. The carbon content of both the two expandable graphite samples was 90 wt.% and 88 wt.% for ES 250 B5 and ES 170 300A respectively.

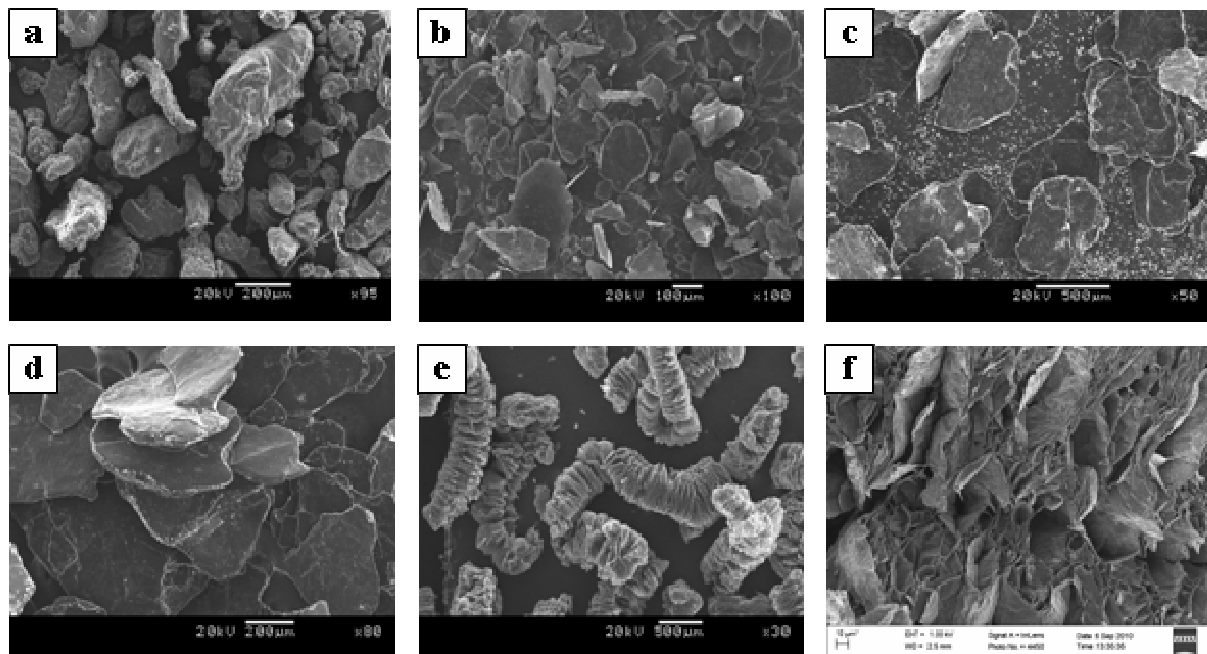


Figure 4-2 SEM micrographs of polyethylene and graphites: (a) LLDPE, (b) Zimbabwean graphite, (c) Expandable graphite ES 170 300A, (d) Expandable graphite ES 250 B5, (e) Expanded graphite ES 250 B5 (low resolution), and (f) Expanded graphite ES 250 B5 (high resolution)

Table 4-2 XRF analysis of graphites (wt.%)

	Zimbabwean graphite	ES 250 B5	ES 70300 A
SiO₂	3.19	1.20	1.06
TiO₂	0.04	0.03	0.02
Al₂O₃	1.55	0.49	0.63
Fe₂O₃	1.23	0.21	0.10
MnO	0.01	0.29	0.03
MgO	0.70	0.45	0.16
CaO	0.59	0.18	1.58
Na₂O	0.05	0.81	0.48
K₂O	0.20	0.18	0.07
P₂O₅	<0.01	<0.01	0.14
V₂O₅	0.01	<0.01	<0.01
SO₃	0.05	7.60	6.06
WO₃	0.01	0.01	<0.01
Cl	0.01	0.01	0.01
CuO	0.02	<0.01	<0.01
Co₃O₄	<0.01	0.08	<0.01
MoO₃	0.01	<0.01	<0.01
S	0.13	<0.01	<0.01
Rest Carbon	92.20	88.45	89.67

4.2 Composite aesthetics

The exterior surfaces of the rotomoulded composites were relatively smooth, with characteristic pinholes typically exhibited by rotomoulded products. However, the interior surfaces exhibited different textures. The dry-blended and double-dumped composites had relatively smooth interiors compared to the compounded composites, for all the graphite types at all graphite contents used. At 10 wt.% graphite, the compounded samples had rough interior surfaces (Figures 4-3 to 4-5). This observation was more pronounced for the expandable and expanded graphite. The roughness was observed to increase with graphite content.

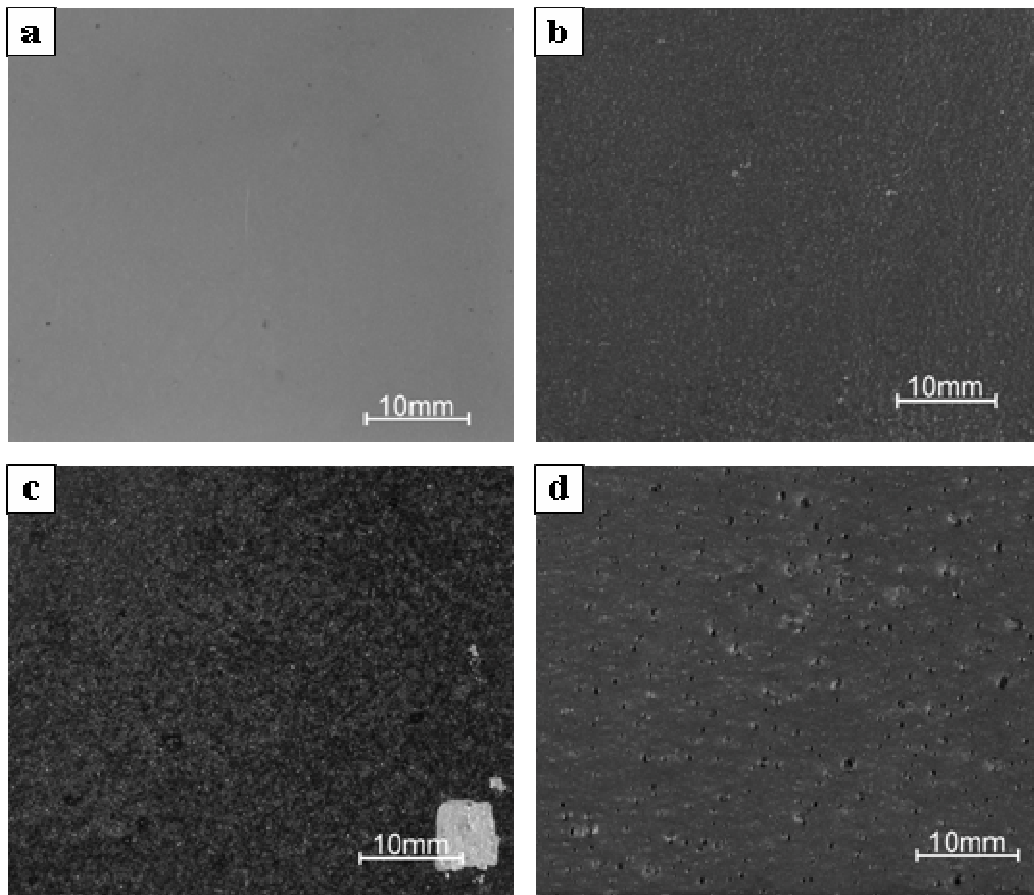


Figure 4-3 Digital photos of the interior surfaces of rotomoulded LLDPE/graphite composites: (a) Neat LLDPE, Zimbabwean graphite at 10 wt.% (b) dry-blended, (c) double-dumped and (d) pre-compounded

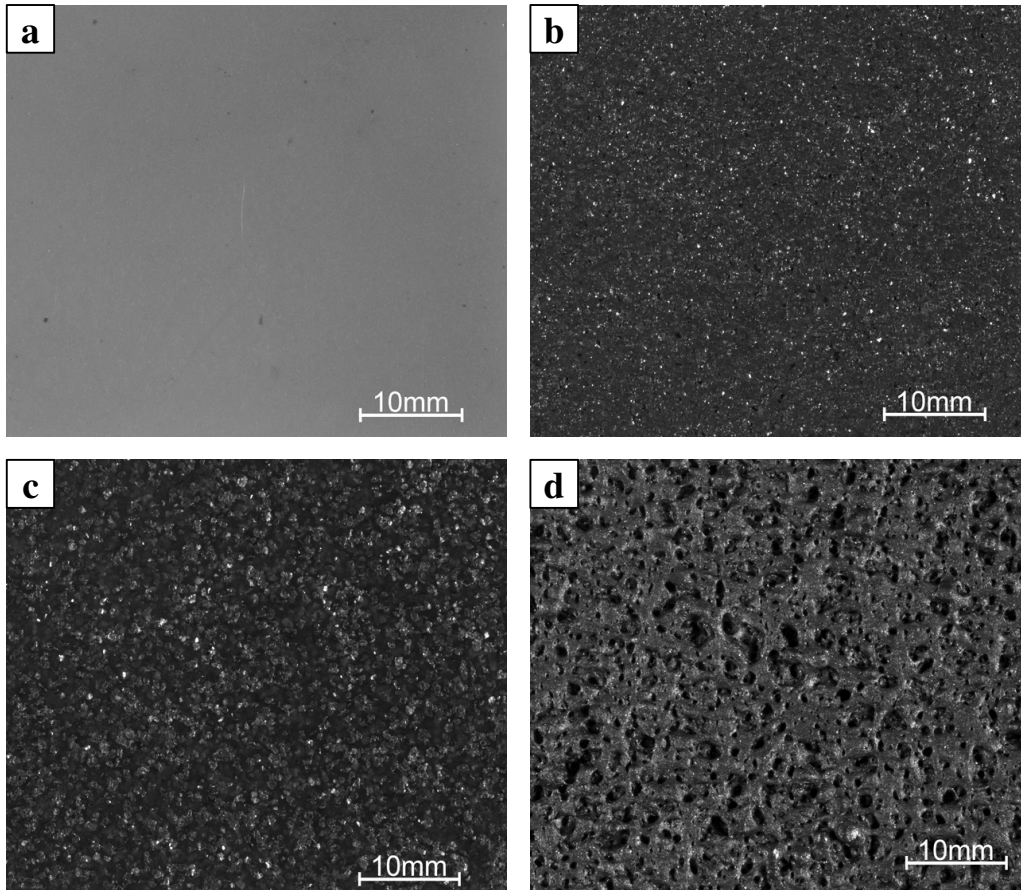


Figure 4-4 Digital photos of the interior surfaces of rotomoulded LLDPE/polyethylene composites: (a) Neat LLDPE, Expandable graphite at 10 wt.% (b) dry-blended, (c) double-dumped and (d) pre-compounded

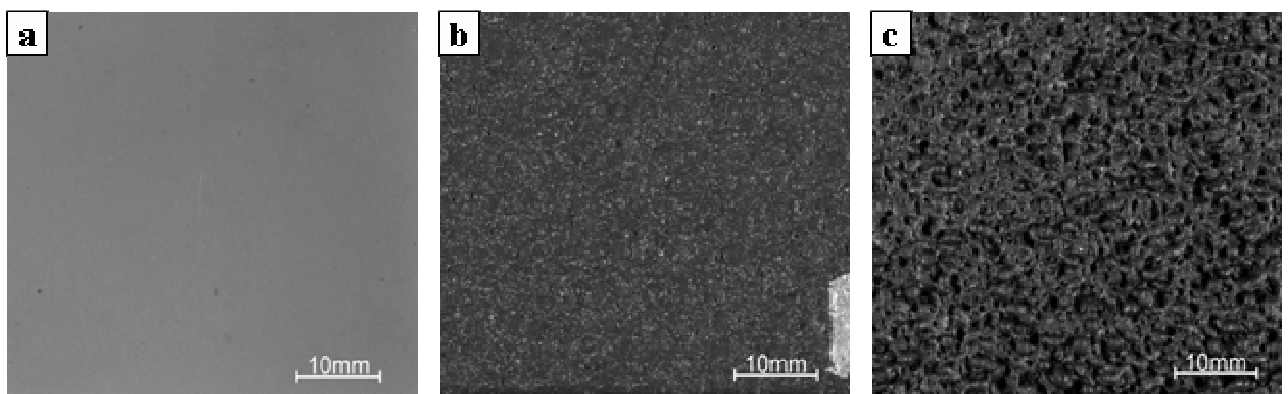


Figure 4-5 Digital photos of the interior surfaces of rotomoulded LLDPE/polyethylene composites: (a) Neat LLDPE, Pre-expanded graphite at 10 wt.% (b) dry-blended and (c) pre-compounded

4.3 Graphite dispersion and composite morphology

It seems that the filler particles were more homogeneously dispersed and distributed in the compounded composites compared to the dry-blended composites (Figure 4-6 and Figure 4-8). The graphite flakes in the dry-blended composites appear to feature randomly oriented and interconnected clusters. Dry blending did not have the same effect on expandable graphite (Figure 4-6).

In contrast, the compounded expandable graphite composites showed a more random orientation of the graphite flakes. The flake size appears to have been reduced significantly. A decrease in graphite flake size was also observed in the flake and expanded graphite composites (Figure 4-6). Figures E1 and F1 show that in the double-dumped composites, the graphite has a preferred orientation; the platelets are partially aligned along the wall.

All the types of graphite were well dispersed in the injection-moulded samples. (Figure 4-7). Another observation from Figure 4-7 was the tendency for the graphite platelets to be partially oriented in the direction of melt flow. Apparently some expanded graphite platelets were damaged or crumpled by the high-shear melt processing.

Cavities in wall cross-sections, graphite agglomerates and surface flaws (including pinholes) were observed for the rotomoulded samples (Figures 4-6, 4-8, E-1 and F-1). However, the injection-moulded composites were void free.

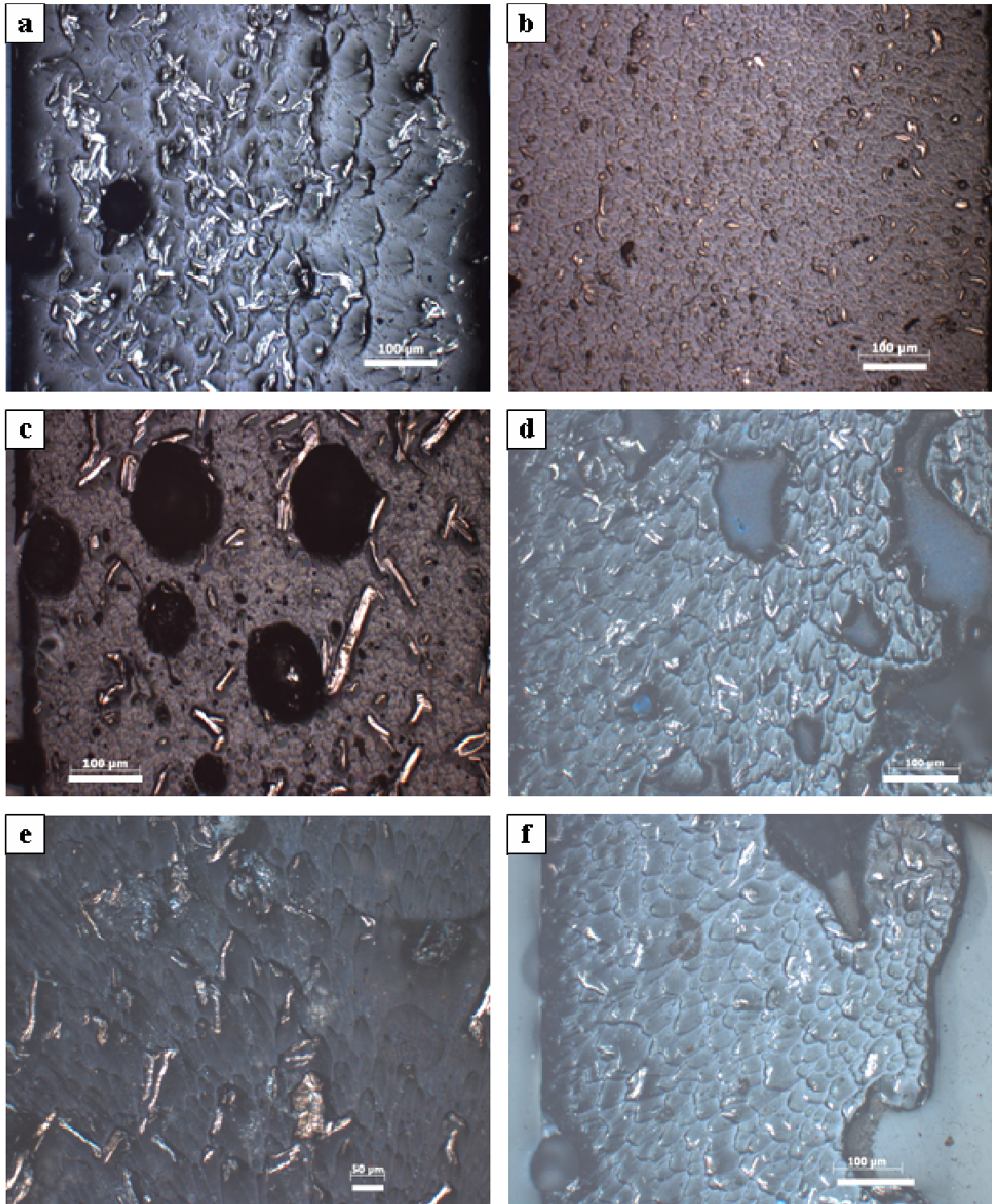


Figure 4-6 Photomicrographs of polished rotomoulded composite sections (5X magnification): Zimbabwean graphite at 15 wt.% (a) dry-blended, and (b) pre-compounded; expandable graphite at 15 wt.% (c) dry-blended, and (d) pre-compounded; pre-expanded graphite at 10 wt.% (e) dry-blended, and (f) pre-compounded. The exterior wall is on the left-hand side

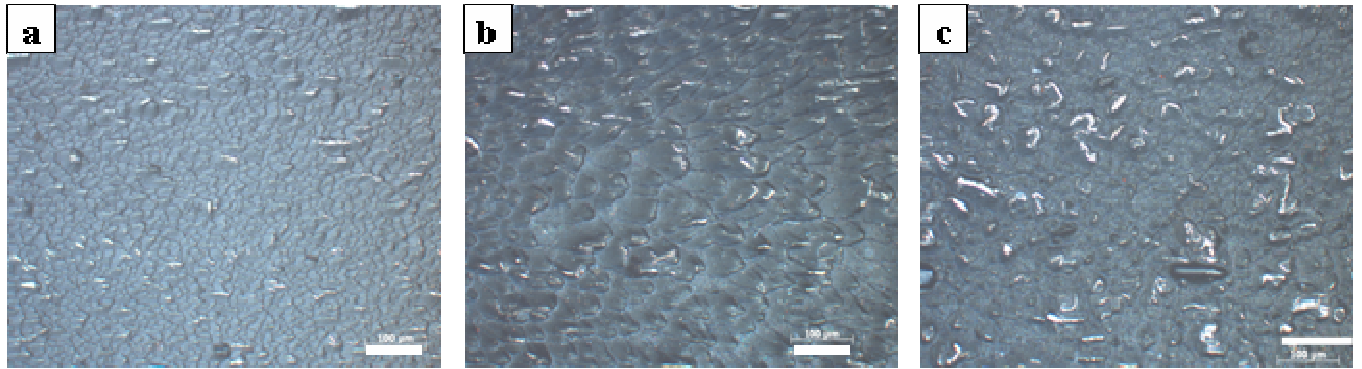


Figure 4-7 Photomicrographs of polished injection-moulded composite sections (5X magnification) containing 10 wt.% graphite: (a) Zimbabwean flake graphite, (b) expandable graphite, and (c) Pre-expanded graphite

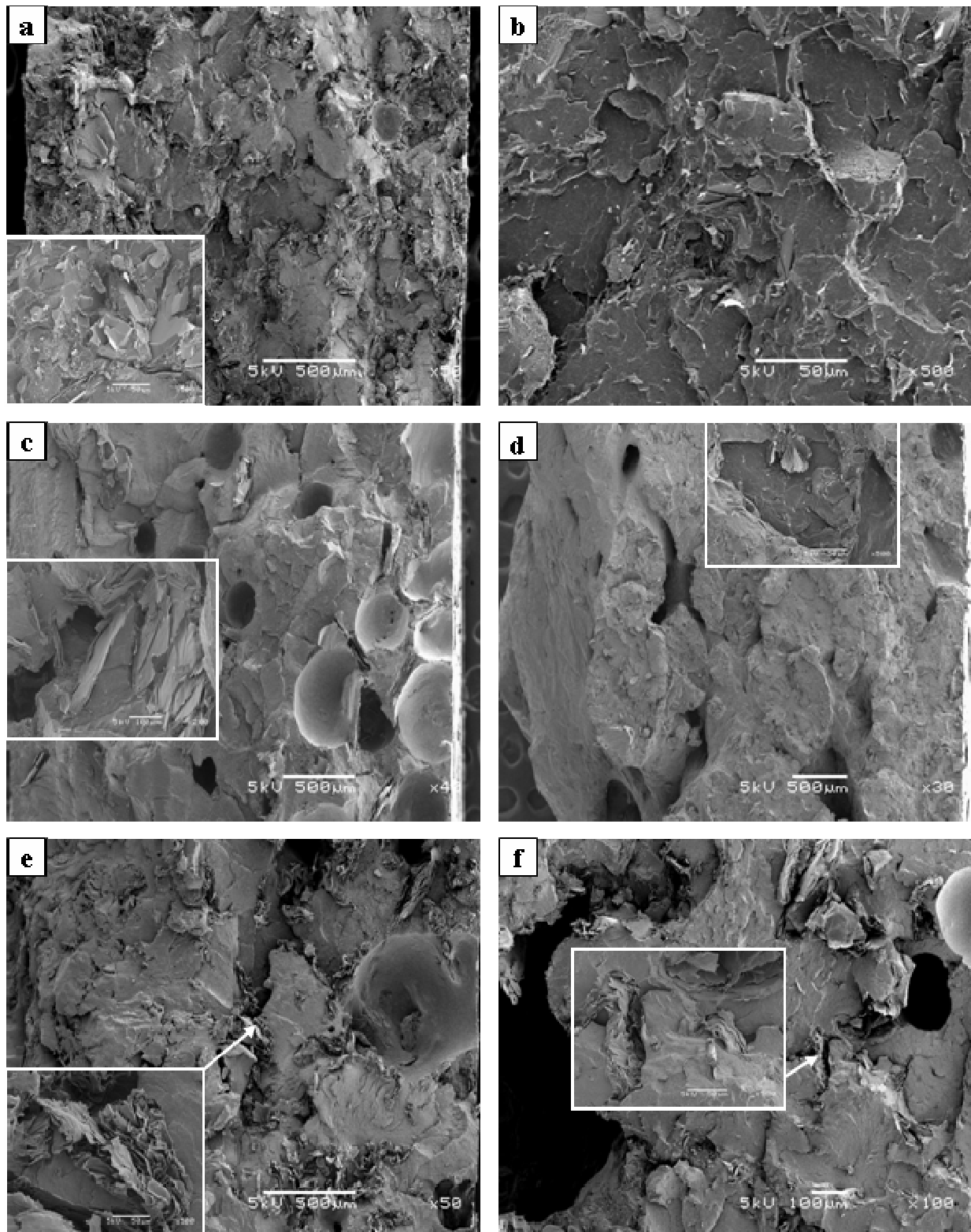


Figure 4-8 SEM fractographs of rotomoulded composites with 10 wt.% graphite: Zimbabwean flake graphite (a) dry-blended, and (b) pre-compounded; expandable graphite (c) dry-blended, and (d) pre-compounded; pre-expanded graphite (e) dry-blended, and (f) pre-compounded. The inserts show higher magnifications and the exterior wall is on the right-hand side

4.4 Rheology

Figure 4-9 shows the variation of the zero-shear viscosity of the graphite composites (evaluated at a shear rate of 0.01 s^{-1}) with temperature for LLDPE and 10 wt.%. The inclusion of graphite filler in the polyethylene matrix resulted in a significantly higher melt viscosity, almost double that of the neat LLDPE.

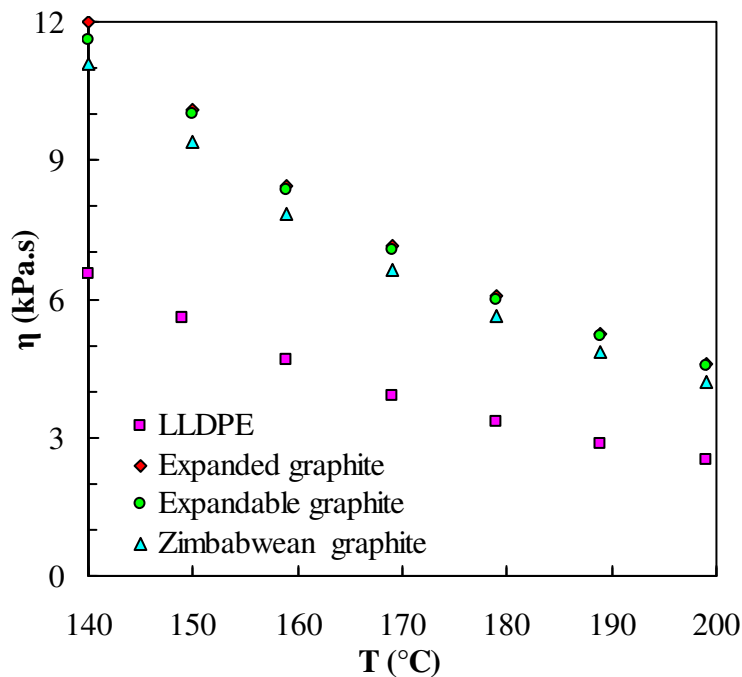


Figure 4-9 Variation of zero-shear viscosity of LLDPE/graphite composites with temperature (η viscosity, T melt temperature)

4.5 Porosity

Figure 4-10 shows the variation of the porosity of the dry-blended and pre-compounded rotomoulded LLDPE/graphite composites with graphite content. The pre-compounded samples exhibited high porosities, particularly for the expandable and pre-expanded graphite forms. At 10 wt.% graphite, the expandable and expanded graphite composites had porosities of 14% and 13% respectively, more than twice that observed for the pristine LLDPE.

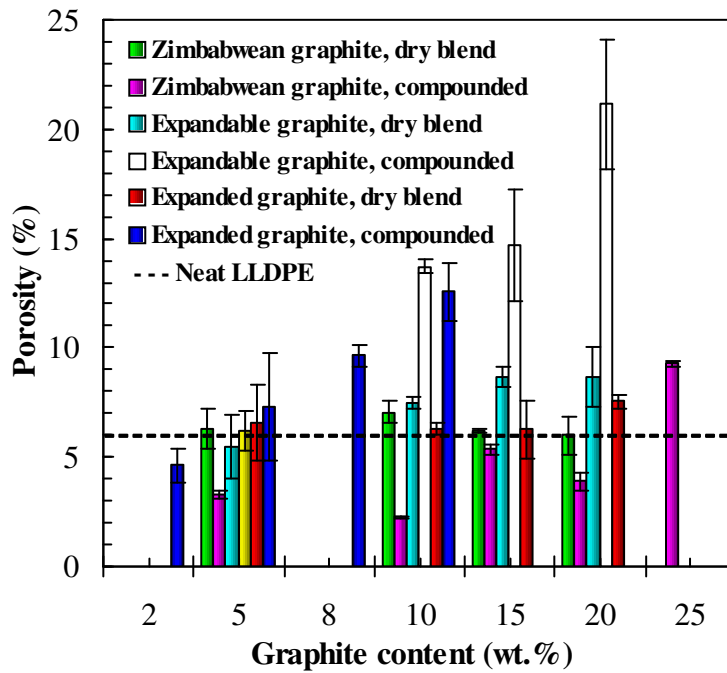


Figure 4-10 Variation of the porosity of LLDPE/graphite composites with graphite content

4.6 Differential scanning calorimetry

Figures 4–11, 4–12 and G–1 show DSC heating and cooling curves of the LLDPE and LLDPE/graphite composites. It was observed that the graphite fillers nucleate polyethylene crystallisation, hence the higher crystallisation temperatures of the composites. The crystallisation temperatures increased by as much 3 °C for the dry-blended rotomoulded composite and 6 °C for the compounded rotomoulded composite (Figure G-1).

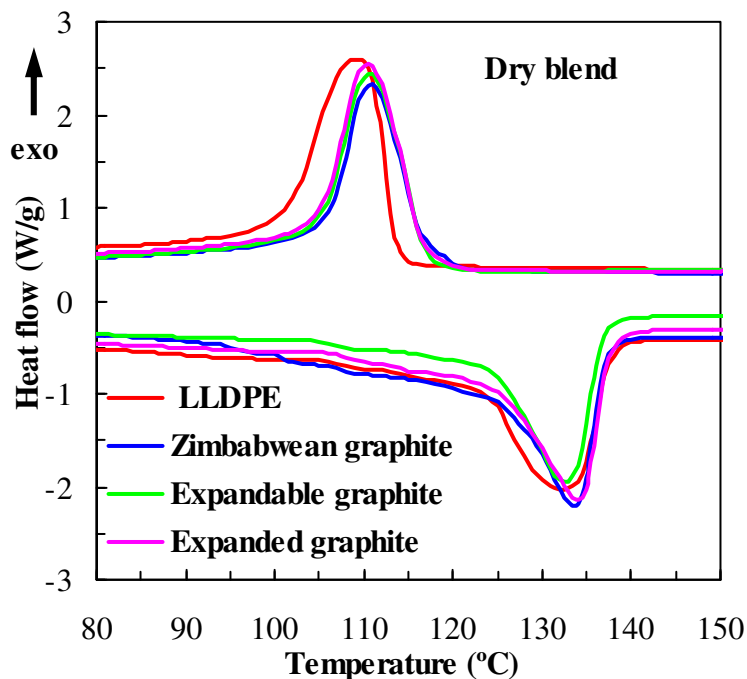


Figure 4-11 DSC scans for dry-blended rotomoulded graphite/LLDPE composites

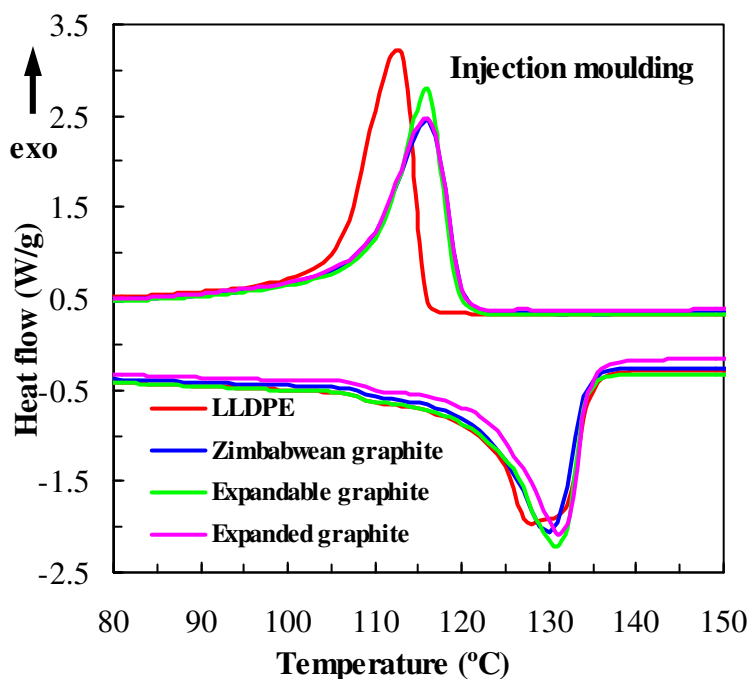


Figure 4-12 DSC scans for injection-moulded graphite/LLDPE composites

4.7 Surface resistivity

The surface resistivity of LLDPE and all injection-moulded graphite composites featured surface resistivity values exceeding $10^{14} \Omega/\square$. Figures 4-13 to 4-15 show the exterior surface resistivity values measured for the rotomoulded LLDPE/graphite composites made by the three processing methods and containing different graphite types. The resistivity of the composites showed the expected decrease in surface resistivity with increasing graphite content (Rosner, 2001).

Dry blend-prepared Zimbabwean flake graphite-based composites had lower resistivity values than those based on powders obtained from compounded and double-dumped samples (see Figure 4-13). At 10 wt.% graphite loading, the surface resistivity was $10^5 \Omega/\square$, equal to the upper limit of the conductive range. This was almost two orders of magnitude lower than the corresponding value for the melt-compounded composite, and 6 decades lower than that of the double-dumped composite. However, the resistivity values for compounded composites showed significantly less variability. The dry-blended and melt-compounded composites reached the IEC 61340-5-1 static dissipative rating at 5 and 10 wt.%, whereas the double-dumped composites only became static dissipative at 15 wt. %.

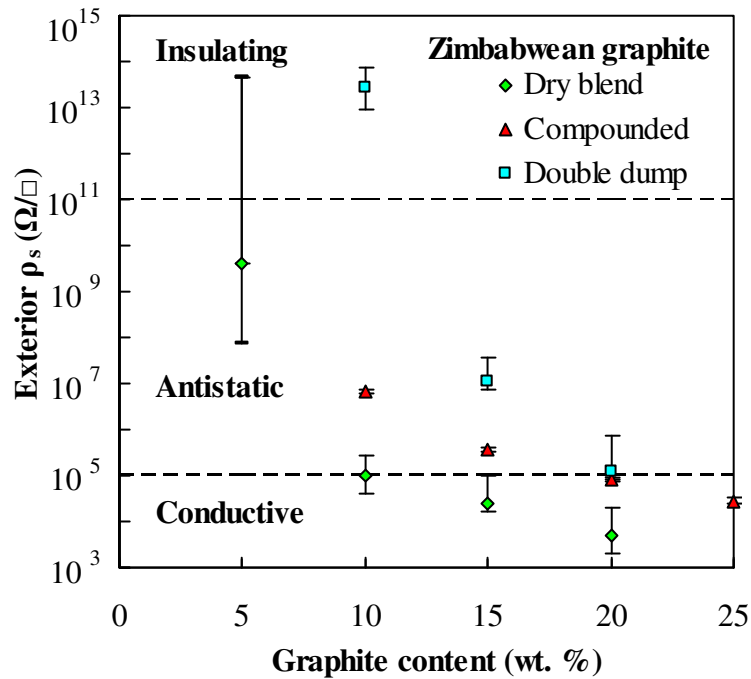


Figure 4-13 Exterior surface resistivity, rotomoulded LLDPE/Zimbabwean graphite composites

Dry-blended expandable graphite composites exhibited higher resistivity values and only achieved the static dissipative ranking above 20 wt.% filler (Figure 4-14). Compounded samples containing 10 wt.% or more graphite were rated static dissipative. However, the double-dumped composites were not static dissipative at all the graphite contents used.

The dry-blended expanded graphite-based composites also exhibited lower resistivity values than the corresponding compounded samples (Figure 4-15). They were more conductive than the composites based on expandable graphite and achieved the static dissipative rating at 8 and 10 wt.% graphite respectively.

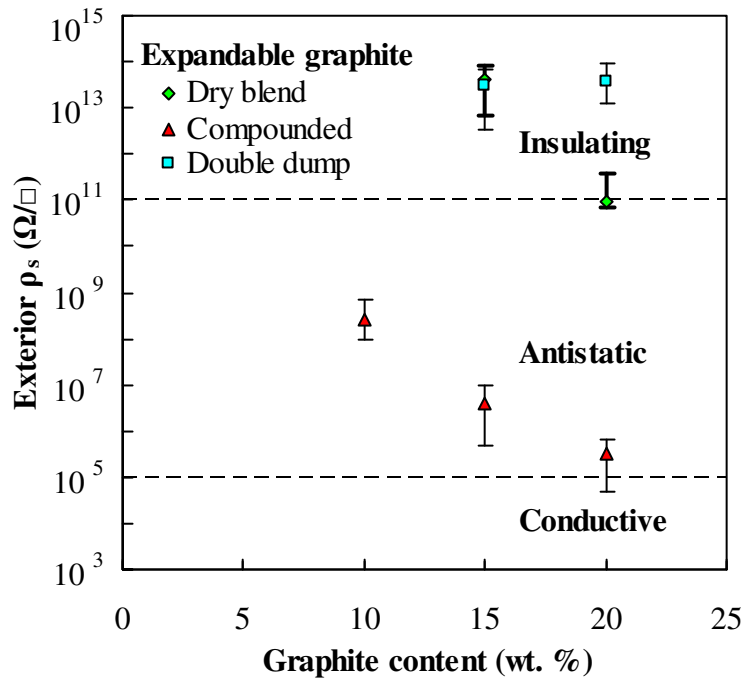


Figure 4-14 Exterior surface resistivity, rotomoulded LLDPE/expandable graphite composites

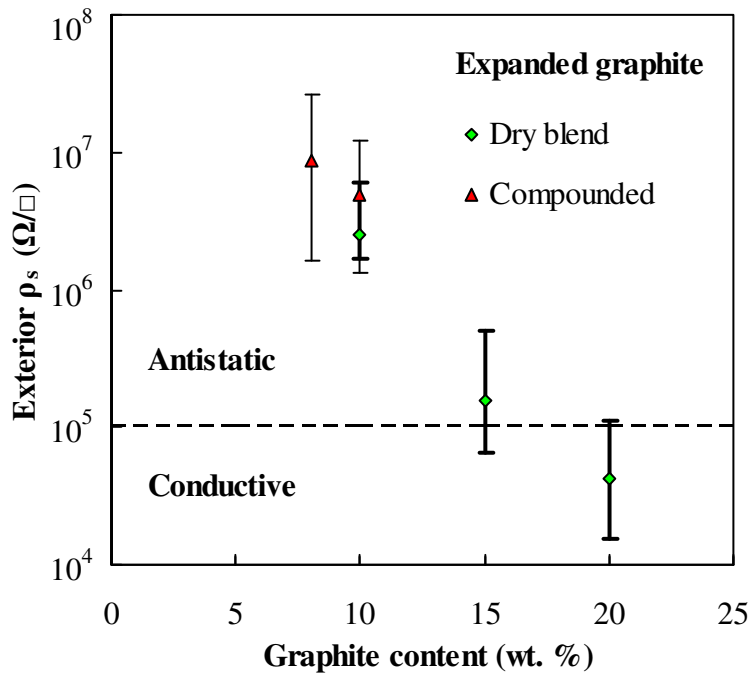


Figure 4-15 Exterior surface resistivity, rotomoulded expanded graphite composites

Figure 4-16 shows a comparison of the lowest surface resistivities for each graphite type. The dry-blended Zimbabwean graphite exhibited the lowest surface resistivities overall.

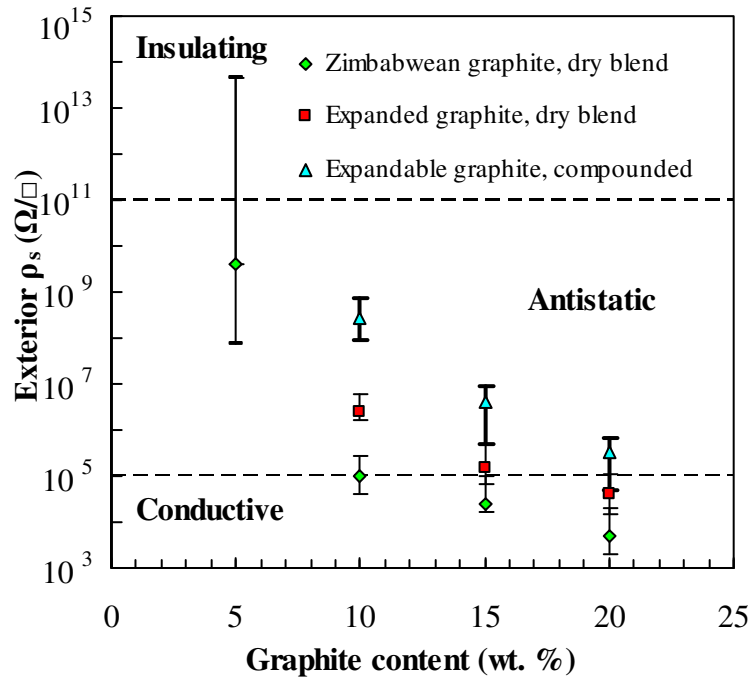


Figure 4-16 Lowest exterior surface resistivities of each rotomoulded graphite type

4.8 Mechanical properties

4.8.1 Young's modulus

The Young's moduli of the rotomoulded and injection moulded composites are listed in Table 4-3. The rotomoulded Zimbabwean graphite composites showed modest improvements in the Young's moduli up to 10 wt.% graphite content. Previous investigations of the moduli of rotomoulded composites also showed an initial improvement, and deterioration thereafter (Robert & Crawford, 1999; Wesley, 1999; Yan *et al.*, 2006). The expandable and expanded graphite composites did not show a marked improvement in the modulus. Improvements of 23%, 20% and 36% were observed in the moduli of the injection-moulded Zimbabwean, and expandable and expanded graphite composites respectively at 10 wt.% loading.

4.8.2 Tensile yield strength

The yield strength of all the rotomoulded graphite composites deteriorated with an increase in graphite content (Table 4-4). However, it is worth noting that the decrease in yield strength was only 10% for the dry-blended Zimbabwean flake graphite containing 5 wt.% graphite. At this graphite content, the dry blend composite was static dissipative. This could be an acceptable decrease in strength for some applications. A modest improvement was observed in the yield strength of all the injection-moulded composites. The improvement in the injection-moulded samples was more pronounced in the Zimbabwean flake graphite composites, with a 26% improvement at 20 wt.% graphite content.

Table 4-3 Effect of graphite type and content as well as processing method on the Young's modulus (MPa) of LLDPE/graphite composites

Processing method		Graphite content (wt.%)						
		0	2	5	8	10	15	20
Injection moulding	Neat LLDPE	189 ± 23						
Rotomoulding	Neat LLDPE	204 ± 56						
<i>Zimbabwean graphite</i>								
Injection moulding			216 ± 8		233 ± 11	265 ± 4	310 ± 3	320 ± 13
Rotomoulding	Dry-blended		203 ± 37		226 ± 13	225 ± 22	204 ± 19	
	Compounded		211 ± 54		231 ± 23	189 ± 39	179 ± 42	111 ± 12
	Double-dumped		238 ± 21		243 ± 67	209 ± 30	198 ± 25	
<i>Expandable graphite</i>								
Injection moulding			207 ± 20		226 ± 5	249 ± 28	282 ± 38	
Rotomoulding	Dry-blended		186 ± 17		145 ± 15	141 ± 20	162 ± 68	
	Compounded		129 ± 22		123 ± 9	104 ± 27	81 ± 9	
	Double-dumped		197 ± 16		192 ± 72	233 ± 38	179 ± 43	
<i>Expanded graphite</i>								
Injection moulding		196 ± 21	239 ± 16	235 ± 9	257 ± 20			
Rotomoulding	Dry-blended		210 ± 22		178 ± 14	182 ± 24	158 ± 8	
	Compounded	186 ± 36	188 ± 23	149 ± 52	101 ± 26			

Table 4-4 Effect of graphite type and content as well as processing method on the yield strength (MPa) of LLDPE/graphite composites

Processing method		Graphite content (wt.%)							
		0	2	5	8	10	15	20	25
Injection moulding	Neat LLDPE	16.5 ± 0.2							
Rotomoulding	Neat LLDPE	21.5 ± 0.4							
<i>Zimbabwean graphite</i>									
Injection moulding				18.2 ± 0.1		18.4 ± 0.6	19.4 ± 0.3	20.8 ± 0.3	20.6 ± 0.1
Rotomoulding	Dry-blended			19.4 ± 0.4		17.4 ± 0.9	15.9 ± 1.4	13.9 ± 1.7	
	Compounded			19.6 ± 1.0		18.1 ± 1.4	14.8 ± 1.8	12.3 ± 0.6	6.0 ± 2.3
	Double-dumped			19.2 ± 0.3		17.3 ± 0.3	16.3 ± 0.6	13.8 ± 1.0	
<i>Expandable graphite</i>									
Injection moulding				17.6 ± 0.4		17.5 ± 0.4	17.9 ± 0.4	18.5 ± 0.9	
Rotomoulding	Dry-blended			16.9 ± 0.4		12.1 ± 0.4	9.7 ± 0.7	9.2 ± 1.1	
	Compounded			13.6 ± 0.7		10.6 ± 0.8	4.3 ± 0.5	0.8 ± 0.4	
	Double-dumped			18.2 ± 0.7		14.0 ± 2.8	12.3 ± 0.5	8.9 ± 0.8	
<i>Expanded graphite</i>									
Injection moulding			15.9 ± 0.4	17.1 ± 0.4	17.2 ± 0.6	17.3 ± 0.4			
Rotomoulding	Dry-blended			18.3 ± 0.3		15.3 ± 0.4	12.7 ± 0.3	11.2 ± 1.0	
	Compounded		18.8 ± 0.4	18.1 ± 0.6	11.5 ± 0.2	7.9 ± 0.8			

4.8.3 Elongation-at-break

Table 4-5 shows the elongation-at-break of the graphite composites. The neat rotomoulded LLDPE exhibited a high elongation-at-break of 1 044%, compared to that of the neat injection-moulded LLDPE, which was 441%. The elongation-at-break for the injection-moulded composites initially improved with graphite content before it deteriorated. Modest improvements of up to 12% (5 wt.% Zimbabwean graphite), 8% (5 wt.% expandable graphite) and 10% (2 wt.% expanded graphite) were observed. The elongation-at-break for all the rotomoulded composites decreased dramatically with an increase in graphite content.

4.8.4 Impact strength

The falling-weight impact strength (Gardner Impact) of the rotomoulded composites decreased drastically with increase in graphite content (Table 4-6). A more gradual decrease in the impact strength was observed for the injection-moulded composites. The rotomoulded samples exhibited a brittle failure mode; they showed radial cracks from the impact point. By contrast, the injection-moulded samples showed ductile failures. Previous studies also found a decrease in the impact strength of graphite/polyethylene composites (Wang *et al.*, 2001; She *et al.*, 2007).

Table 4-5 Effect of graphite type and content as well as processing method on the elongation-at-break (%) of LLDPE/graphite composites

Processing method		Graphite content (wt.%)							
		0	2	5	8	10	15	20	25
Injection moulding	Neat LLDPE	441 ± 9							
Rotomoulding	Neat LLDPE	1044 ± 82							
<i>Zimbabwean graphite</i>									
Injection moulding				494 ± 25		456 ± 11	418 ± 13	69 ± 2	38 ± 3
Rotomoulding	Dry-blended			21 ± 3		15 ± 1	12 ± 1	10 ± 2	
	Compounded			14 ± 3		12 ± 1	11 ± 2	10 ± 3	10 ± 2
	Double-dumped			28 ± 3		20 ± 2	16 ± 1	11 ± 2	
<i>Expandable graphite</i>									
Injection moulding				478 ± 20		461 ± 30	372 ± 55	126 ± 97	
Rotomoulding	Dry-blended			30 ± 3		17 ± 1	14 ± 1	11 ± 1	
	Compounded			16 ± 2		13 ± 3	8 ± 0	5 ± 1	
	Double-dumped			39 ± 7		23 ± 3	20 ± 2	18 ± 2	
<i>Expanded graphite</i>									
Injection moulding			485 ± 19	445 ± 7	435 ± 16	418 ± 21			
Rotomoulding	Dry-blended			20 ± 2		14 ± 1	11 ± 1	11 ± 1	
	Compounded		27 ± 6	16 ± 3	13 ± 3	13 ± 2			

Table 4-6 Falling-weight impact (Gardner Impact) resistance of LLDPE/graphite composites

Processing method		Graphite content (wt.%)							
		0	2	5	8	10	15	20	25
Injection moulding	Neat LLDPE	14.16							
Rotomoulding	Neat LLDPE	9.19							
<i>Zimbabwean graphite</i>									
Injection moulding				8.72		9.69	8.67	7.63	6.19
Rotomoulding	Dry-blended			0.91		0.77	0.66		
	Compounded			0.88		0.58	0.52	0.55	0.75
	Double-dumped			1.21		0.75	0.77	0.44	
<i>Expandable graphite</i>									
Injection moulding				9.57		7.54	7.34	6.38	
Rotomoulding	Dry-blended			3.83		2.05	1.16	1.19	
	Compounded			1.30		0.94	1.21	1.16	
	Double-dumped			5.12		3.36	1.82	1.46	
<i>Expanded graphite</i>									
Injection moulding			10.59	9.03	7.58	6.23			
Rotomoulding	Dry-blended			2.36		0.99	0.82	0.72	
	Compounded			3.26	1.09	1.21	1.19		

4.9 Thermal properties

The double-dumped rotomoulded composites were excluded in the thermal analysis as they exhibited poor antistatic properties and showed poor dispersion of the graphite fillers.

4.9.1 TGA

Figure 4-17 shows the residual mass obtained from the TGA of the graphites, LLDPE and composites at 10 wt.% graphite content for melt-compounded rotomoulded composites. The Zimbabwean graphite and expanded graphite only lose weight beyond 600 °C. However, the expandable graphite loses about 10% weight between 300–500 °C. All the composite samples at 10 wt.% had an initial weight loss at about 400 °C, which is the temperature at which LLDPE also had an initial weight loss. The samples processed by dry blending and injection moulding exhibited the same trends.

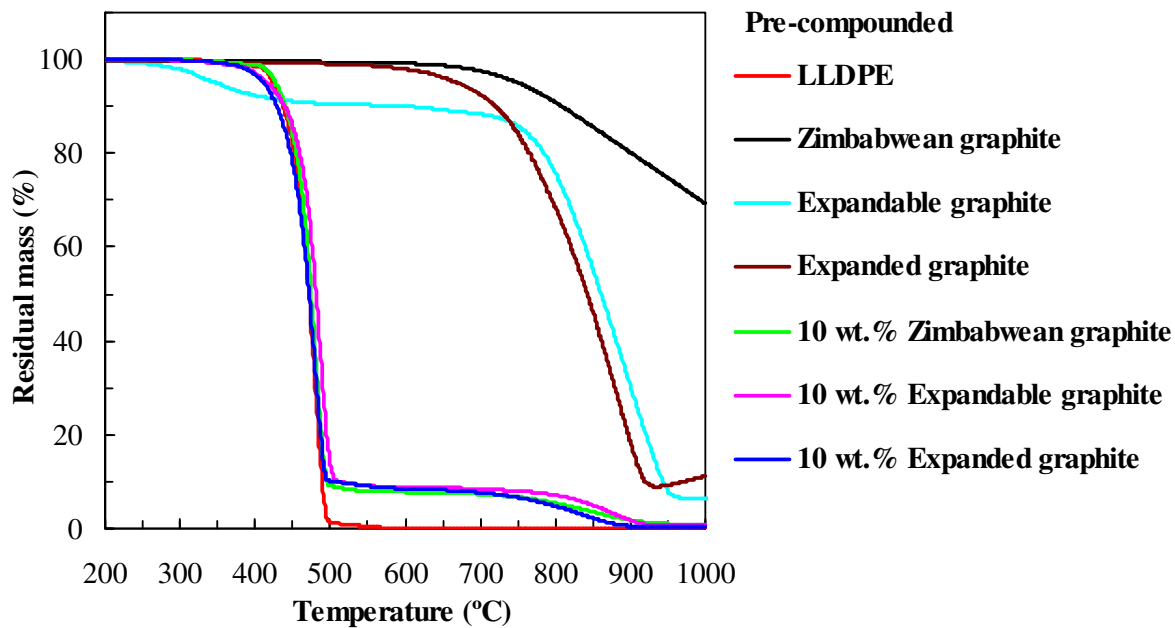


Figure 4-17 TGA of compounded rotomoulded composites with graphite at 10 wt.% content

4.9.2 Thermal conductivity

The variation of the thermal conductivity with graphite content for the different graphite types and also the different mixing techniques used in rotomoulding is shown in Table 4-7. The dry-blended and melt-compounded rotomoulded Zimbabwean graphite composites showed a steady improvement in the thermal conductivity with an increase in graphite content. However, the dry-blended composites exhibited higher thermal conductivity values compared to the melt-compounded composites. The dry-blended Zimbabwean graphite composites attained a conductivity value of 0.74 W/m.K at a graphite content of 20 wt.%, a 76% improvement, compared to 64% improvement of the melt-compounded composites at the same loading.

Improvements in the thermal conductivities were also observed for dry-blended expandable and expanded graphite composites. However, the melt-compounded composites for the expandable and expanded graphite did not show much improvement. The dry-blended expanded graphite composites exhibited the best overall thermal conductivity with an 88% improvement at a graphite content of 20 wt.%.

Injection-moulded LLDPE/graphite composites also showed an improvement in thermal conductivities with an increase in graphite content (Table 4-7). Improvements of 34%, 32% and 62% were observed for composites containing 10 wt.% Zimbabwean, expandable and expanded graphite respectively. However, the conductivity values for injection-moulded composites at 10 wt.% are comparable to those of dry-blended composites at the same loading (Table 4-7).

Table 4-7 Effect of graphite type and content as well as processing method on the thermal conductivity (W/mK) of LLDPE/graphite composites

<i>Processing method</i>		Graphite content (wt.%)							
		0	2	5	8	10	15	20	25
Injection moulding	Neat LLDPE	0.47 ± 0.00							
Rotomoulding	Neat LLDPE	0.42 ± 0.01							
<i>Zimbabwean graphite</i>									
Injection moulding				0.62 ± 0.00		0.63 ± 0.00	0.70 ± 0.02	0.93 ± 0.01	1.18 ± 0.05
Rotomoulding	Dry blended					0.65 ± 0.02		0.74 ± 0.01	
	Compounded			0.45 ± 0.05		0.56 ± 0.00	0.63 ± 0.04	0.69 ± 0.07	0.74 ± 0.01
<i>Expandable graphite</i>									
Injection moulding				0.62 ± 0.03		0.62 ± 0.00	0.77 ± 0.01	1.03 ± 0.07	
Rotomoulding	Dry blended					0.57 ± 0.02		0.67 ± 0.02	
	Compounded			0.31 ± 0.03		0.29 ± 0.01	0.39 ± 0.02	0.39 ± 0.01	
<i>Expanded graphite</i>									
Injection moulding			0.51 ± 0.00	0.49 ± 0.00	0.59 ± 0.02	0.76 ± 0.03			
Rotomoulding	Dry blended					0.68 ± 0.02		0.79 ± 0.09	
	Compounded		0.48 ± 0.05	0.45 ± 0.23	0.24 ± 0.02	0.26 ± 0.02			

4.10 Discussion

4.10.1 DSC

The higher crystallisation temperatures observed for the LLDPE/graphite composites resulted in faster cooling rates (Figures 4-11 and 4-12). This is desirable for rotational moulding as cycle times will be reduced. The degree of crystallisation was calculated using specific enthalpies obtained from DSC according to:

$$X_c = \frac{\Delta H_m}{\Delta H_m^+} \quad (4-1)$$

where X_c is the degree of crystallisation, ΔH_m is the specific melting enthalpy of LLDPE or the LLDPE/graphite composites, and ΔH_m^+ is the specific enthalpy of 100% crystalline polyethylene. A value of $\Delta H_m^+ = 293 \text{ J/g}$ (Krupa *et al.*, 2004) was used for the calculations.

Rotomoulded and injection-moulded LLDPE had degrees of crystallisation of 61% and 65% respectively. Disregarding the outliers, a decrease of about $9.3 \pm 2.7\%$ in the crystallinity of the LLDPE/graphite composites was observed, which is close to the 10 wt.% content of graphite at which the DSC scans were performed. Therefore no significant changes were observed in the degree of crystallisation due to the inclusion of graphite in the polymer matrix. Krupa *et al.* (2004) also did not observe significant changes in the degree of crystallinity of graphite/polyethylene composites.

4.10.2 Surface resistivity

The variability of the resistivity data is very low for melt-compounded Zimbabwean flake graphite composites and high for the dry blended and double dumped composites (Figure 4-13). However, better conductivity performance was achieved with dry blending. As observed earlier in section 4.3, optical microscopy and SEM showed different dispersions of the graphite fillers resulting from the different mixing methods employed. The good dispersion observed in the compounded composites does not necessarily promote the formation of conductive pathways. The graphite flakes in dry-blended composites appear to feature randomly oriented and interconnected clusters that are more conducive to the

formation of conductive pathways. Dry blending did not have the same effect on expandable graphite (Figure 4-6). In contrast, the compounded expandable graphite composites showed a more random orientation of the graphite flakes, which explains the better conductivity in these composites. A previous study showed that the percolation threshold decreases with a reduction in graphite platelet size (Nagata *et al.*, 1999). Thus the observed decrease in graphite flake size in the Zimbabwean flake and expanded graphite composites (Figure 4-6) appears to have contributed to the lower resistivity values achieved.

Double-dumped composites of the Zimbabwean flake and expandable graphite featured graphite flakes aligned mostly along the wall of the moulding (Figure E1, Appendix E). This orientation does not promote the formation of conductive pathways, hence the high resistivities.

The higher surface resistivity of the injection-moulded samples can be explained by the good dispersion of all the types of graphite in the polymer matrix, which does not promote the formation of conductive paths (Figure 4-7). Another observation in Figure 4-7 was the tendency for the graphite platelets to be partially oriented in the direction of melt flow. Apparently some expanded graphite platelets were damaged or crumpled by the high-shear melt processing.

4.10.3 Mechanical properties

Polymer reinforcement depends on effective stress transfer from the matrix to the filler. Strong matrix-filler interaction is a prerequisite for effective stress transfer (Fu *et al.*, 2008). Rotomoulding is a pressure- and shear-free process. In comparison, injection moulding involves pressure and high-shear mixing that facilitates wetting and dispersion of the graphite fillers, hence the better improvement in the moduli and strength. The difference in polarity between graphite and polyethylene results in poor filler-matrix interfacial adhesion. Also, loose expanded graphite platelet stacks are visible, with the expanded graphite squashed and folded, but not exfoliated (Figure 4-8). This weakens the composites.

Cavities in wall cross-sections, graphite agglomerates and surface flaws (including pinholes) all deteriorate mechanical properties (Figures 4-6 and 4-8). Voids do not carry any

load (Verbeek, 2001). The injection-moulded composites were void free (Figure 4-7), hence the better modulus and strength values.

The rotomoulded graphite composites showed a higher incidence of cavities and surface flaws. Resins with low zero-shear viscosities sinter easily and their flowability enables the filling of intricate mould details and good surface finishes (Kontopoulou & Vlachopoulos, 1999). The flake-like nature and random dispersion of the graphite particles makes it more difficult for gas bubbles to escape. The higher apparent melt viscosity of the composites (Figure 4-9) makes degassing even more difficult.

Spence & Crawford (1996) showed that rotomoulding polymers with relatively higher viscosities resulted in more bubbles. In the range from 140 °C to 200 °C the melt viscosity decreased according to the Arrhenius relationship.

$$\eta = \eta_0 e^{E_a / RT} \quad (4-2)$$

where η is the zero-shear viscosity; η_0 is the pre-exponential constant with dimensions of viscosity; E_a is the activation energy; R is the gas constant and T is the absolute temperature. The activation energy was the same for the resin and the compounds and equal to $26.5 \pm 0.3 \text{ kJ}\cdot\text{mol}^{-1}\cdot\text{K}^{-1}$. The fits of this relationship are shown in Figure 4-18.

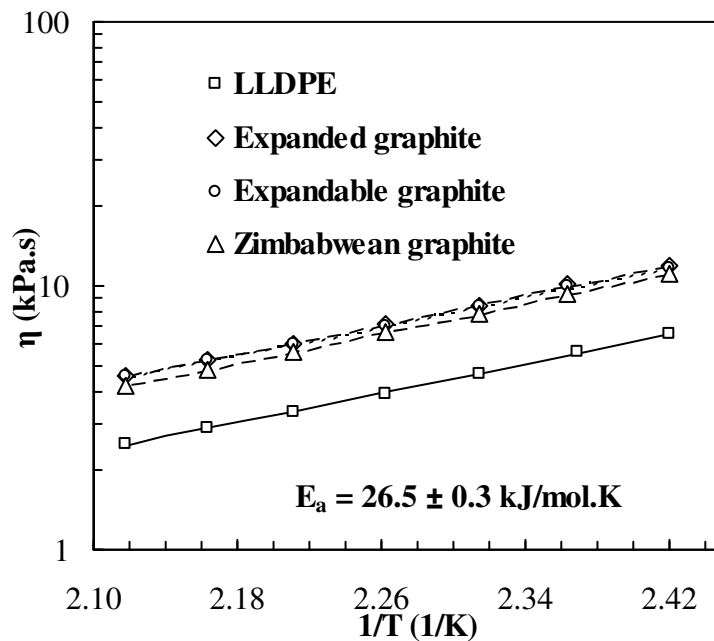


Figure 4-18 Fits of the Arrhenius equation to the viscosity data of polyethylene/graphite composites

Spence & Crawford (1996) also observed that for bubbles to travel out of the polymer melt, the viscosity should be less than 3–4 kPa.s. From Figure 4-9 it is evident that melt temperatures beyond 200 °C would be necessary for this to occur. Trapped air bubbles can be detrimental to the mechanical properties due to thermo-oxidative degradation.

Surface flaws (Young & Lovell, 1991) and particle clusters (Yasmin & Daniel, 2004) are stress concentration points that weaken the composites. Particle clusters are noticeable (Figures 4-6 and 4-8), particularly in the composites that are conductive. The rotomoulded compounded samples were expected to perform much better due to better dispersion and wetting, compared to the dry-blended or double-dumped composites, but they also had voids and pinholes.

In the injection-moulded composites (Figure 4-7), the graphite filler particles appeared partially aligned to the direction of the melt flow (horizontal direction in the photomicrographs). As this was the direction of tensile testing, it provided better reinforcement. Preferred orientations were not apparent in the dry-blended and compounded rotomoulded composites.

A reduction in the elongation-at-break observed in the rotomoulded composites is usually observed in filled polymers. The particles act as stress concentration points that initiate crack propagation (Krupa & Chodak, 2001). It has been previously suggested that if the interaction between graphite platelets and polyethylene was stronger than that between graphite nanoplatelets, then the elongation-at-break could improve as a result of oriented graphite platelets sliding over each other (Wang & Chen, 2010). This explanation is suggested for the initial improvement in the elongation of injection-moulded composites.

Rigid fillers decrease the impact strength of filled polymers due to differences in stiffness (Wang *et al.*, 2001). However, the rapid deterioration of the impact strength and the mode of failure of rotomoulded composites compared to the injection-moulded composites suggest poor adhesion between the graphite filler particles and the polymer matrix. The surface flaws observed in the composites decreased the impact strength. Particle clusters (DeArmitt & Hancock, 2003) and poor dispersion also contributed to a decrease in impact strength (Chen *et al.*, 2001).

Modelling the Young's modulus

The Halpin-Tsai equations (Halpin & Kardos, 1976) were fit to the modulus data due to their wide use in predicting the modulus of composites (Tucker III & Liang, 1999; Fornes & Paul, 2003). Appropriate shape factors for platelets fillers such as graphite have also been proposed (Van Es, 2001).

Figure 4-19 shows least square fits of the Halpin-Tsai equations for the platelets to Young's modulus data of injection-moulded composites. Perfect platelet alignment in the longitudinal direction and random platelet orientation were considered. The tensile modulus for the graphite was taken as the in-plane value of 1 TPa for the longitudinal modulus, and the c-axis value of 36.5 GPa for the transverse modulus (Pierson, 1993). The tensile moduli of the LLDPE were taken as the measured values listed in Table 4-3. By assuming perfect alignment and using Equation 2-12 for the longitudinal modulus, good fits were obtained using shape factors $\zeta_L = 5.1$ and $\zeta_L = 3.73$ for Zimbabwean flake graphite and expandable graphite respectively. By considering random orientation of the platelets and using Equation 2-14 with ζ_T fixed at $\zeta_T = 2$, good fits were obtained using $\zeta_L = 8.39$ and $\zeta_L = 5.88$ for Zimbabwean flake graphite and expandable graphite respectively. The fits for perfect platelet alignment and random platelet orientation lie on the same lines (Figure 4-19). These results provide an indication of the residual aspect ratios of the platelets. For perfect alignment of the platelets the aspect ratios were calculated to be 7.65 and 5.60 for the Zimbabwean flake graphite and expandable graphite respectively. For random orientation of the platelets, the aspect ratios were calculated to be 12.59 and 8.36 for the Zimbabwean flake graphite and expandable graphite respectively. The values of the shape factors confirm the anisotropic nature of the graphite flakes. The Halpin-Tsai model could not be applied to the tensile moduli data for the rotomoulded composites because they deteriorated with graphite content.

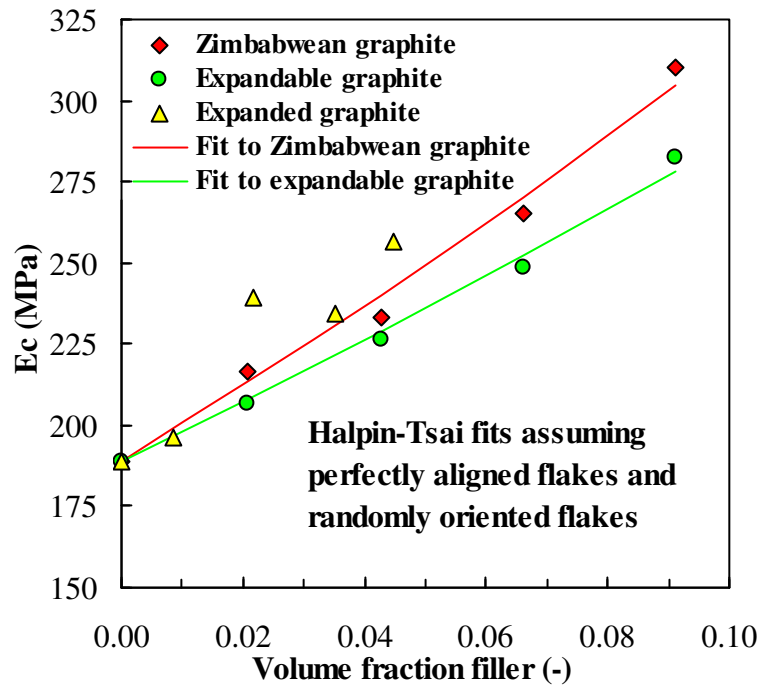


Figure 4-19 Fitting the Halpin-Tsai model to Young's moduli data of injection-moulded composites. The lines generated for perfect platelet alignment and completely random platelet orientations are indistinguishable in this plot

4.10.4 Thermal properties

TGA

The presence of the graphite in the polyethylene matrix does not appear to affect the mass loss of the polyethylene as the mass loss for all the composites commences at about 400 °C. The residual mass of the graphite composites at the temperature (about 500 °C) at which the LLDPE mass declines to zero is 10%, which confirms that the composites contained 10 wt.% graphite.

Thermal conductivity

Due to the large differences in thermal conductivity between the graphite fillers and polyethylene matrix, it is expected that the thermal conductivity of the composites increases with filler loading. This was the observation in all the dry-blended composites and the

compounded Zimbabwean graphite. The improvement in the thermal conductivity of the dry-blended composites is attributed to particle clusters that form conductive pathways through the matrix. These were observed in the light microscopy photomicrographs and SEM micrographs (Figures 4-6 and 4-8). Agari *et al.* (1991) showed that thermal conductivities were higher in composites that exhibited dispersion states in which graphite could easily form conductive chains.

An interesting observation was that the dry-blended composites also exhibited lower resistivity values and therefore good antistatic performance. The non-improvement of the thermal conductivity of compounded expanded and expandable graphite was unexpected.

Although graphite has a very high thermal conductivity, only a marginal improvement was observed in the dry-blended and injection-moulded composites. Bigg (1995) has shown that once the ratio of filler conductivity to matrix conductivity is over 100, the conductivities will reach limiting values and there will not be a significant difference in the conductivities of composites.

The poor performance of rotomoulded compounded samples is attributed to high porosity in the final mouldings (Figure 4-10). This is in agreement with the observation of Osman *et al.* (2007). Pores in the mouldings scatter phonons, causing thermal resistance, thus reducing the thermal conductivity (Sumirat *et al.*, 2006). These pores or voids were observed in the light microscopy photomicrographs in Figures 4-6 and 4-8. The formation of the voids was attributed to the enhanced viscosity of the composites as a result of the inclusion of graphite fillers (section 4.9.3)

The predominantly better thermal conductivity values of injection-moulded composites are attributed to better interaction of the graphite fillers and the polymer matrix in the injection-moulded composites. Rotomoulding is a pressure- and shear-free process. In comparison, injection moulding involves pressure and high-shear mixing that facilitates wetting and dispersion of the graphite fillers in injection moulding. The difference in polarity between graphite and polyethylene results in poor filler-matrix interfacial adhesion. Poor bonding between the matrix and filler increases the interfacial thermal contact resistance (Dong, 2005). Also, no voids were apparent in the injection-moulded samples (Figure 4-7).

Modelling the thermal conductivity

The geometric mean model and the Halpin-Tsai and Lewis-Nielsen models were fitted to the thermal conductivity data.

Following the protocol of Picken *et al.* (2011), the maximum packing fraction v_m was set to $v_m = 1$ in Equation 2-30 so that the Lewis-Nielsen model (Equation 2-27) was effectively the Halpin-Tsai model (Equation 2-12) and fit to the thermal conductivity data.

The corrected shape factors for platelet fillers and averaging scheme proposed by van Es (2001) for the tensile modulus were used to fit the Halpin-Tsai model to the thermal conductivity data. The shape factors are given as $A_L = \frac{2}{3} \frac{w}{t}$ for the longitudinal thermal conductivity (λ_{CL}) and $A_T = 2$ for the transverse thermal conductivity (λ_{CT}) respectively. $\frac{w}{t}$ is the platelet aspect ratio α with w and t being the platelet width and thickness respectively.

The composite thermal conductivity is then given by the averaging scheme (Van Es, 2001) as

$$\lambda_c = 0.49\lambda_{CL} + 0.51\lambda_{CT} \quad (4-3)$$

where λ_c is the composite modulus, and λ_{CL} and λ_{CT} are evaluated from the Halpin-Tsai model.

The data were also fit to the Lewis-Nielsen model with the maximum packing fractions determined from the tap density and the density of graphite (Table 4-1). The maximum packing fractions of the Zimbabwean and expandable graphite were determined to be 0.34 and 0.37 respectively.

Figures 4-20 and 4-21 show fits of the geometric mean model and least square fits of the Halpin-Tsai model to the thermal conductivity data of the rotomoulded (dry blended composites) and injection-moulded composites respectively. In the geometric mean model, the in-plane thermal conductivity value for graphite of 3 000 W/m.K was used. The thermal conductivities of the rotomoulded and injection-moulded LLDPE used are given in Table 4-7.

The geometric mean model fits the thermal conductivity data well at low volume fractions of graphite fillers for both rotomoulded and injection-moulded composites in agreement with recent studies (Ye *et al.*, 2006). However, at higher volume fractions it tends to over-predict the thermal conductivity.

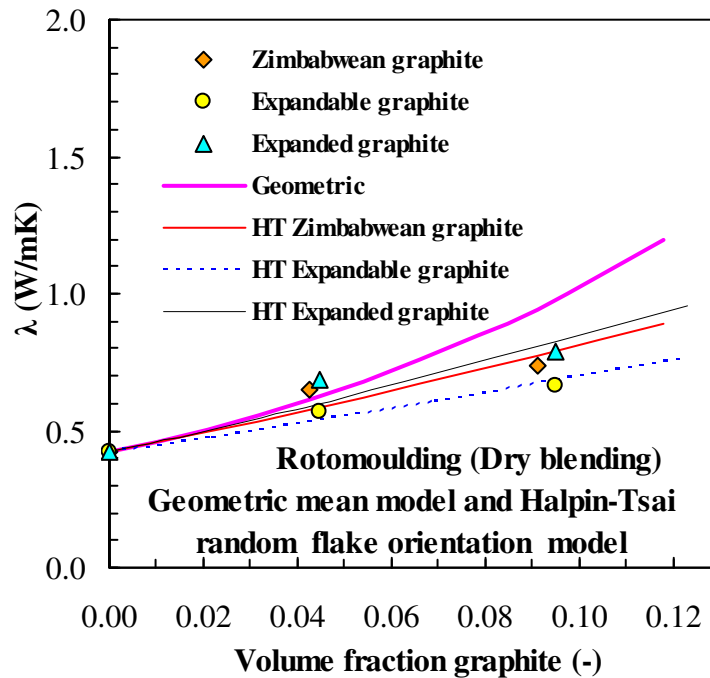


Figure 4-20 Fits of the geometric mean model and least square fits of the Halpin-Tsai (HT) model to the thermal conductivity data of the rotomoulded composites. The Nielsen-Lewis model fits lie on those of the Halpin-Tsai model

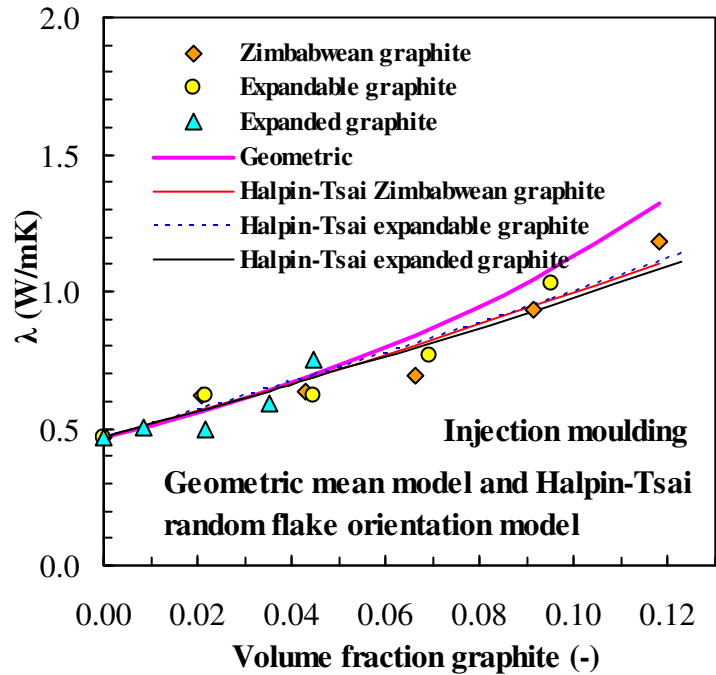


Figure 4-21 Fits of the geometric mean model and least square fits of the Halpin-Tsai model to the thermal conductivity data of the injection-moulded composites. The Nielsen-Lewis model fits lie on those of the Halpin-Tsai model

Using the Halpin-Tsai model, perfect platelet alignment in the longitudinal direction and random platelet orientation were considered. The thermal conductivity of the graphite was taken as the in-plane value of 3 000 W/m.K for the longitudinal thermal conductivity, and the c-axis value of 6 W/m.K for the transverse thermal conductivity (Sengupta *et al.*, 2011). The thermal conductivities of the rotomoulded and injection-moulded LLDPE used are given in Table 4-7.

The shape factors for injection-moulded composites are similar when a particular platelet orientation is assumed, either perfect platelet alignment or random orientation (Table 4-8). The shape factors for random platelet orientation are approximately twice those for perfect alignment.

Table 4-8 Halpin-Tsai model shape factors for estimating the thermal conductivity of LLDPE/graphite composites

	Injection moulding		Rotomoulding (Dry-blended)	
	Perfect alignment	Random	Perfect alignment	Random
Zimbabwean graphite	9.11	17.21	7.35	13.61
Expandable graphite	9.16	17.30	4.96	8.72
Expanded graphite	8.75	16.44	8.17	15.29

The thermal conductivity shape factors of the injection-moulded Zimbabwean and expandable graphite composites were compared to the tensile modulus shape factors of the same composites reported in section 4.9.3.1. It was found that the shape factors required to fit the thermal conductivity data were larger than those required to fit the tensile moduli for the injection-moulded composites (more than twice as large). This observation is in agreement with the results of Picken *et al.* (2011) for irregularly shaped particles.

The shape factors for the thermal conductivity of the dry-blended rotomoulded composites are lower than those for the injection-moulded composites, but also exhibit the same trend as those for injection moulding when the Halpin-Tsai model is used (Table 4-8). Random orientation of the platelets results in shape factors approximately twice those for perfect alignment. The poor interaction between graphite fillers and polyethylene in the dry-blended samples is suggested as the cause for the lower shape factors, and hence lower conductivity compared to the injection-moulded composites.

Table 4-9 shows the shape factors obtained by fitting the Lewis-Nielsen model using the maximum packing fractions obtained in this work. The fits lie on the same lines as those of the Halpin-Tsai model in Figures 4-20 and 4-21. The shape factors arising from the Lewis-Nielsen model are lower than those from the Halpin-Tsai model. The shape factors for injection-moulded composites approximate the values given in the literature for randomly oriented rods with aspect ratios of 15 (Nielsen, 1974). The shape factors for the rotomoulded composites approximate those for randomly oriented rods with aspect ratios of 10.

Table 4-9 Nielsen-Lewis model shape factors for estimating the thermal conductivity of LLDPE/graphite composites

	Injection moulding	Rotomoulding (Dry-blended)
Zimbabwean graphite	7.90	6.46
Expandable graphite	8.45	4.30

CHAPTER 5 : CONCLUSIONS AND RECOMMENDATIONS

The surface resistivities, thermal and mechanical properties of rotationally moulded LLDPE/graphite composites using natural Zimbabwean graphite, expandable and pre-expanded graphite were investigated. Different processing methods were employed in an attempt to obtain antistatic rotomouldable composites with enhanced thermal conductivities. Dry blending was an effective mixing method for the preparation of rotomoulded antistatic LLDPE/Zimbabwean flake graphite composites. The antistatic ranking was reached at just 5 wt.% graphite. At this addition level the Young's modulus of the composite was similar to that of the neat polymer and the tensile yield strength was 10% lower. However, elongation-at-break and Gardner impact strength were severely compromised. Rotomoulded samples based on pre-compounded Zimbabwean flake graphite at the 10 wt.% level were also rated antistatic. In this case the modulus was slightly higher and the tensile yield strength was 16% lower. The deterioration in the other two mechanical properties was just as severe. The double-dumped Zimbabwean graphite composite only became antistatic at 15 wt.% graphite content. At this level, the modulus was close to that of the neat LLDPE, but the yield and impact strength had deteriorated severely.

The expandable graphite composites are of particular interest as good fire retardant properties can be achieved at loadings upward of 10 wt.%. At these levels the rotomoulded samples based on pre-compounded powders are also antistatic. Unfortunately these composites show similarly poor elongation-at-break and Gardner impact values.

The dry-blend expanded graphite-based composites also exhibited lower resistivity values than the corresponding compounded samples, similar to the natural flake graphite. They were more conductive than the composites based on expandable graphite and achieved the static dissipative rating at 8 and 10 wt.% graphite respectively. However, they also exhibited poor mechanical properties.

Injection-moulded versions of all these compositions featured acceptable mechanical properties, but they were not antistatic. The Halpin-Tsai model provided good fits to the experimental tensile modulus data of injection-moulded Zimbabwean and expandable graphite. These fits affirmed the anisotropic nature of the graphite fillers in the composites.

DSC results showed that the graphite fillers nucleate crystallisation, inducing higher crystallisation temperatures of the composites. The TGA of the composites suggests that the presence of the graphite in the polyethylene matrix does not affect degradation of polyethylene as mass losses for all the composites commence at about 400 °C.

Dry blending was also found to be an effective method of rotomoulding polyethylene/graphite composites with enhanced thermal conductivity. Dry-blended expanded graphite composites exhibited the best overall thermal conductivity with an 88% improvement at a graphite content of 20 wt.%. An interesting observation was that the dry-blended composites also exhibited low electrical resistivity and hence good antistatic performance. Melt-compounded rotomoulded composites exhibited poor thermal conductivity values due to higher porosities in the mouldings.

The improvement in the thermal conductivities of injection-moulded LLDPE/graphite composites with an increase in graphite content was predominantly better than that of rotomoulded composites. However, the conductivity values for injection-moulded composites at 10 wt.% are comparable to those of dry-blended composites at the same loading.

The geometric mean model fits the thermal conductivity data well at low volume fractions of graphite fillers for both rotomoulded and injection-moulded composites. The Lewis-Nielsen model was effectively fit as the Halpin-Tsai model to the thermal conductivity data. Fittings of the model to the thermal conductivity data of the injection-moulded composites show that the thermal conductivity shape factors used for Zimbabwean and expandable graphite are more than twice those of the tensile modulus. Based on these observations, the shape factors used for the tensile modulus are not adequate for the thermal conductivity data. The Lewis-Nielsen model was also fit to the thermal conductivity data of the injection-moulded composites using the maximum volumetric packing fractions, unlike in the Halpin-Tsai model. In this case the Lewis-Nielsen model yielded smaller shape factors, compared to when it was used without the maximum packing fractions as the Halpin-Tsai model. The shape factors obtained from the fits for the thermal conductivity data of rotomoulded composites were smaller compared to the shape factors for injection-moulded composites.

Since it has been established which graphite form, composition and mixing method gives adequate antistatic performance, it is recommended that further work be done to improve the mechanical properties of rotomoulded graphite polyethylene composites. This could be achieved through compatibilisation of the graphite and polyethylene and reduction of the viscosity of the melts. Silane coupling agents, maleic anhydride grafted polyethylene or polyethylene-co-acrylic acid are suggested as compatibilisers between graphite and polyethylene. However, there is a potential problem of the resin adhering to the mould wall. The viscosity of the melts could be reduced by using low molecular weight additives, thereby enhancing the sintering behaviour of the polyethylene. Also, flame retardancy tests need to be carried out to verify the effectiveness of the graphite in the composites.

REFERENCES

- Abdullah, M.Z., Bickerton, S., Bhattacharyya, D., Crawford, R.J. and Harkin-Jones, E. (2009). Rotational molding cycle time reduction using a combination of physical techniques. *Polym. Eng. Sci.*, **49**: 1846–1854.
- Agari, Y. and Uno, T. (1986). Estimation on thermal conductivities of filled polymers. *J. Appl. Polym. Sci.*, **32**: 5705–5712.
- Agari, Y., Ueda, A. and Nagai, S. (1991). Thermal conductivities of composites in several types of dispersion systems. *J. Appl. Polym. Sci.*, **42**: 1665–1669.
- Agari, Y., Ueda, A. and Nagai, S. (1993). Thermal conductivity of a polymer composite. *J. Appl. Polym. Sci.*, **49**: 1625–1634.
- Ahmed, S. and Jones F. R. (1990). A review of particulate reinforcement theories for polymer composites. *J. Mater. Sci.*, **25**: 4933–4942.
- Akinci, A. (2009). Mechanical and structural properties of polypropylene composites filled with graphite flakes. *Arch. Mater. Sci. Eng.*, **35**(2): 91–94.
- Ameen, S., Akhtar, M.S. and Husain, M. (2010). A review on synthesis processing, chemical and conduction properties of polyaniline and its nanocomposites. *Sci. Adv. Mater.*, **2**: 441–462.
- An, Q., Qi, S. and Zhou, W. (2009) Thermal, electrical, and mechanical properties of Si₃N₄ filled LLDPE composite. *Polym. Compos.*, **30**(7): 866–871.
- Angelico, D.F. (2011). Electrically conductive confined space ventilator conduit formed of conductive polymer, electrical grounding circuit for ventilation system using same, and methods of using and forming same. US Patent 7 992 593 B2.
- Ansari, R. and Keivani, M.B. (2006). Polyaniline conducting electroactive polymers: Thermal and environmental stability studies. *E. J. Chem.*, **3**(13): 202-217.
- Asbury Carbons. (2011). Introduction to graphite: Structural description. Available at: <http://www.asbury.com/Structural-Description.html> (accessed on 12 August 2011)
- Beall, G.L. (1998). *Rotational Molding, Design, Materials, Tooling and Processing*. Hanser Publishers, Munich, Germany.
- Bellehumeur, C.T. (2005). Rotational molding of polymers. In: Sunggyu, E. (Ed.), *Encyclopedia of Chemical Processing*, Taylor & Francis, New York.
- Bhadra, S., Khastagir, D., Singha, N.K. and Lee, H.J. (2009). Progress in preparation, processing and applications of polyaniline. *Prog. Polym. Sci.*, **34**: 783–810.
- Bhattacharya, S., Tandon, R.P. and Sachdev, V.K. (2009). Electrical conduction of graphite filled high density polyethylene composites; experiment and theory. *J. Mater. Sci.*, **44**:

2430–2433.

- Bigg, D.M. (1995). Thermal conductivity of heterophase polymer composites. *Adv. Polym. Sci.*, **119**: 1–30.
- Bigg, D.M. (1979). Mechanical, thermal, and electrical properties of metal fiber-filled polymer composites. *Polym. Eng. Sci.*, 19(16), 1188–1192.
- Britton, L.G. (1999). *Avoiding Static Ignition Hazards in Chemical Operations*. American Institute of Chemical Engineers, New York.
- Brown, G.M. and Ellyin, F. (2005). Assessing the predictive capability of two-phase models for the mechanical behavior of alumina/epoxy nanocomposites. *J. Appl. Polym. Sci.*, **98**: 869–879.
- Burchel, T.D. (2001). Thermal properties and nuclear applications. In: Delhaès, P. (Ed.), *Graphite and Precursors*, Gordon and Breach Science Publishers, Amsterdam, Netherlands.
- Campbell, R.W. and Tan, W. (1995). Use of static-safe polymers in automated handling equipment. *Proceedings, Electrical Overstress/Electrostatic Discharge Symposium*, Bordeaux, France, 12–14 Sept., pp 95–218.
- Carter, S. (2010). Electrostatic discharge (ESD) properties of plastic packaging: Terminology, standards, and measurement. *Tek Pak Technical Bulletin*, **101**, 1–5.
- Castle, G.S.P. (2001). Industrial applications of electrostatics: The past, present and future. *J. Electrostat.*, **5152**: 1–7.
- Castle, G.S.P. and Incullet, I.I. (1997). The electrostatic fields and discharge hazards of insulating sheets close to a conductor: A review. *IEEE Trans. Ind. Appl.*, **33**(1): 274–278.
- Chaudhary, B.I., Takács, E. and Vlachopoulos, J. (2001). Processing enhancers for rotational molding of polyethylene. *Polym. Eng. Sci.*, **41**(10): 1731–1742.
- Chen, C., Wang, L. and Hong, J. (2010). Graphite nanosheets act as conducting filler for high-density polyethylene. Society of Plastics Engineers, Plastics Research Available at: <http://www.4spepro.org/view.php?source=003007-2010-06-12> (accessed on 28 October 2010).
- Chen, G., Wu, D., Weng, W., He, B. and Yan, W. (2001). Preparation of polystyrene-graphite conducting nanocomposites via intercalation polymerization. *Polym. Int.*, **50**: 980–985.
- Chen, G., Weng, W., Wu, D. and Wu, C. (2003a). PMMA/graphite nanosheets composite and its conducting properties. *Eur. Polym. J.*, **39**: 2329–2335.

- Chen, G., Wu, C., Weng, W., Wu, D. and Yan, W. (2003b). Preparation of polystyrene/graphite nanosheet composite. *Polymer*, **44**, 1781–1784.
- Chen, G., Weng, W., Wu, D., Wu, C., Lu, J., Wang, P. and Chen, X. (2004) Preparation and characterization of graphite nanosheets from ultrasonic powdering technique. *Carbon*, **42**: 753–759.
- Chen, G., Chen, X., Wang, H. and Wu, D. (2007). Dispersion of graphite nanosheets in polymer resins via masterbatch technique. *J. Appl. Polym. Sci.*, **103**: 3470–3475.
- Chen, X., Shen, J. and Huang, W. (2002). Novel electrically conductive polypropylene/graphite nanocomposites. *J. Mater. Sci. Lett.*, **21**: 213–214.
- Cheng, S.C. and Vachon, R.I. (1969). The prediction of the thermal conductivity of two and three phase solid heterogeneous mixtures. *Int. J. Heat Mass Transfer*, **12**: 249–264.
- Chipara, M., Hui, D., Notingher, P.V., Chipara, M.D., Lau, K.T., Sankar, J. and Panaitescu, D. (2003). On polyethylene-polyaniline composites. *Composites Part B*, **34**: 637–645.
- Cho, J., Luo, J.J. and Daniel, I.M. (2007). Mechanical characterization of graphite/epoxy nanocomposites by multi-scale analysis. *Compos. Sci. Technol.*, **67**: 2399–2407.
- Chubb, J. (1999). Measurement of tribo and corona charging features of materials for assessment of risks from static electricity. *IEEE Trans. Ind. Appl.*, **36**(6): 1515–1522.
- Chung, D.D.L. (1987). Review: Exfoliation of graphite. *J. Mater. Sci.*, **22**: 4190–4198.
- Chung, D.D.L. (2002). Review: Graphite. *J. Mater. Sci.*, **37**: 1475–1489.
- Clingerman, M.I., King, J.A., Schulz, K.H. and Meyers, J.D. (2000). Evaluation of electrical conductivity models for conductive polymer composites. *J. Appl. Polym. Sci.*, **83**: 1341–1356.
- Cote, M., Corté, M.T., Beltrán, D. and Ortiz, P. (2009). PANI-LDPE composites: Effect of blending conditions. *Polym. Compos.*, **30**: 22–29.
- Cramez, M.C., Oliveira, M.J. and Crawford, R.J. (2002). Optimisation of rotational moulding of polyethylene by predicting antioxidant consumption. *Polym. Degrad. Stab.*, **75**: 321–327.
- Crawford, R.J. (1996). Recent advances in the manufacture of plastic products by rotomoulding. *J. Mater. Process. Technol.*, **56**: 263–271.
- Crawford, R.J. and Gibson, S. (2006). Rotational molding: The basics for designers. *Rotoworld*, March–April: 60–66.
- Crawford, R.J. and Throne, J.L. (2002). *Rotational Molding Technology*. Plastics Design Library/William Andrew Publishing, New York.

- Dahman, S.J. (2003). All polymeric compounds: Conductive and dissipative polymers in ESD control materials. *Proceedings, Electrical Overstress/Electrostatic Discharge Symposium*, Bordeaux, France, 12–14 Sept.
- DeArmitt, C. and Hancock, M. (2003). In: Rothon, R.N. (Ed.), *Particulate-filled Polymer Composites*, Rapra Technology Ltd, Shrewsbury, UK.
- Debelak, B. and Lafdi, K. (2007). Use of exfoliated graphite filler to enhance polymer physical properties. *Carbon*, **45**: 1727–1734.
- Dong, H., Fan, L. and Wong, C.P. (2005). Effect of interface on thermal conductivity of polymer composite. *Proceedings, 55th Electronic Components and Technology Conference*, Lake Buena Vista, FL, US, 31 May – 3 June.
- Dresselhaus, M.S. and Dresselhaus, G. (2002). Intercalation compounds of graphite. *Adv. Phys.*, **51**(1): 1–186.
- Duquesne, S., Le Bras, M., Bourbigot, S., Delobel, R., Vezin, H., Camino, G., Eling, B., Lindsay, C. and Roels, T. (2003). Expandable graphite: A fire retardant additive for polyurethane coatings. *Fire Mater.*, **27**: 103–117.
- ESD Association (2010). Fundamentals of electrostatic discharge. Part 1: An introduction to ESD. Available at: <http://www.esda.org/documents/FundamentalsPart1.pdf> (Accessed on 10 October 2010).
- Farshidfar, A., Asl, V.H. and Nazokdast, H. (2006). Electrical and mechanical properties of conductive carbon black/polyolefin composites mixed with carbon fiber. COMPOSITES 2006 Convention and Trade Show. Available at: <http://www.acmanet.org/resources/06papers/Farshidfar105.pdf> (accessed on 7 November 2010)
- Fim, F.C., Guterres, J.M., Basso, N.R.S. and Galland, G.B. (2010). Polyethylene/graphite nanocomposites obtained by in situ polymerization. *J. Polym. Sci., Part A: Polym. Chem.*, **48**: 692–698.
- Focke, W.W., Molefe, D., Labuschagne, F.J.W. and Ramjee, S. (2009). The influence of stearic acid coating on the properties of magnesium hydroxide, hydromagnesite, and hydrotalcite powders. *J. Mater. Sci.*, **44**: 61006109.
- Fornes, T.D. and Paul, D.R. (2003). Modeling properties of nylon 6/clay nanocomposites using composite theories. *Polymer*, **44**: 4993–5013.
- Fowler, S.L. (1988). Triboelectricity and surface resistivity do not correlate. *Proceedings, Electrical Overstress/Electrical Discharge Symposium*, New Orleans, Louisiana, US, 26–28 September.
- Fu, S. and Mai, Y. (2003). Thermal conductivity of misaligned short-fiber reinforced polymer composites. *J. Appl. Polym. Sci.*, **88**: 14971505.

- Fu, S., Feng, X., Lauke, B. and Mai, Y. (2008). Effects of particle size, particle/matrix interface adhesion and particle loading on mechanical properties of particulate–polymer composites. *Composites, Part B*, **39**: 933–961.
- Gaxiola, D.L., Jubinski, M.M., Keith, J.M., King, J.A. and Miskioglu, I. (2010). Effects of carbon fillers on tensile and flexural properties in polypropylene-based resins. *J. Appl. Polym. Sci.*, **118**: 1620–1633.
- George, J.J. and Bhowmick, A.K. (2008). Ethylene vinyl acetate/expanded graphite nanocomposites by solution intercalation: Preparation, characterization and properties. *J. Mater Sci.*, **43**: 702708.
- Gibson, N. (1997). Static electricity-an industrial hazard under control? *J. Electrostat.*, **40 & 41**: 21–30.
- Glor, M. (1981). Ignition of gas/air mixtures by discharges between electrostatically charged plastic surfaces and metallic electrodes. *J. Electrostat.*, **10**: 327–332.
- Grasso, T., Gutman, G. and Yenni, D.M. (1985). Triboelectric charging propensity of packaging materials packaging materials. *Proceedings, Nepcon West Conference*, Anaheim, CA, US.
- Greason, W.D. (1992). Electrostatic discharge: A charge-driven phenomenon. *J. Electrostat.*, **28**: 199–218.
- Grob, M.C. and Minder, E. (1999). Permanent antistatic additives: New developments. *Plas. Add. & Comp.*, July: 20–26.
- Groop, E.E., Nowicki, A.W., Calle, C.I., Buhler, C.R, and Mantovani, J.G. (2003). Comparison of surface resistivity and triboelectric charge generation characteristics of materials. *Proceedings, 40th Space Congress*. Cape Canaveral, FL, US, 28 April 28 – 1 May.
- Halpin, J.C. and Kardos, J.L. (1976). The Halpin-Tsai Equations: A Review. *Polym. Eng. Sci.*, **16**(5): 344–352.
- Harper, W.R. (1970). Triboelectrification. *Phys. Educ.*, **5**: 87–93
- Hatta, H., Taya, M., Kulacki, F.A. and Harder, J.F. (1992). Thermal diffusivities of composites with various types of filler. *J. Compos. Mater.*, **26**(5): 612–625.
- Hausmann, K. (2007). Permanent antistatic agent offers long term performance for films and containers. *Plas. Add. & Compound.*, May/June: 40–42.
- Hill, R.F. and Supancic, P.H. (2003). Thermal conductivity of platelet-filled polymer composites. *J. Am. Ceram. Soc.*, **85**(4): 851–57.

- Hogue, M.D., Buhler, C.R., Calle, C.I., Matsuyama, T., Luo, W and Groop, E.E. (2004). Insulator-insulator contact charging and its relationship to atmospheric pressure. *J. Electrostat.*, **61**: 259–268.
- Hung, M.T., Choi, O., Ju, Y.S. and Hahn H.T. (2006). Heat conduction in graphite-nanoplatelet-reinforced polymer nanocomposites. *Appl. Phys. Lett.*, **89** (023117): 1–3.
- Irvine D.J. and McCluskey, J.A. and Robinson I.M. (2000). Fire hazards and some common polymers. *Polym. Degrad. Stabil.*, **67**: 383–396.
- Ismail, M.N. and Khalaf, A.I. (2011). Styrene-butadiene rubber/graphite powder composites: Rheometrical, physicomechanical, and morphological properties. *J. Appl. Polym. Sci.*, **120**: 298–304.
- Jennifer, M. (2008). New developments in antistatic and conductivity additives, *Plast. Add. & Compound.*, September/October: 22–25.
- Jian, L., Ning, L., Yang, S., Wang, J. and Hua, M. (2010). Triboelectrification electrostatic potential of graphite/monomer casting nylon composites under dry sliding: Correlation with electrical resistivity and wear mechanisms. *Polym. Compos.*, **31**: 1369–1377.
- Kalaitzidou, K., Fukushima, H. and Drzal, L.T. (2010). A route for polymer nanocomposites with engineered electrical conductivity and percolation threshold. *Materials*, **3**: 1089–1103.
- Kalaitzidou, K., Fukushima, H., and Drzal, L.T. (2007). Multifunctional polypropylene composites produced by incorporation of exfoliated graphite nanoplatelets. *Carbon*, **45**: 14461452.
- Kalyoncu, R.S. and Taylor, H.A. (2005). Graphite, natural. In: Seidel, A. (Ed.), *Kirk-Othmer Encyclopaedia of Chemical Technology*, Wiley, Hoboken, NJ, US.
- Kelly III, G.L. and Jones, K E (2002). Rotation molded particulate collection bottle. US Patent Application Publication, US 2002/0108358 A1.
- Kim, S., Seo, J. and Drzal, L.T. (2010). Improvement of electric conductivity of LLDPE based nanocomposites by paraffin coating on exfoliated graphite nanoplatelets. *Composites, Part A*, **41**: 581–587.
- Kissin, Y.V. (2005). Polyethylene, linear low density (LLDPE). In: Seidel, A. (Ed.), *Kirk-Othmer Encyclopedia of Chemical Technology*, Wiley, Hoboken, NJ, US.
- Kolycheck, E.G., Mertz, E.A. and Sullivan, F.R. (1992). Polyurethane for use in electrostatic dissipating applications. US Patent 5 159 053.
- Kontopoulou, M. and Vlachopoulos, J. (1999). Bubble dissolution in molten polymers and its role in rotational molding. *Polym. Eng. Sci.*, **39**(7): 11891198.

- Krupa, I. and Chodák, I. (2001). Physical properties of thermoplastic/graphite composites. *Eur. Polym. J.*, **37**: 2159–2168.
- Krupa, I., Novák, I., Chodák, I. (2004). Electrically and thermally conductive polyethylene/graphite composites and their mechanical properties. *Synth. Met.*, **145**: 245–252.
- Kumar, P., Sandeep, K.P., Alavi, S., and Truong, V.D. (2011). Review of experimental and modelling techniques to determine properties of biopolymer-based nanocomposites. *J. Food Sci.*, **76**(1): E2-E14.
- Leonard, J.T. (1981). Static electricity in hydrocarbon liquids and fuels. *J. Electrostat.*, **10**: 17–30.
- Liu, S. and Peng, K. (2010). Rotational molding of polycarbonate reinforced polyethylene composites: processing parameters and properties. *Polym. Eng. Sci.*, **50**: 14571465.
- Lüttgens, G. and Wilson N. (1997). *Electrostatic Hazards*. Butterworth-Heinemann, Oxford, UK.
- Lux, F. (1993) Review: Models proposed to explain the electrical conductivity of mixtures made of conductive and insulating materials. *J. Mater. Sci.*, **28**: 285–301.
- Maplestone, P. (2008). Rotational moulding-rotomoulders take control. *Plast. Eng.*, November: 10–16.
- Martin, D., Halley, P., Truss, R., Murphy, M., Jackson, O. and Kwon, O. (2003). Polyethylene-layered silicate nanocomposites for rotational moulding. *Polym. Int.*, **52**: 1774–1779.
- Martins, C.R. and De Paoli, M. (2005). Antistatic thermoplastic blend of polyaniline and polystyrene prepared in a double-screw extruder. *Eur. Polym. J.*, **41**: 2867–2873.
- McCarty, L.S. and Whitesides, G.M. (2010). Electrostatic charging due to separation of ions at interfaces: Contact electrification of ionic electrets. *Angew. Chem. Int. Ed.*, **47**: 2188–2207.
- Móczó, J. and Pukánszky, B. (2008). Polymer micro and nanocomposites: Structure, interactions, properties. *J. Ind. Eng. Chem.*, **14**: 535–563.
- Mulligan, J.C. (2003). Handling flammable liquids. *Chem. Eng. Prog.*, **99**(7): 48–56.
- Murphy, J. (2001). *Additives for Plastics Handbook*. Elsevier Advanced Technology, Oxford, UK.
- Nagata, K., Iwabuki, H. and Nigo, H. (1999). Effect of particle size of graphites on electrical conductivity of graphite/polymer composite. *Compos. Interfaces*, **6**(5): 483–495.
- Narkis, M., Lidor, G., Vaxman, A. and Zuri, L. (1999). New injection moldable electrostatic

- dissipative (ESD) composites based on very low carbon black loadings. *J. Electrostat.*, **47**: 201–214.
- Nielsen, L. E. and Landel, R.F. (1994). *Mechanical Properties of Polymers and Composites*. Marcel Dekker, New York, US.
- Nielsen, L.E. (1974). The thermal and electrical conductivity of two-phase systems. *Ind. Eng. Chem. Fundam.*, **13**: 1720.
- Noel, M. and Santhanam, R. (1998). Electrochemistry of graphite intercalation compounds. *J. Power Sources*, **72**: 53–65.
- Nugay, N., Küsefoğlu, S. and Erman, B. (1997). Swelling and static-dynamic mechanical behavior of mica-reinforced linear and star-branched polybutadiene composites. *J. Appl. Polym. Sci.*, **66**: 1943–1952.
- Omastova, M., Chodak, I. and Pionteck, J. (1999). Electrical and mechanical properties of conducting polymer composites. *Synth. Met.*, **102**: 1251–1252.
- Osman, A.F., Johar, B., Adam, S.N.F.S, Amin, S.A.M. and Osman, A. (2007). The effect of porosity on thermal conductivity of silicon carbide filled polypropylene composite. *Proceedings, 1st International Conference on Sustainable Materials Engineering (ICoSM 2007)*, Penang, Malaysia, 9–11 June.
- Osswald, T.A. (1998). *Polymer Processing Fundamentals*. Hanser Publishers, Munich, Germany.
- Panwar, V. and Mehra, R.A.M. (2008). Analysis of electrical, dielectric, and electromagnetic interference shielding behavior of graphite filled high density polyethylene composites, *Polym. Eng. Sci.*, **48**: 2178–2187.
- Patch, R. (2001). Conductive plastic container for volatile liquids. US Patent 6 283 320 B1.
- Patel, P., Hull ,T.R., Stec, A.A. and Lyon, R.E. (2011). Influence of physical properties on polymer flammability in the cone calorimeter. *Polym. Adv. Technol.*, **22**: 1100–1107.
- Pavey, I. D. (2004). Electrostatic hazards in the process industries. *Process Saf. Environ. Prot.*, **82**(B2): 132–141.
- Pethrick, R.A. and Hudson, N.E. (2008). Rotational moulding – a simplified theory. *P. I. Mech. Eng. L-J. Mat.*, **222**: 151–158.
- Picken, S.J., Korobko, A.V., Mendes, E., Norder, B., Makarova, V.V., Vasilyev, G.B., Karbushev, V.V. and Tolstykh, M.Y. (2011). Mechanical and thermal properties of polymer micro- and nanocomposites. *J. Polym. Eng.*, **31**: 269–273.
- Pierson, H.O. (1993). *Handbook of Carbon, Graphite, Diamond and Fullerenes - Properties, Processing and Applications*. William Andrew Publishing/Noyes, Park Ridge, NJ, US.

- Pikington, G.A. (1994). Static electricity – friend or foe? Proceedings, 5th International Conference on Electrical Safety in Hazardous Environments, Institution of Electrical Engineers, London, UK, 19–21 April, pp 63–68.
- Pionteck, J. (2007). Introduction. In: Pionteck, J. and Wypych, G. (Eds), *Handbook of Antistatics*, ChemTec Publishing, Toronto, Canada.
- Planes, E., Duchet, J., Maazouz, A. and Gerard, J. (2008). Characterization of new formulations for rotational molding based on ethylene-propylene copolymer/graphite nanocomposites. *Polym. Eng. Sci.*, **48**: 723–731.
- Pötschke, P., Abdel-Goad, M., Pegel, S., Jehnichen, D., Mark, J.E., Zhou, D. and Heinrich, G. (2010). Comparisons among electrical and rheological properties of melt-mixed composites containing various carbon nanostructures. *J. Macromol. Sci., Part A, Pure Appl. Chem.*, **47**: 12–19.
- Progelhof, R.C., Throne, J.L. and Ruetsch, R.R. (1976). Methods for predicting the thermal conductivity of composite systems: A review. *Polym. Eng. Sci.*, **16**(9): 615–625.
- Pukánszky B. and Fekete, E. (1999). Adhesion and surface modification. *Adv. Polym. Sci.*, **139**: 109–153.
- Quan, H., Zhang, B., Zhao, Q., Yuen R.K.K. and Li, R.K.Y. (2009). Facile preparation and thermal degradation studies of graphite nanoplatelets (GNPs) filled thermoplastic polyurethane (TPU) nanocomposites. *Composites, Part A*, **40**: 1506–1513.
- Rao, Y. (2007). Gelatine-clay nanocomposites of improved properties. *Polymer*, **48**: 5369–5375.
- Robert, A., Orr, J.F. and Crawford, R.J. (2000). Influence of mica and talc fillers on the properties of rotationally moulded LLDPE. *Proceedings, ANTEC 2000 Conference, Plastics: The Magical Solution*, Vol. 1: Processing, Orlando, FL, US, 7–11 May.
- Robert, A. and Crawford, R.J. (1999). The Effect of fillers on the properties of rotationally molded polyethylene. *Proceedings, ANTEC 1999, Plastics: Bridging the Millennia*, Vol. 1: Processing, New York City, US, 2–6 May.
- Rosato, D.V. (2007). Emerging tech: Inherently conducting polymers. *Rotational Moulding Newsletter*, **7**(2): 6–8.
- Rosner, R.B. (2001). Conductive materials for ESD applications: An overview. *IEEE Trans., Device Mater. Reliab.*, **1**(1): 9–16.
- Sae-Chien, W. and Kanokboriboon, A. (2007). An investigation on the effects of fine-particulate filler on the properties of a rotomolding-grade polyethylene. *Proceedings, ANTEC 2007, Plastics: Annual Technical Conference*, Cincinnati, OH, US, 6–11 May, pp 2742–2748.

- Sengupta, R., Bhattacharya, M., Bandyopadhyay, S. and Bhowmick, A.K. (2011). A review on the mechanical and electrical properties of graphite and modified graphite reinforced polymer composites. *Prog. Polym. Sci.*, **36**: 638–670.
- Sharma, T., Mahanwar, P.A. and Bambole, V. (2009). Study of modified polypropylene for rotational moulding applications. *Int. J. Plast. Technol.*, **13**(1): 83–94.
- She Y., Chen, G. and Wu, D. (2007) Fabrication of polyethylene/graphite nanocomposite from modified expanded graphite. *Polym. Int.*, **56**: 679–685.
- Shen, J., Huang, W., Zuo, S. and Hou, J. (2005). Polyethylene/grafted polyethylene/graphite nanocomposites: Preparation, structure, and electrical properties. *J. Appl. Polym. Sci.*, **97**: 51–59.
- Spence, A.G. and Crawford, R.J. (1996). The effect of processing variables on the formation and removal of bubbles in rotationally molded products. *Polym. Eng. Sci.*, **36**: 993–1009.
- Struèmler, R. and Glatz-Reichenbach, J. (1999). Conducting polymer composites *J. Electroceram.*, **3**(4): 329–346.
- Sumirat, I., Ando, Y. and Shimamura, S. (2006). Theoretical consideration of the effect of porosity on thermal conductivity of porous materials. *J. Porous Mater.*, **13**: 439–443.
- Takai, T., Kaneko, M. and Honda, M. (1998). One of the methods of observing ESD around electronic equipment. *J. Electrostat.*, **42**: 305–320.
- Tavman, I.H. (1998). Effective thermal conductivity of isotropic polymer composites. *Int. Comm. Heat Mass Transfer*, **25**(5): 723–732.
- Tekce, H.S., Kumlutas, D. and Tavman, I.H. (2007) Effect of particle shape on thermal conductivity of copper reinforced polymer composites. *J. Reinf. Plast. Compos.*, **26**(1): 113–121.
- Thongraung, W., Spontack, R.J. and Balik, C.M. (2002a). Correlated electrical conductivity and mechanical property analysis of high-density polyethylene filled with graphite and carbon fibre. *Polymer*, **43**: 2279–2286.
- Thongraung, W., Balik, C.M. and Spontack, R.J. (2002b). Volume-exclusion effects in polyethylene blends filled with carbon black, graphite, or carbon fiber. *J. Polym. Sci., Part B: Polym. Phys.*, **40**: 1013–1023.
- Torres, F.G. and Aragon, C.L. (2006). Final product testing of rotational moulded natural fibre-reinforced polyethylene. *Polym. Test.*, **25**: 568–577.
- Tucker III, C.L. and Liang, E. (1999). Stiffness predictions for unidirectional short-fiber composites: Review and evaluation. *Comp. Sci. Technol.*, **59**: 655–671.

- Uhl, F.M., Yao, Q., Nakajima H., Manias, E. and Wilkie, C.A. (2005a). Expandable graphite/polyamide-6 nanocomposites. *Polym. Degrad. Stabil.*, **89**: 7084.
- Van Es, M.A. (2001) Polymer-clay nanocomposites, the importance of particle dimensions. PhD thesis, Delft University of Technology, Delft, Netherlands.
- Verbeek, C.J.R. (2001). The Young's modulus of compression moulded LLDPE/phlogopite composites. PhD thesis, University of Pretoria, Pretoria, South Africa.
- Verbeek, C.J.R. and Focke, W.W. (2002). Modelling the Young's modulus of platelet reinforced thermoplastic sheet composites. *Composites, Part A*, **33**: 1697–1704.
- Wang, L. and Chen, G. (2010). Dramatic improvement in mechanical properties of GNs-reinforced HDPE nanocomposites. *J. Appl. Polym. Sci.*, **116**: 2029–2034.
- Wang, Q., Gao, J., Wang, R. and Hua, Z. (2001). Mechanical and rheological properties of HDPE/graphite composite with enhanced thermal conductivity. *Polym. Compos.*, **22**(1): 97–103.
- Wang, W., Liu, Y., Li, X. and You, Y. (2006). Synthesis and characteristics of poly(methyl methacrylate)/expanded graphite nanocomposites. *J. Appl. Polym. Sci.*, **100**: 1427–1431.
- Ward, I.M. and Sweeny, J. (2004). *An Introduction to the Mechanical Properties of Solid Polymers*. Wiley, Chichester, UK.
- Weber, E.H., Clingerman, M.L. and King, J.A. (2003a). Thermally conductive nylon 6,6 and polycarbonate based resins. II. Modeling. *J. Appl. Polym. Sci.*, **88**: 123–130.
- Weber, E.H., Clingerman, M.L. and King, J.A. (2003b). Thermally conductive nylon 6,6 and polycarbonate based resins. I. Synergistic effects of carbon fillers. *J. Appl. Polym. Sci.*, **88**: 112–122.
- Wesley, B.G. (1999). The rotational molding of glass fibre reinforced polyethylene. *Proceedings, ANTEC 1999, Plastics: Bridging the Millennia*, Vol. 1: Processing, New York City, US, 2–6 May.
- Whiteley, R.H (1993). Some comments on the measurement of ignitability and on the calculation of 'Critical heat flux'. *Fire Safety J.*, **21**: 177–83.
- Wissler, M. (2006). Graphite and carbon powders for electrochemical applications. *J. Power Sources*, **156**: 142–1503.
- Wu, Y., Jia Q., Yu, D. and Zhang, L. (2004). Modeling Young's modulus of rubber-clay nanocomposites using composite theories. *Polym. Test.*, **23**: 903–909.
- Wycisk, R., Poźniak, R. and Pasternak, A. (2002). Conductive polymer materials with low filler content. *J. Electrostat.*, **56**: 55–66.

- Xanthos, M. (2005). Polymers and Polymer Composites. In: Xanthos, M. (Ed.), *Functional Fillers for Plastics*, Wiley-VCH Verlag, Weinheim, Germany.
- Xiao, M., Sun, L., Liu, J., Li, Y. and Gong, K. (2002). Synthesis and properties of polystyrene/graphite nanocomposites. *Polymer*, **43**: 2245–2248.
- Xie, R. and Qu, B. (2001). Synergistic effects of expandable graphite with some halogen-free flame retardants in polyolefin blends. *Polym. Degrad. Stabil.*; **71**: 375–380.
- Yan, W., Tin, R.J.T. and Bhattacharyya, D. (2006). Particulate reinforced rotationally moulded polyethylene composites. Mixing methods and mechanical properties. *Compos. Sci. Technol.*, **66**: 2080–2088.
- Yang, J., Tian, M., Jia, Q., Zhang, L. and Li, X. (2006). Influence of graphite particle size and shape on the properties of NBR. *J. Appl. Polym. Sci.*, **102**: 4007–4015.
- Yasmin, A., Luo, J. and Daniel, I.M. (2006). Processing of expanded graphite reinforced polymer nanocomposites. *Compos. Sci. Technol.*, **66**: 1182–1189.
- Yasmin, A. and Daniel, I.M. (2004). Mechanical and thermal properties of graphite platelet/epoxy composites. *Polymer*, **45**: 8211–8219.
- Ye, C., Shentu, B. and Weng, Z. (2006). Thermal conductivity of high density polyethylene filled with graphite. *J. Appl. Polym. Sci.*, **101**: 3806–3810.
- Young, R.J. and Lovell, P.A. (1991). *Introduction to Polymers*. CRC Press, New York, US.
- Yu, H. (1990). Ethylene oxide-epihalohydrin copolymer antistatic additive for chlorine-containing polymers. US Patent 4 931 506.
- Yuan, X., Eastal, A.J. and Bhattacharyya, D. (2008). Influence of surface treatment on hybrid wollastonite-polyethylene composite resins for rotational moulding. *J. Mater. Sci.*, **43**: 6057–6063.
- Zeng, Y., Liu, P., Du, J., Zhao, L., Ajayan, P.M. and Cheng, H. (2010). Increasing the electrical conductivity of carbon nanotube/polymer composites by using weak nanotubes-polymer interactions. *Carbon*, **48**: 3551–3558.
- Zhang, L.M. and Dai, G.C. (2007). Effect of interfacial treatment on the thermal properties of thermal conductive plastics. *Express Polym Lett.*, **1**(9): 608–615.
- Zheng, W., Lu, X. and Wong, S. (2004). Electrical and mechanical properties of expanded graphite-reinforced high-density polyethylene. *J. Appl. Polym. Sci.*, **91**: 2781–2788.

APPENDICES

Appendix A: Rotomoulding charge weights

The composite density was determined using Equation A-1 as follows

$$\frac{1}{\rho_{composite}} = \frac{W_g}{\rho_g} + \frac{W_{PE}}{\rho_{PE}} \quad (A-1)$$

Using the composite density and a fixed charge volume (ca. 320 cm³), the charge mass of each composition was determined using Equation A-2:

$$m_{composite} = \rho_{composite} \times V_{composite} \quad (A-2)$$

where

ρ_g is the density of graphite (g/cm³)

ρ_{PE} is the density of LLDPE (g/cm³)

$\rho_{composite}$ is the density of the composite (g/cm³)

$W_{graphite}$ is the weight fraction of graphite in the composite

W_{LLDPE} is the weight fraction of LLDPE in the composite

$V_{composite}$ is the volume of the composite (fixed at 319.489 cm³)

$m_{composite}$ is the mass of the composite (g)

$m_{graphite}$ is the mass of graphite (g)

m_{LLDPE} is the mass of LLDPE (g)

m_{OroxPK} is the mass of OroxPK (g)

The actual weights of the graphite and LLDPE corresponding to the particular weight fractions for each composition was then determined as fractions of the composite mass. These are shown in Tables A-1 to A-3.

Table A-1 Rotomoulding charge weights: Zimbabwean graphite composites

Graphite (wt.%)	W _{graphite}	W _{LLDPE}	$\rho_{\text{composite}}$ (g/cm ³)	Charge weight			
				m _{composite} (g)	m _{graphite} (g)	m _{LLDPE} (g)	m _{OroxPK, 1 wt.% on LLDPE} (g)
0	0.00	1.00	0.939	300.00	0.00	300.00	3.00
5	0.05	0.95	0.968	309.25	15.46	293.79	2.94
10	0.10	0.90	0.999	319.09	31.91	287.18	2.87
15	0.15	0.85	1.032	329.57	49.44	280.14	2.80
20	0.20	0.80	1.067	340.77	68.15	272.62	2.73
25	0.25	0.75	1.104	352.75	88.19	264.57	2.65

Table A-2 Rotomoulding charge weights: Expandable graphite (ES 170 300A) composites

Graphite (wt.%)	W _{graphite}	W _{LLDPE}	$\rho_{\text{composite}}$ (g/cm ³)	Charge weight			
				m _{composite} (g)	m _{graphite} (g)	m _{LLDPE} (g)	m _{OroxPK, 1 wt.% on LLDPE} (g)
0	0.00	1.00	0.939	300.00	0.00	300.00	3.00
5	0.05	0.95	0.967	308.95	15.45	293.50	2.94
10	0.10	0.90	0.997	318.45	31.84	286.60	2.87
15	0.15	0.85	1.028	328.55	49.28	279.27	2.79
20	0.20	0.80	1.062	339.31	67.86	271.45	2.71

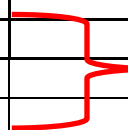
Table A-3 Rotomoulding charge weights: Expanded graphite (ES 250 B5) composites

Graphite (wt.%)	W _{graphite}	W _{LLDPE}	$\rho_{\text{composite}}$ (g/cm ³)	Charge weight			
				m _{composite} (g)	m _{graphite} (g)	m _{LLDPE} (g)	m _{OroxPK, 1 wt.% on LLDPE} (g)
0	0.00	1.00	0.939	300.00	0.00	300.00	3.00
2	0.02	0.98	0.931	297.51	5.95	291.56	2.92
5	0.05	0.95	0.920	293.85	14.69	279.16	2.79
8	0.08	0.92	0.909	290.28	23.22	267.06	2.67
10	0.10	0.90	0.901	287.95	28.80	259.16	2.59
15	0.15	0.85	0.884	282.28	42.34	239.94	2.40
20	0.20	0.80	0.866	276.83	55.37	221.47	2.21

Appendix B: Berstorff compounding data

Table B-1 Berstorff compounding data

Co- rotating, intermeshing, Bestorff 1987, EQ0035187			
Compounding data			D 40mm
Machine	Bestorff		
Screw design		STD NS	DIE HEAD: 1 HOLE
Feed rate powder		25 kg/h	
Extruder parameter		Setting	Reading
RPM		160	160
AMPS		-	25-30
PRESSURE (bars)		-	5
ZONE (°C) 1 (Hopper)		-	17
ZONE (°C) 2		220	175
ZONE (°C) 3		225	220
ZONE (°C) 4		230	225
ZONE (°C) 5		230	214
ZONE (°C) 6		230	234
ZONE (°C) 7		230	235
ZONE (°C) 8		230	233
ZONE (°C) 9 (Die)		235	235
MELT TEMP 10		-	-
BATH TEMP 1		-	-
BATH TEMP 2		-	-
BATH TEMP 3		-	-
PELLETS		-	-
HAUL M/MIN		40	40


**Chilled
in water
bath**

Appendix C: Injection moulding data

Table C-1 ASTM drop impact test mould injection moulding conditions

Injection moulding data			
Machine name	Engel EC885		
Date	28/01/2011	Operator	Washington
Job no	10082403		
Material	(LLDPE/graphite composites). Pellets		
Mould	ASTM drop impact		
Temperature		Set point (°C)	Indicated (°C)
	Barrel 1	200	200
	Barrel 2	220	221
	Barrel 3	230	230
	Melt (Nozzle)	230	221
	Mould	-	RT
Injection time	10	s	
Injection speed	5	mm/s	
Injection pressure	180	bar	
Hold on pressure	50	bar	
Back pressure	10	bar	
Screw speed	50	%	
Cooling time	25	s	
Comments			
Stroke	21 mm		
Clamping force	350 kN		
Cyclic time	42.14 s		
Screw diameter	40 mm		
Remarks			
Runs with ease, ran fully automatic			
Moulding at low injection speeds			
Visible flow lines and graphite particles on the surface of the mouldings (15, 20, 25 wt.%)			

Table C-2 ASTM Tensile test mould injection moulding conditions

Injection moulding data			
Machine name	Engel EC885		
Date	24/08/2010	Operator	Washington
Job no	10082403		
Material	(LLDPE/graphite composites). Powder.		
Mould	ASTM tensile test		
Temperature		Set point (°C)	Indicated (°C)
	Barrel 1	220	220
	Barrel 2	225	224
	Barrel 3	230	230
	Melt (nozzle)	230	232
	Mould	-	RT
Injection time	10	s	
Injection speed	20	mm/s	
Injection pressure	180	bar	
Hold on pressure	75	bar	
Back pressure	10	bar	
Screw speed	50	%	
Cooling time	25	s	
Comments			
Stroke	22 mm		
Clamping force	350 kN		
Cyclic time			
Screw diameter	40 mm		
Remarks			
Mould with ease			
Mouldings stuck to the moving mould part (20 & 25%)			
Total moulding time: 8 hours			

Appendix D: Falling weight (Gardner Impact) impact resistance test calculations

Table D-7 Calculation of the impact resistance of 5 wt.% Zimbabwe graphite, compounded, rotomoulded

Total dart height, mm	Outcome of test (X = failure; O = non-failure)																				n_x	n_o	i	n_i	in_i	i^2n_i
	1	2	3	4	5	6	7	8	9	10	11	12	13	14	15	16	17	18	19	20						
150	X		X		X																3	0	4	0	0	0
125		O		O		X															1	2	3	2	6	18
100							X		X				X		X		X		X		6	0	2	0	0	0
75								O		X		O		O		O		O		O	1	6	1	6	6	6
50											O										0	1	0	1	0	0
Totals																				11	9		9	12	24	
																				(N_x)	(N_o)		(N)	(A)	(B)	

N = total number of failure or non-failures, **whichever is smaller**. For ease of notation, call whichever are used events

$$h = h_o + d_h (A/N \pm 0.5)$$

h = mean-failure height, mm

d_h = increment in height, mm

N = total number of failure or non failures, **whichever is smaller**. For ease of notation, call whichever are used events

h_o = lowest height at which an event occurred, mm

$i = 0, 1, 2, \dots, k$ (counting index, starts at h_o or w_o)

n_i = number of events that occurred at h_i or w_i

$$h_i = h_o + i d_h$$

$$A = \sum_{i=0}^k i n_i$$

$$h_o = 50 \text{ mm}$$

$$D = 25 \text{ mm}$$

$$N = 8$$

$$\mathbf{h = 100.0 \text{ mm} \quad \text{Mean failure height}}$$

MFE = mean failure energy , J

h = mean failure height, mm

w constant mass, kg

f = factor for conversion to Joules

$$f = 0.00980665$$

$$MFE = h w f$$

$$\mathbf{MFE = 0.883 \text{ J}}$$

Estimated standard deviation of the sample

s_h = estimated standard deviation, height, mm

$$s_h = 1.62 d_h [B/N - (A/N)^2] + 0.047 d_h$$

$$B = \sum_{i=0}^k i^2 n_i$$

$$B = 24$$

$$[B/N - (A/N)^2] = 1$$

$$\mathbf{s_h = 37.2 \text{ mm}}$$

Estimated standard deviation of the sample mean

$$s_h^- = G s_h / \sqrt{N}$$

s_h^- = estimated standard deviation of the mean height, mm

G= factor that is a function of s/d, **from Table X1.2 (ASTM D5420-10)**

$$s = 37.2 \text{ mm}$$

$$s/d = 1.49$$

$$\mathbf{G} = 0.96$$

$$s_h^- = \mathbf{11.83}$$

Estimated standard deviation of the mean failure energy

$$S_{MFE} = s_h^- w f$$

where

S_{MFE} = estimated deviation of the mean failure energy

$$\mathbf{S_{MFE} = 0.104 \text{ J}}$$

Appendix E: Photomicrographs of double-dumped composites

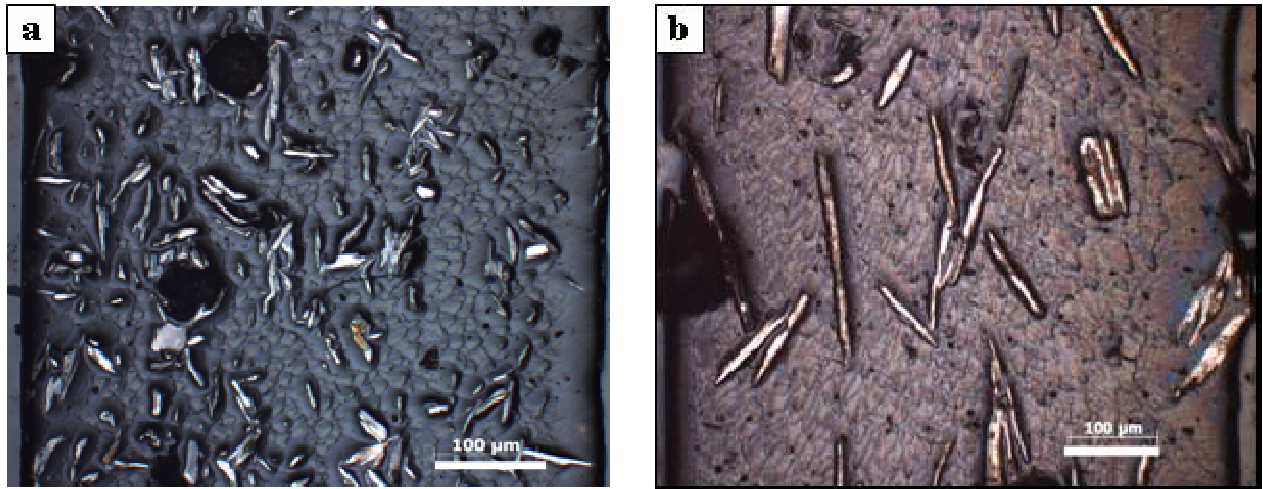


Figure E-1 Photomicrographs of polished double-dumped rotomoulded composite sections (5X magnification) at 15 wt.% graphite: (a) Zimbabwean graphite and (b) Expandable graphite

Appendix F: SEM fractographs of double-dumped rotomoulded composites

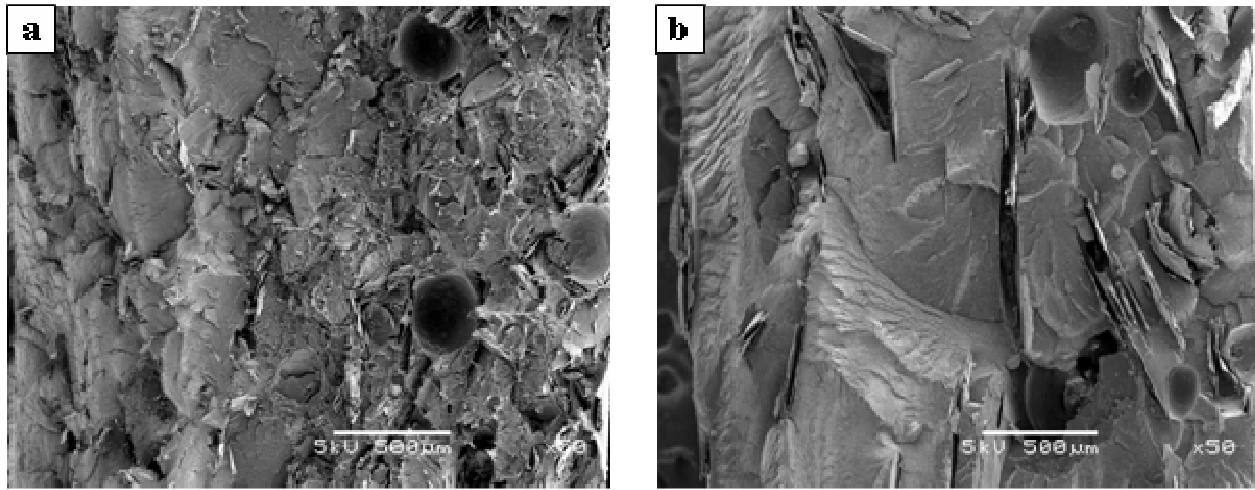


Figure F-1 SEM fractographs of double-dumped rotomoulded composites with 10 wt.% graphite: (a) Zimbabwean graphite and (b) Expandable graphite

Appendix G: DSC scans for pre-compounded rotomoulded graphite/LLDPE composites

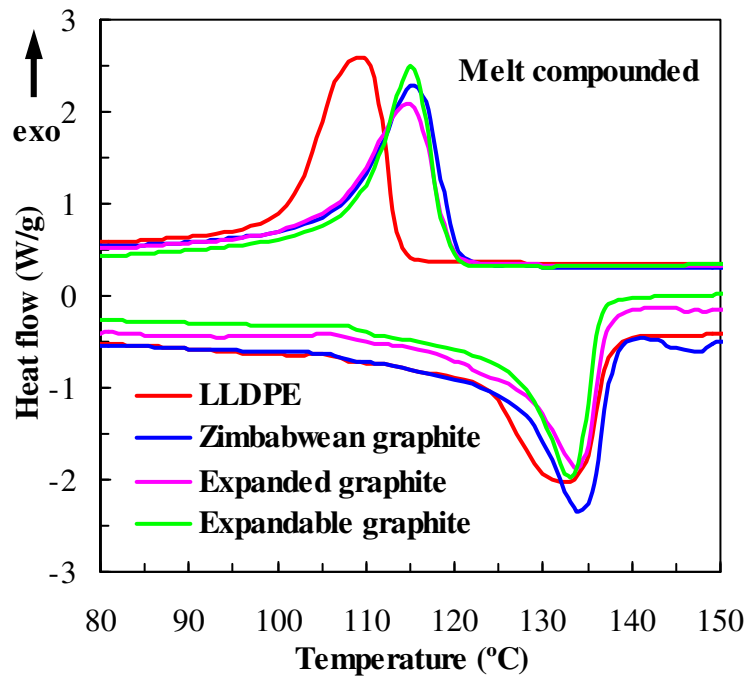


Figure G-1 DSC scans for pre-compounded rotomoulded graphite/LLDPE composites

Appendix H: Publications arising from this work

Mhike, W. and Focke, W.W. (In press). Surface resistivity and mechanical properties of rotationally molded polyethylene/graphite composites. *J. Vinyl Add. Tech.*

Mhike, W. and Focke, W.W. Thermal properties of rotationally moulded polyethylene/graphite composites (to be submitted to *Comp. Sci. Technol.* for publication).